



**University of  
Nottingham**

UK | CHINA | MALAYSIA

# **Improved Ultrashort Time Echo and Dynamic Contrast Enhancement Magnetic Resonance Imaging Based on Stack-of-Stars Golden Angle Radial Sampling Scheme**

Thesis submitted to the University of Nottingham for the degree of

**Doctor of Philosophy**

**Jichang Zhang**

**20026010**

Supervised by

**Dr. Chengbo Wang**

**Dr. Chiew-Foong Kwong**

**Dr. Paul Glover**

June 2022

# Abstract

Magnetic resonance imaging (MRI) is a radiation-free medical imaging technique and it is widely used for clinical diagnosis. MRI is developed from the physical phenomenon of nuclear magnetic resonance (NMR). MR signals are excited, spatially encoded and acquired by the corresponding radio-frequency (RF) pulse, gradient system and receiving coil system respectively. Compared to traditional medical imaging techniques like X-ray and Computed Tomography (CT), MRI requires a relatively long data acquisition time to gradually fulfill the k-space to form an image. Aggressive acceleration is applied to MRI to satisfy the clinical requirements for dynamic imaging. Meanwhile, MR signals from the short  $T_2$  tissues experience significant decay before data acquisitions, these tissues are invisible in MRI images. Ultra-short time echo (UTE) protocols are essential for imaging short  $T_2$  tissues.

This thesis explores the methods of imaging short  $T_2$  tissues and dynamic imaging using MRI. Experiments are performed using simulations, multiple resolution phantoms and human subjects. Several frameworks with a hybrid three-dimensional (3D) sampling scheme are developed for UTE imaging and highly accelerated dynamic MRI imaging respectively.

A significant contribution presented in this dissertation is the development and assessment of the 3D stack-of-star central out golden angle protocol for UTE imaging. Echo Time (TE) is reduced in the proposed protocol by applying the adaptive phase encoding gradient. The intrinsic sensitivity to the hardware

imperfection in the non-Cartesian UTE imaging is alleviated by employing trajectory measurement and iterative density compensation function (DCF). The self-gating property is effectively utilized to achieve motion resolved lung imaging, enabling investigation of lung functions incorporated with oxygen-enhanced MRI.

This thesis also presents a significant contribution for improved reconstruction of dynamic contrast enhanced (DCE) MRI based on the stack-of-stars golden angle sampling scheme. In this thesis, Low Rank plus Sparse (L+S) with two sparsity constraints temporal total variation (TV) and temporal fast Fourier transform (FFT) is developed and assessed. The additional sparsity constraint temporal FFT is employed to alleviate the temporal blurring caused by temporal TV and recover the dynamic contrast. The proposed method achieved high spatial-temporal resolution, high reconstruction efficiency and improved dynamic contrast simultaneously when comparing with other methods in reconstructing several simulated phantom datasets and free-breathing liver DCE-MRI datasets. Another contribution in this thesis is the soft-weighting for motion corrected DCE-MRI. A soft-weighting matrix is integrated into the proposed reconstruction framework for motion corrected DCE-MRI. Compared to the motion subdivision, a better motion compression is achieved by soft weighting function without increasing computational complexity.

# Acknowledgments

I started my PhD journey at Sir Peter Mansfield Imaging Center in University of Nottingham Ningbo China in September 2017. The past four years that spent here gave me plenty of memories. I would like to express my thanks to many people who both helped me in my studies and research. The first two people I would like to thank are my supervisors Dr. Chengbo Wang and Dr. Yaping Zhang.

When I just finished my master degree in the University of Nottingham United Kingdom in 2016, I was very anxious about the future path. Without the recommendation and encouragement from Yaping, I would not start my MRI journey. I am very grateful to have advising and guidance from Chengbo. I learned how to discover problems, think about problems and solve them independently during my PhD degree. His supervision and guidance made me be a quantified PhD student. He offered a chance to me to be an exchange student in Sir Peter Mansfield Imaging Center in University of Nottingham United Kingdom.

I would like to thank Prof. Richard Bowtell, Dr. Paul Glover, Prof. Penny Gowland and Prof. Sue Francis for their guidance and help during my research time in UK campus. They also provided financial support for me during lock-down duration caused by COVID-19 pandemic in 2020. I am extremely grateful for their help while the one-year research in UK campus is one of the most significant durations in my PhD study. I would like to express my appreciation to my colleague in UK campus Faisal Najeeb. I have obtained plenty of research ideas from the discussions with him.

I am very grateful to my second supervisor Dr. Chiew-Foong Kwong and my internal assessor Dr. Jing Wang for their supervision and help. Their guidance and encouragement ensure my research progress. Thanks for the support from my colleague Xinpei Wang. We are the first two PhD students in MRI laboratory in Ningbo campus. We used to study and work together. I am also grateful for the support from my colleagues including Pengfei Xu, Zhen Nan, Jie Zeng, Yulin Wang and Shao Che. I have enjoyed the time spent with them in both working time and free time. Thanks for the technical support from the research assistant Rachel Yao in our laboratory. Without help from her, I would not be able to complete the MRI experiments so smoothly.

Finally, I would like to express gratitude to my parents and all my other family members. I would not have been able to finish my PhD study without their infinite support and love.

# Contents

<b>Abstract.....</b>	<b>i</b>
<b>Acknowledgments.....</b>	<b>iii</b>
<b>List of Figures .....</b>	<b>viii</b>
<b>List of Tables.....</b>	<b>xx</b>
<b>List of Abbreviations .....</b>	<b>xxi</b>
<b>Chapter 1 Introduction.....</b>	<b>1</b>
1.1 Overview.....	1
1.2 Research Gap.....	7
1.3 Research Purpose.....	9
1.4 Thesis Outline.....	10
<b>Chapter 2 Background .....</b>	<b>12</b>
2.1 NMR Phenomenon .....	12
2.2 MR Signal Generation .....	14
2.3 Relaxation Phenomenon .....	15
2.4 Spatial Encoding.....	17
2.4.1 FID Signal.....	17
2.4.2 Gradient Field Encoding.....	18
2.5 Sampling Pattern in MRI.....	23
2.6 Non-Cartesian Reconstruction.....	28
<b>Chapter 3 MRI Acceleration.....</b>	<b>33</b>
3.1 Parallel MRI.....	33
3.2 Compressed Sensing.....	37
3.2.1 Sparse Representation in Measurement.....	38
3.2.2 Sparse MRI.....	40
3.2.3 Compressed SENSE .....	45
3.3 Simple Applications of Compressed Sensing.....	45
3.4 Conclusion.....	49
<b>Chapter 4 Stack-of-Stars Central Out Golden Angle UTE Imaging .....</b>	<b>50</b>
4.1 2D UTE Imaging .....	52
4.2 3D UTE Imaging .....	53
4.3 Hybrid 3D Sampling Pattern for 3D UTE Imaging.....	54
4.3.1 Stack-of-Stars Sampling.....	55

4.3.2	Golden Angle Radial Sampling .....	56
4.3.3	Stack-of-Stars Central Out Golden Angle UTE imaging .....	57
4.3.4	Stack-of-Stars UTE with Adaptive Time Echo .....	58
4.4	Trajectory Calibration.....	60
4.5	Iterative Density Compensation Function .....	64
4.6	Stack-of-Stars 3D UTE Imaging.....	66
4.6.1	3D Stack-of-Stars UTE Pulse Sequence Design.....	66
4.6.2	Stack-of-Stars 3D UTE Brain Imaging.....	67
4.6.3	Stack-of-Stars 3D UTE Knee Imaging .....	68
4.6.4	Pre-scan for Trajectory Calibration .....	69
4.7	Image Reconstruction and Analysis .....	70
4.8	Discussion.....	75
4.9	Conclusion .....	76
<b>Chapter 5</b>	<b>Motion Resolved UTE Lung Imaging with Oxygen Enhancement .....</b>	<b>77</b>
5.1	Motion Estimation and Subdivision .....	78
5.2	Oxygen-Enhanced UTE Lung Imaging .....	81
5.3	Free-Breathing UTE Lung Imaging Applications .....	83
5.3.1	3D Free-Breathing UTE Lung Imaging.....	83
5.3.2	UTE Lung Imaging with Oxygen Enhancement .....	83
5.4	Image Statistical & Analysis .....	85
5.5	Discussion.....	89
5.6	Conclusion .....	91
<b>Chapter 6</b>	<b>Improved DCE-MRI Imaging .....</b>	<b>92</b>
6.1	Golden Angle Radial Sparse Parallel.....	93
6.2	L+S Decomposition.....	95
6.3	Temporal Sparsity Constraints.....	97
6.4	L+S with Joint Sparsity .....	99
6.5	Dynamic Simulation with Model Phantom .....	101
6.5.1	Phantom with Dynamic Variation .....	102
6.5.2	Reconstruction Parameter Design.....	105
6.5.3	Quantification of Dynamic Performance .....	106
6.6	Clinic Dataset and Reconstruction.....	109
6.7	Image Analysis and Statistics .....	111
6.8	Discussion.....	114

6.9	Conclusion .....	117
<b>Chapter 7</b>	<b>Motion Corrected DCE-MRI.....</b>	<b>118</b>
7.1	Motion Subdivision in Extra Dimension GRASP .....	118
7.2	Respiratory Weighted GRASP .....	120
7.3	L+S Decomposition with Soft Weighting .....	123
7.4	Dynamic and Motion Simulation with Model Phantom.....	126
7.4.1	Phantom Simulation Design .....	126
7.4.2	Experiment Design .....	130
7.4.3	Simulation Results & Analysis .....	131
7.5	L+S with Soft Weighting and Joint Sparsity .....	137
7.6	Simulation Results & Analysis .....	139
7.7	Clinic Dataset and Reconstruction.....	143
7.8	Image Analysis and Statistics .....	145
7.9	Discussion.....	150
7.10	Conclusion .....	154
<b>Chapter 8</b>	<b>Conclusion and Future Development.....</b>	<b>155</b>
8.1	Thesis Contributions .....	155
8.2	Significant Innovations .....	157
8.3	Limitations and Future Research Plan .....	159
	<b>Reference.....</b>	<b>161</b>

# List of Figures

Figure 2-1: (a) Spins are randomly oriented without an external magnetic field. The net magnetic moment vector is zero. (b) Spins are aligned parallel or anti-parallel to the direction of the external field  $B_0$ . The energy of parallel state is slightly lower than the anti-parallel state and more spins are aligned parallel to the  $B_0$ . A net magnetization vector is generated. .... 13

Figure 2-2: (a) The net magnetization vector is located in the direction of the external magnetic field z-axis without RF excitation. (b) The net magnetization is gradually rotated from z-axis to x-y plane while a transverse magnetization component  $M_{xy}$  is produced. The net magnetization component can be completely converted into  $M_{xy}$  by implementing a  $90^\circ$  RF pulse for excitation..... 15

Figure 2-3: (a) The longitudinal magnetization vector  $M_z$  gradually recovers to the equilibrium state due to the  $T_1$  relaxation effect. (b) The transverse magnetization vector  $M_{xy}$  gradually decays to zero due to the  $T_2$  relaxation effect..... 16

Figure 2-4: (a) Additional gradient magnetic field induces inhomogeneous distribution of magnetic field strength. (b) The spins precess at different Larmor frequencies along the z-axis. An RF pulse with limited bandwidth can be implemented to excite the spins which are precessing at corresponding frequencies. .... 19

Figure 2-5: Spin-Echo pulse sequence diagram. Slice gradient, phase encoding gradient and frequency encoding gradient are applied on z, y and x axes respectively. .... 22

Figure 2-6: A comparison of different 2D sampling schemes. (a) 2D Cartesian sampling scheme with two k-space intervals in phase encoding direction and frequency encoding direction respectively. (b) 2D non-Cartesian radial sampling scheme with a certain k-space interval. .... 24

Figure 2-7: (a) A standard 2D radial sampling pulse sequence diagram. (b) 2D radial sampling trajectories in k-space..... 26

Figure 2-8: Blurring and excessive gray level occur in gridding algorithm without density compensation function: (a) The initial computation Shepp-logan model with

a matrix size of 256\*256; (b) Gridding reconstruction of radial sampled phantom dataset with a larger FOV..... 31

Figure 3-1: (a) An example of 8-channel brain images. The inhomogeneous intensity distribution is induced by the receiving sensitivity maps of coil channels. A relatively homogenous brain image can be recovered by sum-of-square (SOS) of the multi-channel brain images. (b) Corresponding receiving sensitivity maps of receiving coil elements estimated by Walsh algorithm. .... 34

Figure 3-2: Brain image weighted by a coil receiving sensitivity map: (a) Initial brain image. (b) Receiving sensitivity map of a certain coil element. (c) Ultimate reconstructed brain image in this channel. .... 35

Figure 3-3: (a) The T1 weighted brain image. (b) Sparse representation of brain image in wavelet transform domain. Majority of DWT coefficients are approximately zero. (c) The brain image recovered from wavelet domain with 15% wavelet coefficients. The brain structure information was reserved effectively with about 6-fold smaller size..... 39

Figure 3-4: (a) Random sampling on phase encoding dimension in 2D Cartesian sampling. (b) Corresponding PSF of 2D Cartesian sampling scheme on phase encoding dimension. (b) 2D random sampling scheme. (d) PSF of the 2D random scheme with much better incoherence..... 42

Figure 3-5: Basic procedure of simulation of the compressed sensing. Random undersampling pattern induces noise-like artefacts while these artefacts have negligible power in the DWT domain. .... 46

Figure 3-6: (a) Fully sampled reference brain image. (b) Randomly undersampled brain image at AF=6. (c) Brain image reconstructed by compressed sensing at AF=6. .... 47

Figure 3-7: Simulation about producing a multi-channel brain MRI dataset with virtual receiving sensitivity maps. .... 48

Figure 3-8: A comparison of compressed sensing and compressed SENSE in reconstructing a radial undersampled brain image at AF=4. Compared to the reference, fewer errors were observed in compressed SENSE..... 48

Figure 3-9: (a) NUFFT reconstruction of phantom dataset acquired by radial sampling pattern at AF=3. (b) NUFFT reconstruction of phantom dataset acquired by radial sampling pattern at AF=33. (c) Phantom image reconstructed by compressed SENSE at AF=33. The residual undersampling artefacts are labelled by a red solid arrow. .... 49

Figure 4-1: 2D UTE imaging sequence with a ramped half Gaussian soft pulse for excitation. The TE of the pulse sequence is theoretically approaching zero, limited by the switch duration of coil systems..... 53

Figure 4-2: 3D UTE imaging pulse sequence diagram. Three readout gradients are implemented on x, y and z axes respectively, forming 3D central out radial sampling. .... 54

Figure 4-3: 3D stack-of-stars sampling pulse sequence diagram. Transverse plane and slice dimension are encoded by radial sampling and Cartesian sampling respectively. A shorter TE and TR can be achieved by combing the Gpz and refocusing section of slice selective gradient. .... 56

Figure 4-4: A comparison of partial sampling pattern between uniform radial sampling and golden angle radial sampling. 10 spokes are selected from two radial sampling patterns with a total of 100 spokes. K-space is still roughly covered by a partial part of golden angle radial sampling. .... 57

Figure 4-5: 3D stack-of-stars UTE pulse sequence diagram. TE is reduced by employing a short duration RF pulse and central out radial sampling pattern. The minimum TE is typically limited by the duration of phase encoding gradient Gpz. .... 58

Figure 4-6: Advanced 3D stack-of-stars UTE pulse sequence diagram with adaptive TE. The duration of phase encoding gradient Gpz is increased gradually from central k-space to the outer k-space along the slice dimension. Minimum TE is achieved for k-space center which defines the basic image contrast..... 59

Figure 4-7: Pulse sequence for measuring the central out radial sampling trajectories. All the gradients are placed on the same axis while multiple slices are excited at different positions on this axis. Three orthogonal axes are measured by individual pre-scans respectively..... 63

Figure 4-8: Advanced trajectory measurement pulse sequence diagram. An additional dephasing gradient  $G$  is introduced into the pre-scan to shift the position of signal nulling in the acquired MR signal. The SNR of acquired is improved by averaging pre-scans with dephasing gradient  $+G$ ,  $0$  and  $-G$  while the errors from signal nulling are compressed effectively..... 63

Figure 4-9: (a) A comparison of theoretical sampling trajectories (red lines) and measured sampling trajectories (blue lines). (b) A zoomed view of theoretical sampling trajectories and measured sampling in k-space center. .... 70

Figure 4-10: (a) Reconstruction with theoretical trajectories and simple DCF. (b) Reconstruction with measured trajectories and simple DCF. (c) Reconstruction with theoretical trajectories and iterative DCF. (d) Reconstruction with measured trajectories and iterative DCF..... 72

Figure 4-11: A comparison of brain images acquired using advanced 3D stack-of stars UTE imaging and stack-of-stars VIBE imaging. The short T2 coil signals were captured in UTE images labelled by red indicators..... 72

Figure 4-12: A comparison of brain images acquired using advanced 3D stack-of stars UTE pulse sequence with parameters:  $TR/TE=5.0/0.14ms$ ,  $FA=6^\circ$ ,  $FOV=260mm * 260mm * 250mm$ , matrix size  $256 * 256 * 64$  and 2D GRE pulse sequence with parameters  $TR/TE=500ms/10ms$ ,  $FOV=260*260mm$ ,  $FA=70^\circ$ , matrix size  $256 * 256$ , number of slices=30. The intensity enhancements of nose cartilage, the eye optic nerve and teeth were observed in UTE images ..... 73

Figure 4-13 (a) A slice of knee image acquired by advanced 3D stack-of stars UTE pulse sequence with parameters:  $TR/TE=5.0/0.14ms$ ,  $FA=6^\circ$ ,  $FOV=180mm * 180mm * 240m$ , matrix size  $256 * 256 * 80$ . (b) A zoomed view of knee joint, the internal structure of cartilage can be obtained in detail..... 74

Figure 4-14: A representative slice of knee with metal implant acquired using advanced 3D stack-of stars UTE pulse sequence with parameters:  $TR/TE=5.0/0.26ms$ ,  $FA=6^\circ$ ,  $12^\circ$  and  $30^\circ$  (from left to right),  $FOV=180mm * 180mm * 240m$ , matrix size  $256 * 256 * 80$ . The metal implant sections and abnormal muscle regions were labelled by red arrows and a red cycle respectively. .... 74

Figure 5-1. Stack-of-stars central out golden angle sampling trajectories, the partition dimension and transverse plane are encoded as inner-loop and outer-loop respectively. .... 78

Figure 5-2: Procedures to estimate the motion signals from stack-of-stars sampling schemes. The repeated acquired k-space center is converted into the projection of the excited profiles on the partition dimension. The PCA algorithm is implemented to analyze the variation of these projection curves to estimate the rigid motion signal. .... 79

Figure 5-3: Motion subdivision for the continuously acquired spokes. The spokes are initially resorted according to the estimated respiratory signals and then subdivided into 4 motion states here. .... 80

Figure 5-4: Six representative slices of UTE lung images. High SNR in lung tissues was achieved by the proposed 3D UTE imaging protocol. .... 85

Figure 5-5: A zoomed view of lung tissues in three representative slices in 3D UTE imaging. The internal structure of lung tissues was clearly displayed in UTE images. .... 86

Figure 5-6 A comparison of UTE lung images in different motion phases. The lung images without motion subdivision expressed significant motion blurring. The motion blurring was compressed effectively in two motion resolved lung images. The respiratory motion leads to a significant position shift of diaphragm and other lung tissues between inspiration phase and expiration phase. .... 87

Figure 5-7 3D stack-of-stars central out golden angle UTE lung images and corresponding PSE maps at the end of expiration with variable flip angles from 3° to 12°. The corresponding mean of PSE is 3.33%, 4.89% and 8.88%. .... 88

Figure 5-8: 3D stack-of-stars central out golden angle UTE T1 weighed lung images and its corresponding PSE map. The first column on left is reconstructed from all spokes without phase segmentation. The other 4 columns correspond to 4 respiratory phases from inspiration to expiration. .... 89

Figure 6-1: GRASP reconstruction framework. Field maps are extracted from multi-coil reference images which are given by the coil-by-coil NUFFT reconstruction of the k-space data at a certain slice. The k-space is decomposed by 1D FFT on the

slice dimension in hybrid 3D datasets. The spokes are first resorted into undersampled dynamic time frames according to the acquisition time order. The GRASP reconstruction with NLCG algorithm is then applied to recover the image series by exploring the temporal sparsity among the subdivided time frames..... 93

Figure 6-2: Time frame subdivision from the fully golden angle sampled k-space dataset. The sub-sampling pattern within time frames is different between each other, offering the temporal sparsity..... 94

Figure 6-3: L+S decomposition reconstruction framework is similar to the previous iGRASP reconstruction framework. The spokes are first resorted into undersampled dynamic time frames according to the acquisition time order. A further subdivision is implemented on time frames to decompose low-rank components and sparse dynamic components in time series. The L+S decomposition reconstruction with ISTA algorithm is then applied to recover the image series by exploring the temporal sparsity among the dynamic sparse components..... 97

Figure 6-4. Operation for k-th iteration in the L+S decomposition with joint sparsity reconstruction framework.  $L_k$  is obtained by applying SVT for  $R_{k-1}-S_{k-1}$ . A shrinkage operator is implemented to the sparsity constraints in both the T and F domains to get  $ST_k$  and  $SF_k$  respectively.  $S_k$  is figured out by a linear combination of  $ST_k$  and  $SF_k$ . Image series  $M_k$  is then recovered as  $M_k = L_k + S_k$ . Additional residual signal  $E^*(E(L_k + S_k-d))$  is then subtracted to maintain the data consistency. The updated input  $R_{k+1}$  for the next iteration is obtained by a specific linear combination of the previous two points  $M_{k-2}$  and  $M_{k-1}$  which enforces faster convergence..... 101

Figure 6-5: Design of Shepp-logan model for dynamic simulation: (a) A general Shepp-logan computer model provided by Matlab. (b)~(d) Three phantom background sections, the signal intensity of these sections was kept constant as 1 and 0.4 and 0.2 respectively. (e) Six dynamic sections of computer model, the signal intensity of these sections were varied by the dynamic curve. (f) The ultimate computer model before contrast enhancement. .... 103

Figure 6-6: Signal intensity variation of dynamic sections in the computer model. A dynamic curve was created according to the DCE signal variation model obtained

in clinical datasets. The dynamic curve model contains a total of 588 discrete points between pre-contrast phase and venous phase. The signal intensity of dynamic sections in phantom model was modified by this dynamic curve. The maximum dynamic signal occurs at 187<sup>th</sup> point, forming central arterial phase. .... 104

Figure 6-7: Flowchart of data acquisition during dynamic variation period. 8 field maps were integrated into phantom before data acquisition forming multiple virtual coil channels. The simulation of data acquisition contains a total of 588 steps between pre-contrast phase and venous phase. Two data acquisitions were executed at each time point, producing fully sampled reference DCE series and continuous DCE phantom dataset respectively. .... 104

Figure 6-8: Three phase images corresponding to the reconstruction of the simulated phantom dataset at AF=22 (a total of 588 radial spokes and temporal resolution of 28 spokes/frame) using NUFFT, GRASP, L+S decomposition and the proposed method. Signal intensity in the selected region (labelled by circles) among all the frames was used to estimate the dynamic contrast performance in different reconstruction schemes. .... 108

Figure 6-9: Dynamic signal variation for the phantom using ground truth, fully sampled reference, GRASP, L+S and L+S with joint sparsity. Using the ground truth and fully sampled reference as the benchmark, our proposed L+S with joint sparsity method demonstrated much better dynamic contrast compared with GRASP and standard L+S. .... 108

Figure 6-10: A comparison of different reconstruction schemes in the three representative phases in a liver DCE-MRI dataset at AF= 22 and 28 spokes/frame. Both our proposed method and the standard L+S method provide better background structures than GRASP. Our L+S with joint sparsity followed by FCSEA demonstrated better dynamic contrast (solid arrow and dashed arrow). Arterial signal intensity in the selected region (labelled by circles) among all the frames was used to estimate the dynamic contrast performance in different reconstruction schemes. .... 112

Figure 6-11: Dynamic signal variation in the arterial region for the liver DCE-MRI dataset by using GRASP, L+S and L+S with joint sparsity. Improved dynamic

contrast was achieved by our proposed L+S with joint sparsity. Significant improvement of peak dynamic signal was observed in proposed L+S with joint sparsity..... 113

Figure 6-12: A comparison of the reconstructed images of GRASP, L+S decomposition and L+S with joint sparsity at different temporal resolutions in the venous phase of a liver DCE-MRI dataset. A total of 21, 28 and 42 frames were reconstructed at different temporal resolutions respectively. Blurring artefacts and degradation of image quality as observed in GRASP. Fewer blurring artefacts and degradation were observed in L+S with joint sparsity. The penalty factor for the three reconstruction schemes was set the same among all the reconstructions... 114

Figure 7-1: XD-GRASP reconstruction framework. The PCA algorithm is implemented to extract motion signals from repeatedly acquired k-space center along the slice dimension. The acquired spokes within time frames are resorted and subdivided into multiple motion states according to the extracted motion signal. An extra motion dimension is produced in XD-GRASP besides the temporal dimension. The XD-GRASP reconstruction with NLCG algorithm is then applied to recover the image series with multiple motion states by exploring the temporal sparsity among the time frames and motion sparsity among motion states..... 119

Figure 7-2: RACER-GRASP reconstruction framework. The PCA algorithm is implemented to extract motion signals from repeatedly acquired k-space center along slice dimension. The acquired spokes within time frames are resorted and subdivided into multiple motion phases according to the extracted motion signal. The RACER-GRASP reconstruction with NLCG algorithm is then applied to recover the image series with multiple motion states by exploring the temporal sparsity. An additional motion weighting matrix is implemented to control the contribution from different motion states and lock the desired motion phase during the iterative reconstruction. .... 121

Figure 7-3: The design of soft weighting functions. (a) Stair-step weighting function used in RACER-GRASP and the proposed modified sigmoid function. (b) Combined sigmoid functions for other motion phases. (c) Shifting the proposed

weighting function with a certain step-size for the reconstruction of different motion states. ....	125
Figure 7-4: L+S with soft weighting reconstruction framework. The acquired spokes within time frames are resorted according to the extracted motion signal. A soft weighting matrix is implemented to control the contribution from spokes acquired at different motion phases and lock the desired motion phase during reconstruction. Feasible motion states can be reconstructed by shifting the weighting matrix. ..	126
Figure 7-5: (a) A Shepp-logan computer model with modified internal structure. (b)~(c) Two background sections, the signal intensity of these sections was kept constant as 1 and 0.2 respectively. (d) Six dynamic sections of computer model, the signal intensity of these sections were varied by the dynamic curve. (e) Three motion sections of computer model, both the signal intensity and position of motion sections were varied. (f) The ultimate computer model before contrast enhancement. ....	128
Figure 7-6: Three representative contrast phases of modified Shepp-logan model at the same motion state. The signal intensity of six dynamic sections were varied by a dynamic curve model with a total of 1100 discrete points. The maximum dynamic signal occurs at 230 <sup>th</sup> point, forming central arterial phase. ....	128
Figure 7-7: 4 representative motion states of computer model before the dynamic contrast simulation. The motion sections were gradually rotated by the motion curve with a step-degree 0.37°. The rotation angle motion sections ranged from -15° to 15° .....	129
Figure 7-8: A comparison of reference at end-expiration stage to three reconstruction schemes without motion correction in three representative phase contrast in phantom dataset. Significant motion blurring was observed in NUFFT, GRASP and L+S decomposition. GRASP and L+S compressed the undersampling streaking artefacts effectively. ....	133
Figure 7-9: A comparison of reference at end-expiration stage to three reconstruction schemes with motion correction in three representative phase contrast in the phantom dataset. All the image series were reconstructed at AF= 8 and 100 spokes/frame. All three reconstruction schemes compressed motion	

blurring effectively. Some streaking artefacts remained in XD-GRASP. Better image quality was achieved in RACER-GRASP and the proposed method. .... 134

Figure 7-10: A comparison of GRASP, L+S decomposition, RACER-GRASP and L+S with soft weighting in venous phase at end-expiration stage. Three rows of images series corresponding to the venous phase image, zoomed view of a motion section in venous phase and the error maps in these five different reconstruction schemes. Significant motion errors were obtained in GRASP and L+S decomposition. L+S with soft weighting shows the least residual motion artefacts. .... 136

Figure 7-11: (a) Dynamic signal variation for the simulated phantom using reference, GRASP, XD-GRASP and RACER-GRASP. Two motion corrected GRASP techniques experienced more dynamic degradation than the standard GRASP. (b) Dynamic signal variation for the simulated phantom by using reference, L+S and L+S with soft weighting. A similar tendency about dynamic degradation was obtained in motion corrected L+S technique. L+S with soft weighting experienced more dynamic degradation than standard L+S decomposition. .... 137

Figure 7-12: L+S with soft weighting and joint sparsity reconstruction framework. The acquired spokes within time frames are resorted according to the extracted motion signal. A soft weighting matrix is implemented to control the contribution from spokes acquired at different motion phases and lock the desired motion phase during reconstruction. FCSA is implemented to solve the optimization problem with joint sparsity constraints. Feasible motion states can be reconstructed by shifting the weighting matrix. .... 138

Figure 7-13: A comparison of four different motion correction schemes in three representative phase contrast in phantom dataset. All the image series were reconstructed at AF= 8 and 100 spokes/frame. All schemes reconstructed the end-expiration phase accurately. The improved dynamic signal was obtained in arterial phase in the proposed method. .... 140

Figure 7-14: A comparison of four reconstruction schemes in venous phase at end-expiration stage. Three rows of image series corresponding to the venous phase image, zoomed view of motion section in venous phase and the error map in these

5 different reconstruction schemes. L+S with soft weighting and L+S with soft weighting and joint sparsity showed much fewer residual motion errors compared with XD-GRASP and RACER-GRASP..... 141

Figure 7-15: Dynamic signal variation for the simulated phantom using XD-GRASP, RACER-GRASP, L+S with soft weighting and proposed L+S with soft weighting and joint sparsity. Best dynamic contrast was achieved by the proposed method. The peak dynamic signal of the proposed method is a little bit higher than XD-GRASP and much higher than L+S with soft weighting and RACER-GRASP. 142

Figure 7-16: A comparison of different reconstruction schemes in three representative phases in a free-breathing liver DCE-MRI dataset. The reconstruction period for XD-GRASP, RACER-GRASP with GROG, L+S with soft weighting and the proposed method is 560.5s, 106s, 58.3s and 59.4s respectively. RACER-GRASP contains unexpected convolution artefacts (dashed arrow). The proposed method achieved the best dynamic tissue contrast and motion compression. .... 145

Figure 7-17: A further comparison of XD-GRASP, RACER-GRASP and the proposed L+S with soft weighting and joint sparsity reconstruction schemes in three representative phases with respiratory motion in zoomed view of liver section. Best tissue detail and dynamic contrast were observed in L+S with soft weighting and joint sparsity, especially in arterial phase..... 146

Figure 7-18: Dynamic signal variation among time frames in the arterial region in different reconstruction schemes. The peak dynamic signal in liver dataset in the proposed method demonstrated an increase in peak DCE signal by 7.8%, 23.1% and 20% than that of XD-GRASP, RACER-GRASP and L+S with soft weighting respectively..... 148

Figure 7-19: A comparison of XD-GRASP and L+S with soft weighting and joint sparsity for multiple motion states reconstruction in venous phase in liver DCE-MRI dataset with temporal resolution 100 spokes/frame. The structures in 4 motion states from inspiration to expiration in two reconstruction schemes were matched which certificated the fidelity of multiple motion states reconstruction through

shifting weighting function. The better tissue details and improved image quality were achieved by our method. .... 149

Figure 7-20: 12 motion states reconstructed by L+S with joint sparsity with shifted respiratory soft-weighting matrix in venous phase in liver image. Feasible motion states reconstruction was certificated. The image series with high motion state resolution explored the tissues variation caused by respiratory motion clearly. . 149

Figure 7-21: (a) A comparison of RACER-GRASP and L+S with soft weighting and joint sparsity at different temporal resolutions in the venous phase of liver images. The end-expiration phase was locked in two frameworks. Blurring artefacts and degradation of image quality were induced at higher AF in RACER-GRASP. Less blurring artefacts and degradation were obtained in the proposed method. The penalty factor for the two reconstruction schemes was set the same among all reconstructions. (b)~(d) Dynamic variation of the arterial signal intensity in the two reconstruction schemes at different temporal resolutions i.e. 96 spokes/frame (AF=6), 64 spokes/frame (AF=9) and 32 spokes/frame (AF=18). .... 150

# List of Tables

Table 6-1: Reconstruction time, Peak DCE signal and Mean DCE signal of the three reconstruction schemes in the simulated Phantom data. Reconstruction efficiency has been significantly improved in the proposed method due to L+S reconstruction while joint sparsity improved dynamic contrast in the proposed method. .... 109

Table 7-1: Reconstruction time, Peak DCE signal and Mean DCE signal of different reconstruction schemes in the simulated phantom data. Improved dynamic contrast, better motion correction and high reconstruction efficiency were obtained in the proposed method..... 142

# List of Abbreviations

<b>Abbreviation</b>	<b>Definition</b>
1D	one-dimensional
2D	two-dimensional
3D	three-dimensional
AF	acceleration factor
COPD	chronic obstructive pulmonary disease
CSA	composite splitting algorithm
CT	Computed Tomography
DCE	dynamic contrast enhancement / enhanced
DCF	density compensation function
DWT	discrete wavelet transform
FA	flip angle
FCSA	fast composite splitting algorithm
FFT	fast Fourier transform
FID	free induction decay
FISTA	fast iterative shrinkage and thresholding algorithm
FLASH	Fast Low Angle Shot
FOV	field of view
Gd-DTPA	gadopentate dimeglumine
GRAPPA	Generalized Auto-calibrating Partially Parallel Acquisition
GRASP	Golden Angle Radial Sparse Parallel
GRE	Gradient Reading Echo
GROG	self-calibrating GRAPPA operator gridding
HASTE	half Fourier-acquired single-shot turbo spin-echo
ISTA	iterative shrinkage and thresholding algorithm
L+S	Low Rank plus Sparse
MPSE	mean percent signal enhancement

MRI	magnetic resonance imaging
NLCG	Non-linear Conjugate Gradient
NMR	nuclear magnetic resonance
NUFFT	non-uniform fast Fourier transform
PCA	principle component analysis
PSE	percent signal enhancement
PSF	point spread function
RACER	Respiratory-Weighted
RER	relative enhancement ratio
RF	radio-frequency
RMSE	root mean square error
SE	Spin Echo
SENSE	Sensitivity Encoding
SMASH	Simultaneous Acquisition of Spatial Harmonics
SNR	signal-to-noise ratio
SOS	sum-of-square
SPR	sidelobe-to-peak ratio
SVD	Singular Value Decomposition
SVT	Singular Value Thresholding
TE	time echo / echo time
TV	total variation
UTE	ultra-short time echo / ultra-short echo time
VERSE	Variable-Rate Selective Excitation
XD	extra-dimension
ZTE	zero time echo / zero echo time

# Chapter 1 Introduction

## 1.1 Overview

Magnetic Resonance Imaging (MRI) is a robust technique in the realm of medical imaging systems while it plays an increasingly crucial role in clinical diagnosis. Compared with the conventional medical imaging techniques X-ray and Computed Tomography (CT) which are based on the absorption rate difference of X-ray among tissues, there is no X-ray radiation implemented in MRI. Hence, MRI is regarded as a non-radiation imaging technology. MRI provides medical imaging with high resolution and a variety of contrast parameters, enabling superior characterization of soft-tissues (1).

MRI is developed from the physical phenomenon of nuclear magnetic resonance (NMR) in atoms (2,3). By employing a strong external magnetic field on the imaging object, the atomic spins are aligned parallel or anti-parallel to the direction of magnetic field. A macroscopic magnetization vector is generated by the gap of spins in two states and it is aligned with the direction of the external field. A radial-frequency (RF) pulse is implemented to excite the spins and rotate the magnetization vector from the longitudinal direction to the transverse plane. The MRI receiving systems detect the magnetization vector in transverse plane and ultimately convert the detected electromagnetic signal into the MR signals.

In conventional MRI experiments, gradient systems are employed to assign the spatial information to the excited spins before data acquisition. The gradient magnetic field induces inhomogeneous field strength. Hence, gradient encoding

introduces specific precessing frequency and phase offset which depend on the spatial position of the spins signal, enabling the localization of MR signals (4). With delicate gradient encoding and data acquisition, the acquired MR signal gradually fulfills a Fourier transform based frequency domain k-space. Cartesian sampling is the most frequent sampling scheme in MRI which fills the k-space line-by-line. The MRI image can be directly reconstructed from Cartesian sampled k-space by applying an inverse Fast Fourier Transform (FFT) function.

After the RF excitation, the longitudinal magnetization vector gradually recovers to its equilibrium state while the transverse magnetization starts to decay. The recovery of longitudinal magnetization vector and the decay of transverse magnetization vector are described by  $T_1$  relaxation effect and  $T_2$  relaxation effect respectively (5).  $T_1$  and  $T_2$  are two intrinsic parameters of the tissues in human body. The decay of MR signals caused by  $T_2$  relaxation can be alleviated by decreasing the echo time (TE) between RF excitation and data acquisition.

The minimum TE in conventional Cartesian sampling MRI is limited as milliseconds which is sufficiently small for imaging the long  $T_2$  tissues like fat and muscle. The signals from long  $T_2$  tissues experience relatively small decay before the data acquisition. However, for the tissues with extremely short  $T_2$  like meninges and cartilage, their MR signals experience significant decay before the data acquisition (6). Consequently, these tissues become invisible in reconstructed images, leading to the missing of significant diagnosis information.

To catch the MR signals from short  $T_2$  tissues, ultra-short time echo (UTE) imaging techniques have been developed from the non-Cartesian sampling scheme (7). By adjusting the gradient waveform appropriately, the k-space data can be acquired by other sampling trajectories like radial and spiral. Non-Cartesian sampling enables data acquisition from the central k-space to the outer k-space, reducing the TE parameter effectively. The central out radial sampling is the most popular non-Cartesian sampling scheme in UTE imaging. The minimum TE has been reduced to be less than 10 us with special receiving coil systems in both two-dimensional (2D) UTE imaging and three-dimensional (3D) UTE imaging (8). However, 2D UTE imaging is extremely sensitive to hardware imperfections. The data acquisition efficiency in radial sampling is intrinsically lower than Cartesian sampling because more spokes are required to satisfy the Nyquist standard in radial sampling. The acquisition efficiency in 2D UTE is further degraded by a factor of four compared to the conventional radial sampling (6,7).

3D UTE is a robust method for imaging short  $T_2$  tissues, offering high signal-to-noise ratio (SNR), isotropic resolution and less sensitivity to hardware imperfections, etc. 3D UTE employs a short duration RF pulse and 3D radial sampling scheme to excite the entire imaging volume and acquire MR signals respectively (9). The minimum TE in conventional 3D UTE is around 100 us which is sufficient to image majority of short  $T_2$  tissues. However, the acquisition time in 3D UTE is still relatively long while the excessive computation cost from gridding reconstruction limits its real-time clinical applications.

In recent years, another 3D sampling scheme called stack-of-stars is proposed for fast 3D MRI imaging and it plays an increasingly significant role in 3D MRI imaging. Stack-of-stars employs non-Cartesian radial sampling and Cartesian sampling on the transverse plane and partition dimension respectively, forming a 3D hybrid sampling scheme (10). Stack-of-stars achieves fast data acquisition and reconstructions. Partition information can be interpolated feasibly and simply decomposed by applying one-dimensional (1D) FFT. 3D UTE imaging can be obtained by integrating the central out model into the stack-of-stars sampling pattern, forming stack-of-stars UTE (11). With the adaptive design of phase encoding on partition dimension, similar TE can be achieved in stack-of-stars UTE compared to the conventional 3D UTE (12). A variety of researches have shown the priority of stack-of-stars UTE in terms of imaging speed, motion robustness and fast reconstruction. Meanwhile, the stack-of-stars sampling scheme contains the self-gating property. The motion signal can be estimated by analyzing the repeated projections on the partition dimension while these motion signals are helpful to improve the image quality for the tissues with periodic motion like lung and cardiac. Besides the application on UTE imaging, the stack-of-stars sampling scheme also shows a potential advantage for dynamic MRI imaging with the support of acceleration techniques. Compared with traditional medical imaging techniques like X-ray and Computed Tomography (CT), MRI typically requires a long duration to fulfill the k-space to satisfy the Nyquist sampling standard. This duration is further extended in non-Cartesian sampling schemes. The long data acquisition duration limits the clinical application of MRI.

The scan duration can be reduced by employing more powerful MRI systems for faster spatial encoding and acquisition but the overall improvement from hardware systems is limited. Undersampling k-space is another effective approach to reduce the total acquisition period. Partial Fourier imaging was proposed in 1980s which approximately reduces the number of k-space lines by half (13-15). The missing k-space samples are derived by exploring the conjugate symmetry property of the acquired k-space. However, the acceleration factor (AF) is limited to be less than 2 in partial Fourier imaging. Besides the partial Fourier imaging, a variety of parallel imaging techniques including Simultaneous Acquisition of Spatial Harmonics (SMASH) (16), Sensitivity Encoding (SENSE) (17) and Generalized Auto-calibrating Partially Parallel Acquisition (GRAPPA) (18) were proposed in the past few decades. Regular undersampling in Cartesian k-space causes aliasing artefacts in the spatial domain. Parallel imaging utilizes the additional sensitivity field map information from multi-channel receiving coils to derive the missing k-space samples or decompose the aliased pixels for recovering images without aliasing from a subset of measurements. However, the AF is limited by the number of channels in the receiving coil while SNR is decreased with the increasing of AF in parallel imaging (18,19).

Compressed Sensing is another acceleration technique which achieves advanced AF for MRI. It was initially reported by Donoho, et al. in 2006 (20) and it was applied for undersampling MRI reconstruction soon by Lustig in 2007 (21). The basic principle of compressed sensing is based on the fact that majority of digital images including medical images are typically compressive with appropriate transform like

Discrete Wavelet Transform (DWT) and Total Variation (TV) (21,22). Images are expressed sparsely in these transform domains. Power is mainly concentrated on a few transform coefficients while other transform coefficients have negligible power. Inversely, a few transformed coefficients are sufficient to recover the images without significant quality degradation while it offers the compression availability for undersampled MRI reconstruction. Compressed sensing is typically combined with a random or pseudorandom sampling pattern in MRI. Noise-like artefacts are induced by random undersampling schemes while they have negligible power in the sparse transform domain (21). Consequently, these artefacts can be easily filtered out during iterative reconstruction while MRI images are reconstructed from highly undersampled k-space without loss of significant information.

Random sampling is limited by the slew rate of gradient system and only performed on phase encoding dimension in 2D Cartesian MRI imaging. However, non-Cartesian sampling schemes like radial sampling intrinsically contain more measurements in k-space center and high sampling incoherence. Radial scheme distributes undersampling interference among all the spatial dimensions, achieving high incoherence for better sparse signal recovery in compressed sensing (23-25).

Compressed sensing is limited in conventional 3D radial sampling imaging due to the excess computation burden. But it can also be applied for accelerating stack-of-stars based 3D MRI imaging. After partition decomposition, compressed sensing can be implemented to reconstruct the images slice-by-slice from the k-space acquired by stack-of-stars sampling pattern. The combination of stack-of-stars and

compressed sensing enables fast 3D imaging in MRI with prior image quality, high AF and better motion robustness (26-28).

Meanwhile, gold angle technique is usually integrated into the stack-of-stars sampling scheme, obtaining a relatively uniform coverage of k-space with any arbitrary number of consecutive spokes (10,29). The acquired spokes can be subdivided into multiple frames on temporal dimension or motion dimension. By implementing the compressed sensing to explore the sparsity among subdivided frames, 3D MRI images can be reconstructed with high spatial-temporal or spatial-motion resolutions which are desired by dynamic MRI imaging. Many researchers have focused on developing the reconstruction frameworks for dynamic contrast enhanced (DCE) MRI based on compressed sensing and stack-of-stars golden angle sampling scheme.

## **1.2 Research Gap**

### **Continuous and Motion Resolved 3D UTE Imaging**

The current research of stack-of-stars UTE mainly focuses on the fast imaging speed and its clinical applications. There are some limitations of stack-of-stars UTE imaging:

1. Stack-of-stars central out radial sampling is still sensitive to the hardware imperfection. Delicate calibration of MRI hardware system is extremely complex and time-consuming.
2. Limited researches work on utilizing the self-gating property in stack-of-stars schemes. Researchers typically employ additional gating system to

support the MRI imaging for tissues with respiratory motion like lung and liver. A soft gating model is implemented to trigger the data acquisition within the certain respiratory phase. Overall data acquisition efficiency is significantly degraded by the waiting time in soft gating model.

3. Conventional UTE imaging cannot be used to obtain the functional lung imaging like ventilation and perfusion maps of lung.

### **Improved DCE-MRI with Stack-of-Stars Golden Angle Sampling**

A variety of reconstruction frameworks have been developed for DCE-MRI based on stack-of-stars sampling scheme and compressed sensing. By exploring temporal sparsity among subdivided frames, the dynamic image series can be reconstructed with high spatial-temporal resolution. However, there are some limitations within these reconstruction frameworks:

1. Additional temporal blurring is introduced during iterative reconstruction while the dynamic contrast is degraded. There are limited researches working on recovering the dynamic contrast from the temporal blurring effect.
2. The respiratory motion is another challenge in DCE-MRI. Some motion corrected frameworks are developed with motion subdivision. The motion subdivision increases the reconstruction period and decreases the temporal resolution.
3. It is difficult to obtain the fully sampled DCE-MRI reference in practice. The quantification of the dynamic and motion correction performance of these reconstruction frameworks is extremely difficult.

## **1.3 Research Purpose**

### **Continuous and Motion Resolved 3D UTE Imaging**

We plan to develop an improved 3D UTE imaging protocol based on the stack-of-stars central out golden angle sampling scheme which contains following optimizations:

1. Develop a simple and robust calibration framework for reducing the imaging artefacts caused by hardware imperfections.
2. Increase the data acquisition efficiency by using a continuous acquisition model. The motion solved UTE imaging is supposed to be achieved without the expense of additional gating system and waiting time during the acquisition.
3. Achieve functional lung imaging by using the oxygen-enhanced MRI in UTE imaging. Additional ventilation information in lung can be obtained from the oxygen enhancement effect.

### **Improved DCE-MRI with Stack-of-Stars Golden Angle Sampling**

We plan to develop an advanced reconstruction framework for accurately characterizing the lesions and tumors in clinical diagnosis. The reconstruction framework contains following improvements:

1. Improve the dynamic contrast by optimizing the structure of reconstruction models.
2. Develop a simple and effective motion compression method for the reconstruction framework for free-breathing liver DCE-MRI. Both the

computation efficiency and temporal resolution are not supposed to be degraded by this motion correction method.

3. Create simulation frameworks to quantify the performance of the proposed method in terms of temporal resolution, motion compression and dynamic contrast, etc.

## 1.4 Thesis Outline

**Chapter 1** gives an overview of research background and the motivations for this dissertation.

**Chapter 2** presents a brief overview of fundamental principles in MRI and non-Cartesian gridding reconstruction.

**Chapter 3** presents a review of parallel imaging, compressed sensing and compressed SENSE. Several experiments are implemented to certificate the robustness of compressed SENSE for reconstructing images from highly undersampled k-space.

**Chapter 4 and Chapter 5** present a stack-of-stars central out golden angle sampling scheme with adaptive TE for advanced 3D UTE imaging. Trajectory calibration and iterative density compensation are integrated into the reconstruction to improve the image quality. The performance of the proposed UTE protocol is certificated by a wide range of applications including metal implant imaging. The motion resolved lung UTE imaging is achieved by motion subdivision. The oxygen enhancement method is integrated into the UTE protocol for better clinical diagnosis.

**Chapter 6** presents an advanced reconstruction framework called Low Rank plus Sparse (L+S) decomposition with joint sparsity with stack-of-stars golden angle sampling scheme for improved reconstruction of DCE-MRI. A simulation framework is established to quantify the performance of the proposed method and other reconstruction frameworks for DCE-MRI. The reconstructions are performed on a simulated phantom dataset and several clinical free-breathing liver DCE-MRI datasets. L+S with joint sparsity framework shows prior dynamic contrast, temporal resolution and reconstruction efficiency simultaneously.

**Chapter 7** presents a motion corrected reconstruction framework for motion compressed DCE-MRI called L+S with soft weighting. A soft weighting matrix is created with a modified sigmoid function to replace the additional motion subdivision by controlling the contribution from spokes acquired at different respiratory phases. A simulation framework is proposed to certificate the performance of L+S with soft weighting and other two motion corrected reconstruction frameworks for DCE-MRI. Improved reconstruction efficiency and fewer motion errors are obtained simultaneously in the proposed method. The proposed framework is further extended with joint sparsity, enabling accurate motion compression and improved dynamic contrast simultaneously.

**Chapter 8** presents a summary of the research works in this thesis. The limitations of the proposed methods and future research plans are discussed.

## Chapter 2 Background

This chapter gives an overview of basic principles of MRI, k-space sampling schemes and non-Cartesian k-space reconstruction techniques. The procedures for gridding the non-Cartesian k-space into Cartesian k-space are introduced.

### 2.1 NMR Phenomenon

The physical NMR phenomenon in solids and liquids was observed independently by Edward Purcell and Felix Bloch in 1940s (2,30). The atomic nucleus containing an odd number of protons, neutrons or both in combination such as  $H^1$  and  $C^{13}$  possess a property called nuclear spin with an angular momentum  $I$ . A tiny magnetic moment is generated by the nuclear spin and directly proportional to the  $I$  as:

$$\mu = \gamma I \quad (2.1)$$

Here  $\gamma$  is a constant value called gyromagnetic ratio. Hydrogen ( $H^1$ ) is the atom which is relevant to the human body most due to its abundance in water and lipids. Spin is the fundamental property of the nuclei in atoms. At room temperature, the spins of atoms ( $H^1$ ) are oriented in random directions while the microcosmic magnetic moment vectors generated by spins are cancelled with each other. There is no macrocosmic magnetic moment vector produced.

When a strong external magnetic field  $B_0$  is placed on the nuclei in hydrogen ( $^1H$ ), these spins are divided into two groups. One group of spins ( $n_+$ ) aligned parallel while others ( $n_-$ ) oriented anti-parallel with the direction of the external magnetic field as shown in Figure 2-1.

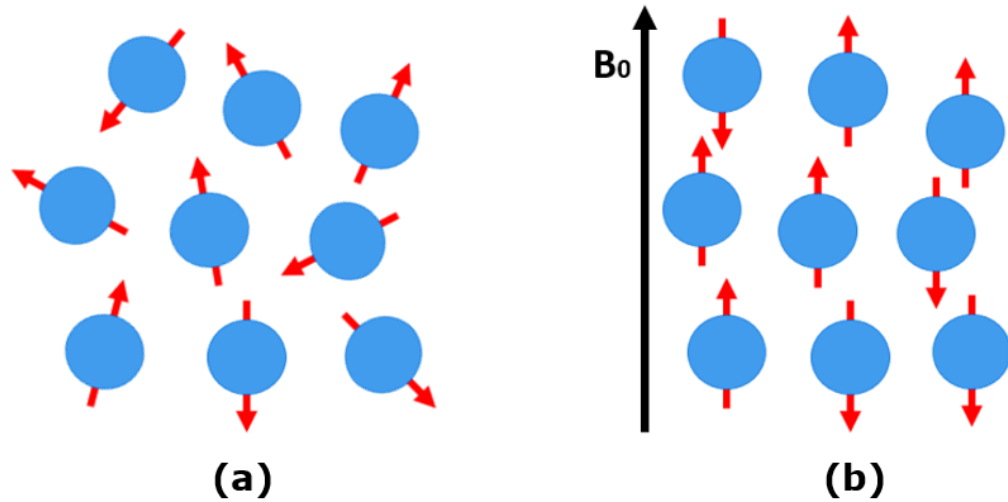


Figure 2-1: (a) Spins are randomly oriented without an external magnetic field. The net magnetic moment vector is zero. (b) Spins are aligned parallel or anti-parallel to the direction of the external field  $B_0$ . The energy of parallel state is slightly lower than the anti-parallel state and more spins are aligned parallel to the  $B_0$ . A net magnetization vector is generated.

Spins start to precess around the direction of  $B_0$  at the certain angular frequency  $\omega_0$  which is given by Larmor equation:

$$\omega_0 = \gamma B_0 \quad (2.2)$$

The energy of the parallel state is slightly lower than the anti-parallel state while more spins align themselves parallel with the direction of  $B_0$ . The ratio between nuclei aligned parallel and anti-parallel is demonstrated by Boltzmann distribution:

$$\frac{n_-}{n_+} = e^{\frac{\Delta E}{KT}} \quad (2.3)$$

Here  $K$  is the Boltzmann's constant and  $T$  is the absolute temperature.  $\Delta E$  is the potential energy gap between parallel state and anti-parallel state. At human body temperature, the thermal energy is much larger than the  $\Delta E$ . Therefore, only a few

more nuclei are in the parallel state for every million nuclei while it is called spin excess (31). Due to the imbalanced distribution of nuclei, a net magnetization vector  $M_0$  is induced and aligned with the direction of  $B_0$ , expressed as:

$$M_0 = \frac{\gamma^2 h^2 B_0 N}{4KT} \quad (2.4)$$

Here  $h$  is the Planck's constant. The magnitude of the net magnetization is directly proportional to the strength of  $B_0$ .

## 2.2 MR Signal Generation

A bulk non-vanishing spin excess is insufficient to induce the detectable signal. The net magnetization vector  $M_0$  needs to be tipped from direction of  $B_0$  (z-axis) to the transverse x-y plane which is perpendicular to the  $B_0$ . The rotation of net magnetization vector  $M_0$  is achieved by implementing a radio-frequency magnetic field (RF pulse) perpendicular to the  $B_0$  while this magnetic field is supposed to rotate at Larmor frequency to satisfy the condition of nuclear resonance.

$M_0$  is continuously rotated from z-axis to the transverse x-y plane during the RF excitation. The overall rotation degree or the flip angle (FA) is determined by both the magnitude and duration of RF pulse as:

$$\alpha = \int_0^T B_1(t) dt \quad (2.5)$$

Here  $B_1$  and  $T$  indicate the magnitude and duration of the RF pulse respectively. The rotation of  $M_0$  generates two magnetization vectors located on z-axis ( $M_z$ ) and in x-y plane ( $M_{xy}$ ) respectively. The precession of  $M_{xy}$  produces a changing

magnetic flux while this varying magnetic flux can be detected by the receiving coils and ultimately converted as the MR signal.

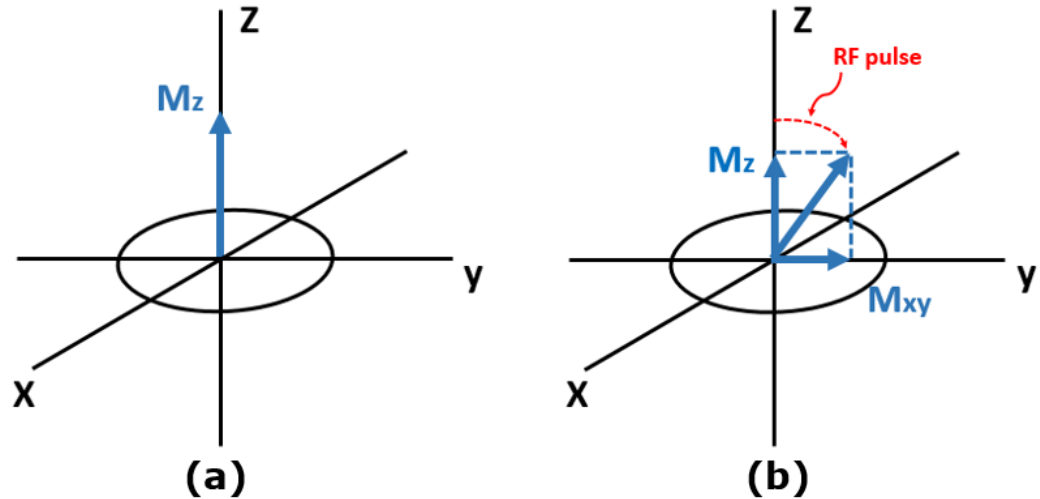


Figure 2-2: (a) The net magnetization vector is located in the direction of the external magnetic field z-axis without RF excitation. (b) The net magnetization is gradually rotated from z-axis to x-y plane while a transverse magnetization component  $M_{xy}$  is produced. The net magnetization component can be completely converted into  $M_{xy}$  by implementing a  $90^\circ$  RF pulse for excitation.

### 2.3 Relaxation Phenomenon

During the RF excitation, the spins are tipped from the equilibrium so that the net magnetization is pulled down to the transverse plane. These spins eventually return to the z-directed equilibrium state after the RF excitation. The recovery of  $M_z$  to its equilibrium state ( $M_z = M_0$ ) is known as spin-lattice relaxation which corresponds to the energy exchange between the processing protons and the surrounding lattice. The rate of the recovery process is described by the spin-lattice relaxation time  $T_1$ . For a  $90^\circ$  RF excitation, the recovery of  $M_z$  can be expressed as:

$$M_z(t) = M_0 \left(1 - e^{-\frac{t}{T_1}}\right) \quad (2.6)$$

After RF excitation, the excited spins gradually lose their coherence due to the local field inhomogeneity or interference between spins and environment. Consequently, the transverse magnetization vector  $M_{xy}$  experiences a decay. The decay process in  $M_{xy}$  is typically much faster than the recovery process in  $M_z$  while it is quantified by the spin-spin relaxation time  $T_2$ . The process of  $M_{xy}$  approaching to zero after  $90^\circ$  RF excitation is mathematically expressed as:

$$M_{xy}(t) = M_{xy}(0)e^{-\frac{t}{T_2}} \quad (2.7)$$

Figure 2-3a and Figure 2-3b show the recovery curve of the longitudinal magnetization vector  $M_z$  and the decay curve of the transverse magnetization vector  $M_{xy}$  respectively after the  $90^\circ$  RF excitation.

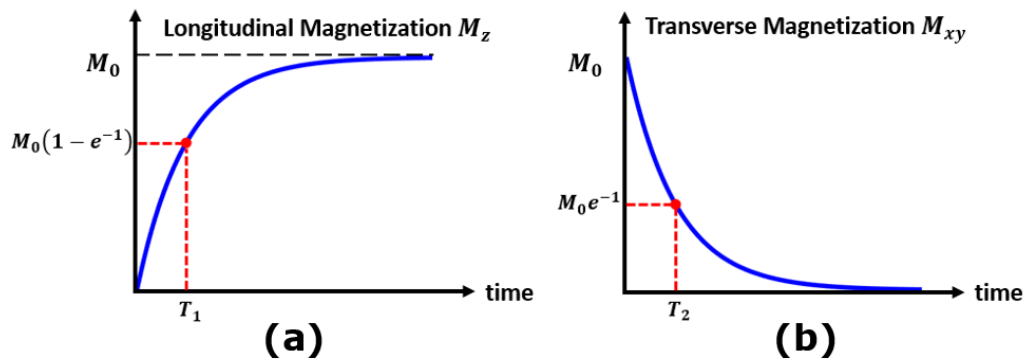


Figure 2-3: (a) The longitudinal magnetization vector  $M_z$  gradually recovers to the equilibrium state due to the  $T_1$  relaxation effect. (b) The transverse magnetization vector  $M_{xy}$  gradually decays to zero due to the  $T_2$  relaxation effect.

## 2.4 Spatial Encoding

### 2.4.1 FID Signal

As described previously, the precession of  $M_{xy}$  produce a changing magnetic flux while the circular coil elements which are perpendicular to the direction of  $B_0$  are implemented to detect this varied magnetic field signal. According to the Faraday's law of electromagnetic induction, the variation of magnetic flux for the closed coil can produce induction electromotive force (32). Hence, the net transverse magnetization vector signal  $M_{xy}$  is converted into the corresponding electrical signal—Free Induction Decay (FID) signal. The magnitude of FID signal is given by:

$$M_{FID} = M_{xy} e^{-\frac{t}{T_2^*}} \cos \omega_0 t$$
$$\frac{1}{T_2^*} = \frac{1}{T_2} + \gamma \Delta B \quad (2.8)$$

Here  $T_2^*$  is another parameter which describes the transverse relaxation rate under non-ideal experiment conditions. The local field difference  $\Delta B$  is produced by the inhomogeneity of  $B_0$  or difference of magnetic susceptibility among tissues, etc. The  $M_{xy}$  decay with the rate  $T_2^*$  which is much faster than ideal  $T_2$  relaxation in practice. Hence,  $T_2^*$  is typically several to hundreds of milliseconds smaller than  $T_2$ .  $\omega_0$  indicates the precession of  $M_{xy}$  at Larmor frequency.

## 2.4.2 Gradient Field Encoding

The signal detected by the coils contains the contributions from all the transverse magnetization vectors in the imaging object. The acquired MR signal can be simply expressed as:

$$S = \int M(u) du \quad (2.9)$$

Here  $u$  indicates the spatial position.  $M(u)$  and  $S$  presents the magnetization vector at a certain spatial position and ultimately acquired MR signal respectively. For simplification of the equation, the transverse relaxation effect is ignored during the data acquisition.

It is essential to assign the spatial localization information to spins before the data acquisition in MRI. The gradient systems on x, y and z axes are developed to modify local magnetic field strength to assign the spatial information to the magnetization vectors. The additional field gradient can be expressed as a combined vector. The local magnetic field strength with additional gradient field modification can be expressed as:

$$G = G_x i + G_y j + G_z k \quad (2.10)$$

Here  $G_x$ ,  $G_y$  and  $G_z$  present the gradient field strength on x, y and z axes respectively.  $i$ ,  $j$  and  $k$  indicate the corresponding spatial location on three axes relatively. The local field strength modified by additional gradient field can be expressed as:

$$B = B_0 + Gr \quad (2.11)$$

where  $r$  indicates the spatial position in the imaging object. According to the Larmor equation, the precession frequency of spins is directly proportional to the magnetic field strength. The spatially varied magnetic field induces spatial location dependent precession frequency for the spins and can be expressed as:

$$\omega = \gamma(B_0 + Gr) \quad (2.12)$$

In conventional 2D MRI imaging, a slice selective gradient magnetic field  $G_z$  is applied on the axis perpendicular to the imaging slice, inducing a varied precession frequency along that axis. An RF pulse with limited bandwidth is then implemented to excite the spins in a profile with certain thickness as shown in Figure 2-4.

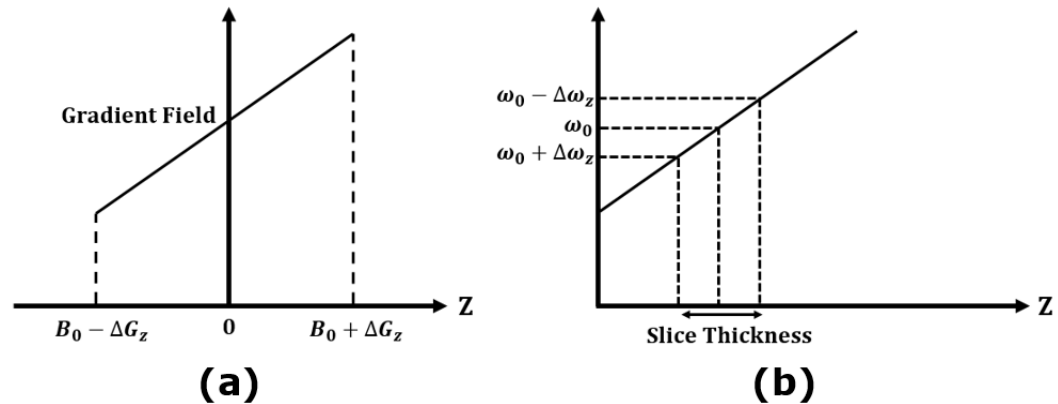


Figure 2-4: (a) Additional gradient magnetic field induces inhomogeneous distribution of magnetic field strength. (b) The spins precess at different Larmor frequencies along the z-axis. An RF pulse with limited bandwidth can be implemented to excite the spins which are precessing at corresponding frequencies.

The spins which locate out of profile are not excited due to the mismatching between their resonance frequency and RF frequency. The relationship among excited slice thickness, slice selective gradient strength and bandwidth of RF pulse can be mathematically expressed as:

$$\text{Slice Thickness} \propto \frac{\text{Pulse Bandwidth}}{G_z} \quad (2.13)$$

After exciting a certain profile, two gradient magnetic fields  $G_x$  and  $G_y$  are applied in two orthogonal directions in the excited profile to encode the in-plane spatial information.  $G_x$  and  $G_y$  works as the frequency encoding gradient and phase encoding gradient respectively. Phase encoding assigns the spatial information on the phase encoding direction by implementing the  $G_y$  for a short period.  $G_y$  induces different precession frequencies for spins along the phase encoding direction. Once the phase encoding gradient has been removed, the precession frequency of all the spins are recovered back to  $\omega_0$  due to the effect of  $B_0$ . An adequate phase offset which contains the spatial information for the each spin along the phase encoding direction is expressed as:

$$\phi_y = \int_0^{t_{pe}} \gamma G_y(t) y dt \quad (2.14)$$

where  $y$  is the spatial location of spins in the phase encoding direction while  $t_{pe}$  is the period of phase encoding. Frequency encoding is typically achieved by applying another gradient magnetic field  $G_x$  in the direction which is perpendicular to the  $G_y$  after finishing the phase encoding. Under the frequency encoding gradient, the spins along frequency encoding direction precess at different Larmor frequencies which are given by:

$$\omega_x = \gamma(B_0 + G_x x) \quad (2.15)$$

where  $x$  is the spatial location of spins along the frequency encoding direction. The MR signals are acquired during the frequency encoding while frequency encoding gradient is also named as readout gradient. Another phase component is introduced to the spins during readout as:

$$\varphi_x = \int_0^t \gamma G_x(t) x dt \quad (2.16)$$

Set two phase components introduced by phase encoding and frequency encoding as  $k_x$  and  $k_y$ . The MR signal at certain position of imaging slice after spatial encoding can be mathematically described as:

$$S(x, y) = m(x, y) e^{-i2\pi[k_x(t)x + k_y(t)y]} \quad (2.17)$$

Here  $m(x, y)$  presents the spin density at a certain position in a 2D object to be imaged. The ultimate acquired MR signals which contain the contributions from all the spins are given by:

$$M(k_x, k_y) = \iint m(x, y) e^{-i2\pi[k_x(t)x + k_y(t)y]} dx dy \quad (2.18)$$

Here  $k_x$  and  $k_y$  can be regarded as the two spatial-frequency variables in the 2D k-space. With delicate strength design of phase encoding and frequency encoding, the acquired MR signals in k-space present spatial Fourier transform of the imaging object. Figure 2-5 shows a standard Spin-Echo (SE) pulse sequence diagram for 2D MRI imaging.

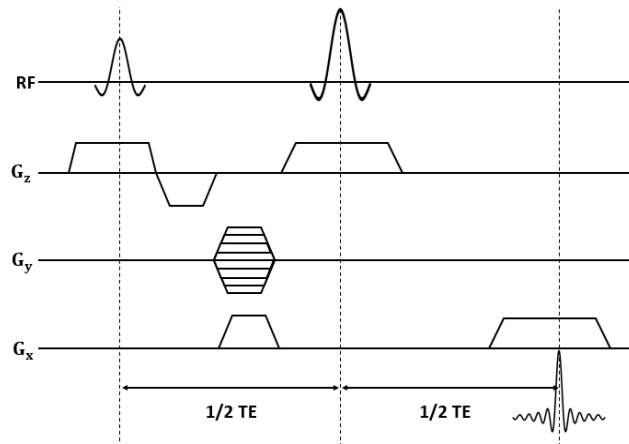


Figure 2-5: Spin-Echo pulse sequence diagram. Slice gradient, phase encoding gradient and frequency encoding gradient are applied on z, y and x axes respectively.

In SE pulse sequence, a  $90^\circ$  RF pulse is applied accompany with slice selective gradient  $G_z$  to excite a profiles with limited thickness. The transverse magnetization vector  $M_{xy}$  is reversed by a  $180^\circ$  RF pulse, removing the signal dephasing caused by local field inhomogeneity. The data acquisition occurs during the readout gradient as the signals of all voxels have been encoded spatially by frequency encoding gradient  $G_x$  and phase encoding gradient  $G_y$  within the excited transverse plane. Due to the existing of pre-dephasing gradient and 180 reversion RF pulse, an echo signal is produced and acquired in SE pulse sequence. The duration for completing above steps is the repetition time called TR. These steps will be repeated with different strengths of  $G_y$  until completely filling the k-space. In 2D MRI, the matrix size of k-space is  $N_x * N_y$  where  $N_x$  and  $N_y$  are the number of phase encoding steps and frequency encoding steps respectively.

2D MRI imaging can be converted into 3D MRI imaging by integrating an additional phase encoding gradient on the partition dimension. The signal equation is extended as:

$$M(k_x, k_y, k_z) \iiint m(x, y) e^{-i2\pi[k_x(t)x + k_y(t)y + k_z(t)z]} dx dy dz \quad (2.19)$$

where  $k_z$  is the phase offset introduced by the additional phase encoding gradient on the partition dimension.

## 2.5 Sampling Pattern in MRI

Conventional pulse sequences like Spin Echo (SE) and Gradient Reading Echo (GRE) gradually fulfill the k-space through repeated data acquisitions. The acquired samples in k-space are located on the Cartesian coordinates, forming Cartesian sampling. The k-space is fulfilled in a sequential line-by-line fashion in Cartesian sampling. However, the position of the acquired MR signal in k-space depends on both the encoding gradient waveforms and the encoding period according to the Equations 2.18 and 2.19. By adjusting the gradient waveform appropriately, the k-space data can be acquired by other sampling trajectories like radial and spiral, forming non-Cartesian sampling. Figure 2-6 shows a comparison of Cartesian sampling scheme and non-Cartesian radial sampling scheme.

K-space is sampled discretely in practice. The intervals between adjacent points in Cartesian sampling scheme are defined as  $\Delta k_x$  and  $\Delta k_y$  on the phase encoding dimension and frequency encoding dimension as shown in Figure 2-6a. The size of

k-space determines the resolution of the reconstructed MRI images while the field of view (FOV) of the images is determined by these two k-space intervals.

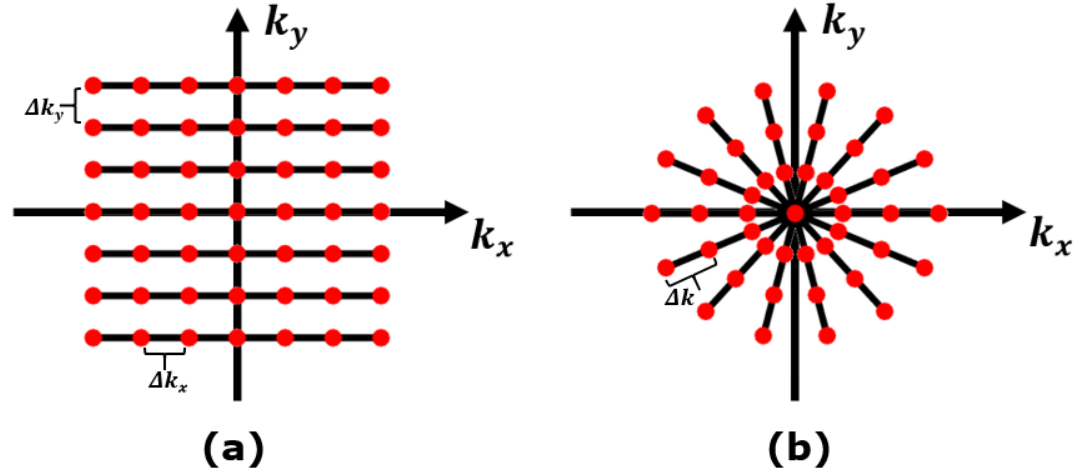


Figure 2-6: A comparison of different 2D sampling schemes. (a) 2D Cartesian sampling scheme with two k-space intervals in phase encoding direction and frequency encoding direction respectively. (b) 2D non-Cartesian radial sampling scheme with a certain k-space interval.

The FOVs of reconstructed image in phase encoding direction and frequency encoding direction are given by:

$$\begin{aligned}
 FOV_x &= \frac{1}{\Delta k_x} \\
 FOV_y &= \frac{1}{\Delta k_y}
 \end{aligned}
 \tag{2.20}$$

As mentioned before, the acquired k-space corresponds to the spatial Fourier transform of the imaging object. According to the Nyquist sampling standard of Fourier transform, the imaging FOV is supposed to be greater than the size of imaging object to avoid aliasing artefacts. Hence, the k-space intervals are required to satisfy the following conditions:

$$\begin{aligned}\Delta k_x &\leq \frac{1}{D_x} \\ \Delta k_y &\leq \frac{1}{D_y}\end{aligned}\tag{2.21}$$

Here  $D_x$  and  $D_y$  present the maximum size of imaging object in the frequency encoding direction and phase encoding direction respectively. Even though better images can be reconstructed from the k-space with infinite samples, the size of k-space is typically finite and limited by the acquisition period. A rectangular function with width  $2 \times k_{max}$  (from  $-k_{max}$  to  $+k_{max}$ ) is used to describe the k-space spatial frequency in the certain direction. The highest spatial frequencies in finite k-space are presented by the  $k_{xmax}$  and  $k_{ymax}$  in frequency encoding direction and phase encoding direction respectively. The spatial resolution in two orthogonal directions in Cartesian sampling can be expressed as:

$$\begin{aligned}\Delta x &= \frac{FOV}{N_x} \\ \Delta y &= \frac{FOV}{N_y}\end{aligned}\tag{2.22}$$

where  $N_x$  and  $N_y$  are the number of samples in two encoding directions in Cartesian k-space. The resolutions are thus correlated to the spatial frequency as:

$$\begin{aligned}\Delta x &= \frac{1}{\Delta k_x N_x} = \frac{1}{2k_{xmax}} \\ \Delta y &= \frac{FOV}{\Delta k_y N_y} = \frac{1}{2k_{ymax}}\end{aligned}\tag{2.23}$$

In a non-Cartesian radial sampling scheme, all the acquired k-space samples are located on polar coordinates. The phase encoding gradient in the Cartesian sampling

scheme is replaced by another frequency encoding gradient in the non-Cartesian sampling scheme. A standard 2D radial sampling pulse sequence diagram and corresponding k-space sampling trajectories are shown in Figure 2-7.

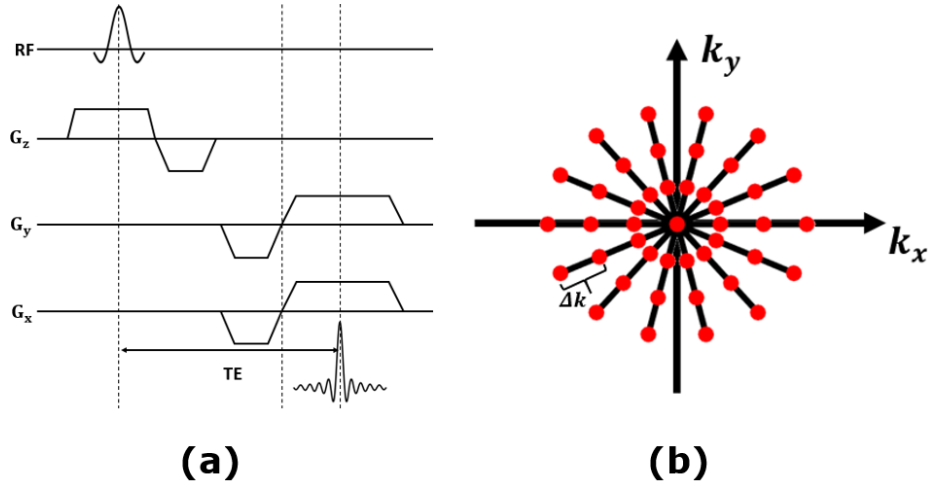


Figure 2-7: (a) A standard 2D radial sampling pulse sequence diagram. (b) 2D radial sampling trajectories in k-space.

Two frequency encoding gradients  $G_x$  and  $G_y$  are turned on simultaneously in radial sampling. An effective gradient vector  $G$  is produced and expressed as:

$$G = \sqrt{G_x^2 + G_y^2} \quad (2.24)$$

The magnitude of the effective encoding gradient  $G$  is kept constant while the strength ratio between  $G_x$  and  $G_y$  are adjusted during data acquisition. The change of strength ratio between two frequency encoding gradients rotates the sampling trajectory by a certain degree  $\theta$  in k-space as:

$$\theta = \tan^{-1} \frac{G_x}{G_y} \quad (2.25)$$

Through increasing  $\theta$  gradually from  $0^\circ$  to  $180^\circ$ , the radial sampling scheme achieves a relatively uniform coverage of k-space. The radial sampling only contains a k-space interval  $\Delta k$  while a circular FOV is produced by radial sampling:

$$FOV = \frac{1}{\Delta k} \quad (2.26)$$

Similar to the Cartesian sampling scheme, the k-space interval in radial sampling is supposed to satisfy a certain condition to avoid aliasing artefacts as:

$$\Delta k \leq \frac{1}{D} \quad (2.27)$$

Here  $D$  presents the maximum size of imaging object in all the circular directions. Meanwhile, radial sampling offers high sampling density and low sampling density in the k-space center and outer k-space respectively. The improvement of sampling density in the outer k-space region is achieved by increasing the number of radial spokes. Hence the angle between adjacent spokes is reduced. Compared to the Cartesian sampling, more spokes are required to satisfy the Nyquist standard (33) in radial sampling, expressed as:

$$n_\theta = \frac{\pi}{2} n_x \quad (2.28)$$

where  $n_\theta$  and  $n_x$  are the number of radial spokes (spoke degrees) and the number of sample points in each spoke respectively. Similar to the Cartesian scheme, the 2D radial sampling scheme can be extended into the 3D version by integrating the third frequency encoding gradient on partition dimension, forming a 3D radial sampling scheme. It is also available to integrate a phase encoding gradient on

partition dimension in the radial sampling scheme to produce a 3D hybrid stack-of-stars radial sampling scheme.

## 2.6 Non-Cartesian Reconstruction

For the Cartesian sampled k-space, images can be directly reconstructed by the FFT function. Due to the non-uniform distribution of samples in the non-Cartesian k-space, the FFT cannot be directly used for reconstruction in radial sampling. The Non-uniform Fast Fourier Transform (NUFFT) has been developed for reconstructing images from the non-Cartesian k-space. In NUFFT, the non-Cartesian k-space is gridded into Cartesian sampled k-space and then reconstructed by the FFT function (34-36). During the gridding procedure, sampled data is converted from polar coordinate to Cartesian coordinate by a convolution kernel. According to the Equation 2.18, the theoretically continuous 2D MR signals  $M(k_x, k_y)$  can be expressed as:

$$M(k_x, k_y) = \iint m(x, y) e^{-i2\pi(xk_x + yk_y)} dx dy \quad (2.29)$$

The discrete sampling function  $S(k_x, k_y)$  in k-space consists of a series of Dirac functions which is given by:

$$S(k_x, k_y) = \sum_j \delta^2(k_x - k_{x,j}, k_y - k_{y,j}) \quad (2.30)$$

The ultimate acquired discrete k-space samples can be regarded as a multiplication result of  $M(k_x, k_y)$  and  $S(k_x, k_y)$ , given by:

$$M_s(k_x, k_y) = M(k_x, k_y) \cdot S(k_x, k_y) \quad (2.31)$$

In radial sampling, the sampling function  $S(k_x, k_y)$  is not uniformly distributed in Cartesian coordinate. The acquired radial points can be convolved with a certain kernel function to recover the continuous MR signals  $M_{sc}(k_x, k_y)$  as:

$$M_{sc}(k_x, k_y) = M_s(k_x, k_y) * C(k_x, k_y) \quad (2.32)$$

where  $C(k_x, k_y)$  is the convolution kernel function. Consecutively, a re-sampling function with equally spaced delta functions in Cartesian coordinate is implemented to obtain the Cartesian sampled k-space  $M_{scs}(k_x, k_y)$  as:

$$M_{scs}(k_x, k_y) = M_{sc}(k_x, k_y)R(k_x, k_y) \quad (2.33)$$

where the  $R(k_x, k_y)$  is the re-sampling function with equally spaced delta function and can be mathematically expressed as:

$$R(k_x, k_y) = \sum_a \sum_b \delta^2(k_x - a, k_y - b) \quad (2.34)$$

The overall process to map the non-Cartesian sampled data into the Cartesian scheme can be simplified as:

$$M_{scs}(k_x, k_y) = \{[M(k_x, k_y) \cdot S(k_x, k_y)] * C(k_x, k_y)\} \cdot R(k_x, k_y) \quad (2.35)$$

Ultimately, images can be reconstructed from the gridded k-space directly by FFT function. According to the definition of Fourier transform, the multiplication and convolution are reversed between frequency domain and spatial domain. The gridding process equation can be expressed in spatial domain as:

$$m_{scs}(x, y) = \{[m(x, y) * s(x, y)] \cdot c(x, y)\} * r(x, y) \quad (2.36)$$

It is obvious that two additional weighting coefficients  $c(x, y)$  and  $s(x, y)$  are introduced to the reconstructed image which leads to the artifact and unexpected spatial intensity modulation (apodization). The convolution kernel  $c(x, y)$  directly modulated the gray level among the imaging region. Therefore, the selected kernel function is supposed to provide a flat profile among the imaging domain, reducing the apodization effect. The ideal kernel function for gridding is infinite Sinc function kernel which provides the square profile in spatial domain without additional signal intensity modulation. However, the infinite Sinc function is unavailable in practice. Jackson compared several kernel functions with finite size for gridding and obtained that the transformed spatial profile of Kaiser-Bessel function is closest to infinite Sinc kernel function (36). The Kaiser-Bessel function is given by:

$$\frac{1}{D} I_0 \left[ \beta \sqrt{1 - \left( \frac{2u}{D} \right)^2} \right] \quad (2.37)$$

where  $D$  is the kernel width and  $\beta$  is a free parameter.  $I_0$  is a constant which defines the magnitude of the kernel.  $u$  is another parameter to control the profile of Kaiser-Bessel kernel whose magnitude is supposed to be smaller than  $D/2$ .

Even though the Kaiser-Bessel kernel is implemented for convolution, the apodization is still existing in the imaging region. To further alleviate the apodization effect, two-times gridding technique has been proposed. The sample intervals  $\Delta k_x$  and  $\Delta k_y$  in re-gridded k-space are reduced by half while the matrix size of final reconstructed image is doubled during gridding process. The reduction

of k-space interval leads to a double of imaging FOV. The central section of reconstructed images which corresponds to the initial imaging FOV is extracted. The extracted matrix corresponds to the relatively flat band of the Kaiser-Bessel kernel, reducing the apodization effect caused by convolution further.

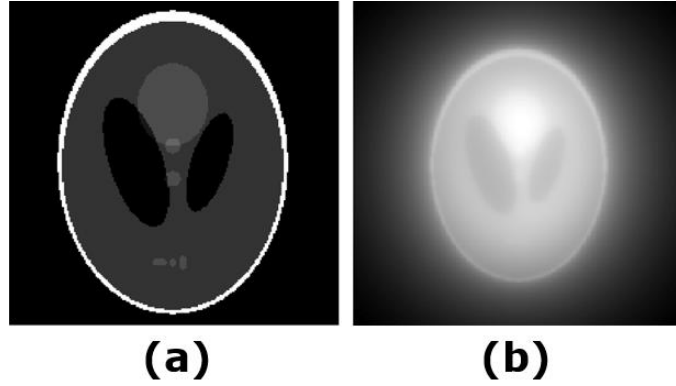


Figure 2-8: Blurring and excessive gray level occur in gridding algorithm without density compensation function: (a) The initial computation Shepp-logan model with a matrix size of 256\*256; (b) Gridding reconstruction of radial sampled phantom dataset with a larger FOV.

Meanwhile, sampling density of  $S(k_x, k_y)$  in central k-space is much higher than the outer region in radial sampling, leading to excessing magnitude accumulation at low frequency components during gridding. The blurring and excess gray level occur in final reconstructed images as shown in Figure 2-8.

To tackle with the blurring artifact, a density compensation function (DCF) is indispensable to compress the contributions from low frequency components. Typically, the DCF is implemented before or after convolution procedure in gridding algorithm. The final re-sampled k-space data with DCF is presented by:

$$M_{scs}(k_x, k_y) = \frac{1}{W(k_x, k_y)} \cdot M_{sc}(k_x, k_y) \cdot R(k_x, k_y) \quad (2.38)$$

Here  $W(k_x, k_y)$  presents the DCF for acquired k-space data in a non-Cartesian sampling scheme. Initially, the DCF can be simply obtained by weighting factors which are directly proportional to the square of the distance from sampled data to k-space center while the DCF can also be obtained by computing a Voronoi diagram of the trajectory (35,37).

## Chapter 3 MRI Acceleration

MRI can provide the image with high spatial resolution and multi-contrast for clinical diagnosis. However, the conventional MRI pulse sequences (GRE, SE, etc.) require period ranges from dozens of seconds to minutes to complete the data acquisition. Consequently, the MRI has worse temporal resolution compared with CT and X-ray. The excessive scan duration also leads to poor medical experience for patients. In this chapter, some acceleration techniques including parallel imaging, compressed sensing and compressed SENSE are introduced briefly. Several experiments are implemented to certificate the robustness of compressed sensing for highly accelerated MRI reconstruction

### 3.1 Parallel MRI

The MRI imaging speed can be improved by employing advanced hardware systems. With faster gradient switching rates, more frequent RF excitations and stronger gradient field, the scan time is reduced effectively in MRI. However, the overall acceleration rate highly relies on the property of the hardware system.

Reducing the number of samples in acquisition (undersampling) is an effective method to accelerate MRI imaging. Partial Fourier imaging is one of the simplest acceleration techniques which approximately reduce the number of k-space lines by half (13-15). The missing k-space samples are derived by exploring the conjugate symmetry property of the acquired k-space. The overall AF in Partial Fourier imaging is limited to be less than 2.

Parallel imaging is another robust acceleration method which accelerates imaging speed by exploring field maps information among receiving coil channels (16-19). During the MRI scan, a phased array coil with multiple sub-channel elements surrounding the imaging object is employed to acquire the excited MR signals. The MR signals are acquired by these coil elements simultaneously while the receiving MR signals are modified by an adequate receiving sensitivity field map in the certain coil channel. The field map difference among receiving channels offers additional encoding information which can be used to derive the missing samples in undersampled k-space or remove aliasing artefacts in spatial domain. In past decades, a variety of parallel imaging techniques like SMASH, SENSE and GRAPPA, etc. have been developed and widely implemented in clinical MRI now.

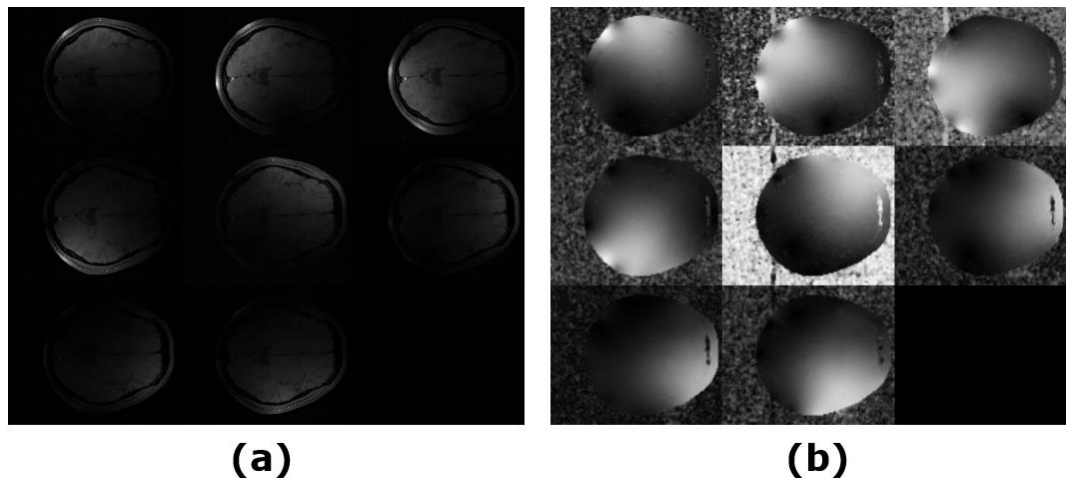


Figure 3-1: (a) An example of 8-channel brain images. The inhomogeneous intensity distribution is induced by the receiving sensitivity maps of coil channels. A relatively homogenous brain image can be recovered by sum-of-square (SOS) of the multi-channel brain images. (b) Corresponding receiving sensitivity maps of receiving coil elements estimated by Walsh algorithm.

Parallel imaging like SENSE requires accurate sensitivity field maps of receiving coil channels to derive missing k-space samples. The receiving sensitivity maps depend on both the geometry structure of coil arrays and imaging objects. These field sensitivity maps can be obtained by implementing an individual pre-scan or applying post imaging processing techniques like Walsh algorithm (38) and ESPIRiT (39) on the reference k-space kernel. Figure 3-1 shows a series of reconstructed brain images from different receiving coil channels and their corresponding field maps estimated by Walsh algorithm. Figure 3-2 shows the principle of signal intensity modifications from receiving channels.

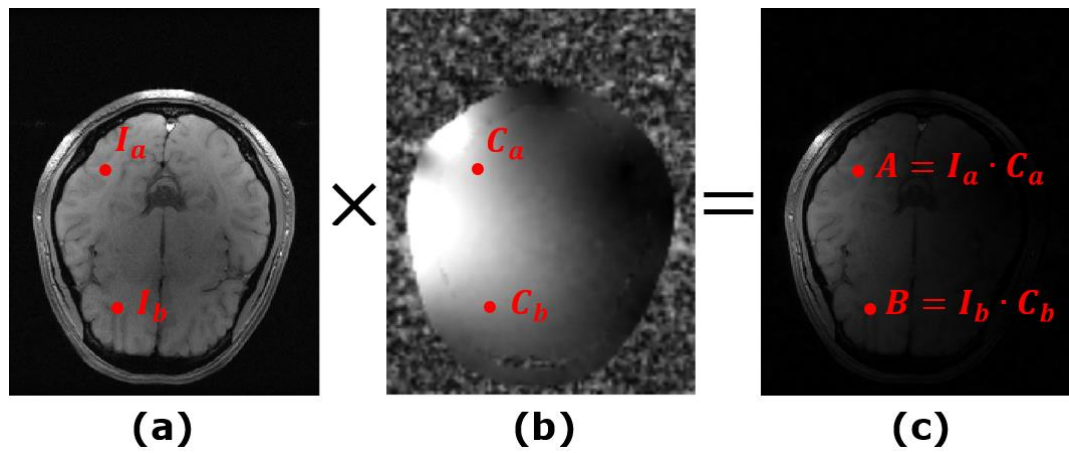


Figure 3-2: Brain image weighted by a coil receiving sensitivity map: (a) Initial brain image. (b) Receiving sensitivity map of a certain coil element. (c) Ultimate reconstructed brain image in this channel.

In Figure 3-2,  $I_A$  and  $C_A$  indicate the initial signal intensity and corresponding receiving sensitivity factor at spatial position  $A$ . The ultimate intensity presents at position  $A$  is modified by the field map as  $I_A \cdot C_A$ .

Regular undersampling leads to an increased  $\Delta k$  in k-space and reduced FOV in spatial domain respectively. Aliasing artefacts are consequently produced in the

reconstructed images. Aliasing artefacts indicate that the information of several pixels is overlapped at a single pixel. The number of pixels involved in overlapping is directly determined by the undersampling ratio or AF. For instance, with the AF=2, all the pixels are aliased with 2 correlated pixels as:

$$S = I_A + I_B \quad (3.1)$$

Here  $S$  presents the signal intensity of a certain pixel aliased by two pixels  $A$  and  $B$ . With additional receiving field maps encoding, the acquired signal in two coil channels can be expressed as:

$$\begin{aligned} S_1 &= C_{A1} \cdot I_A + C_{B1} \cdot I_B \\ S_2 &= C_{A2} \cdot I_A + C_{B2} \cdot I_B \end{aligned} \quad (3.2)$$

where  $S_1$  and  $S_2$  are the signal intensity of the pixel  $S$  in coil channels 1 and 2.  $C_{A1}$ ,  $C_{A2}$ ,  $C_{B1}$  and  $C_{B2}$  are the sensitivity coefficients of the aliased pixels  $A$  and  $B$  in two coil channels. The overlapped pixels can be decomposed by solving the group of Equation 3.2 above while an image can be reconstructed without aliasing artefacts in SENSE. However, the number of coil channels is typically much larger than 2 in practice, leading to a more complicated equation group.

It is available to simplify the expression of acquired multi-channel MR signals in a matrix format. The acquired signal can be generalized as:

$$S = E \cdot m \quad (3.3)$$

where  $S$  is the acquired multi-coil MR signal vector,  $m$  presents the image vector to be reconstructed.  $E$  is the multiple coil encoding matrix. The non-aliased images

can be reconstructed from regular undersampled k-space by solving an optimization problem as:

$$\operatorname{argmin}_m = \|E \cdot m - s\|_2^2 \quad (3.4)$$

Theoretically, the AF in SENSE is limited by the number of coil channels. However, the noise level in the reconstructed images is increased when the higher undersampling ratio is used. The amplification of noise in parallel imaging is determined by receiving coil design and expressed by an equation as:

$$SNR = \frac{SNR_0}{g\sqrt{R}} \quad (3.5)$$

Where  $SNR_0$  is the baseline of SNR of the MRI system and  $g$  is the geometry-factor (g-factor) which is related to the design of coil structure (40). The SNR in parallel imaging is inversely proportional to the undersampling ratio.

### 3.2 Compressed Sensing

Compressed Sensing was initially reported by Donoho in 2006 (20) and it was applied for under-sampling MRI reconstruction soon by Lustig in 2007 (21). In past decades, a variety of compressed sensing based acceleration techniques has been released for highly undersampled MRI reconstruction.

The basic principle of compressed sensing is based on the fact that majority of digital images including medical images are typically compressive with appropriate transform like DWT and TV (21,22). Images are expressed sparsely in these transform domains. Power is mainly concentrated on a few transform coefficients while other transform coefficients have negligible power. Inversely, a few

transformed coefficients are sufficient to recover the images with negligible loss of details while it offers the compression availability for highly undersampled MRI reconstruction.

### 3.2.1 Sparse Representation in Measurement

Similar to the parallel imaging, the undersampled MR signals in compressed sensing can be simply expressed in a matrix format as:

$$s = \Phi \cdot m \quad (3.6)$$

where  $s$  is a measured signal vector with the size  $M \times 1$  and  $m$  presents an initial signal vector with the size  $N \times 1$ .  $\Phi$  is the sampling matrix with the size  $M \times N$ . In fully sampled MRI, the number of measurements is equal to the size of signal as  $M = N$ .

Undersampling is achieved by implementing fewer measurements than the signal size as  $M < N$ . Consequently, there are multiple solutions existing in Equation 3.6 if matrix  $\Phi$  has full rank. However, it is practical to recover the signal vector from insufficient measurement when the signal can be expressed sparsely.

In a  $K$ -sparse signal, the majority of signal components are zero while at most  $K$  signal components are non-zero. Therefore, the size of measurement matrix  $\Phi$  can be reduced from  $M \times N$  to  $M \times K$  and thus a new measurement matrix  $\Phi_K$  is generated. The  $K$ -sparse signal  $m$  is expressed as  $m_K$ . The measured signals become:

$$s = \Phi_K \cdot m_K \quad (3.7)$$

The intrinsic sparse signal is relatively rare in practice. However, a variety of signals including MR signals can be expressed sparsely with an appropriate sparse transform  $\Psi$ . The signal is then expressed as:

$$m = \Psi x \quad (3.8)$$

where  $x$  is the sparse representation of  $m$ . Figure 3-3 shows a sparse representation of a brain MRI image in DWT domain. The magnitude of majority of DWT coefficients are approaching zero as shown in Figure 3-3b.

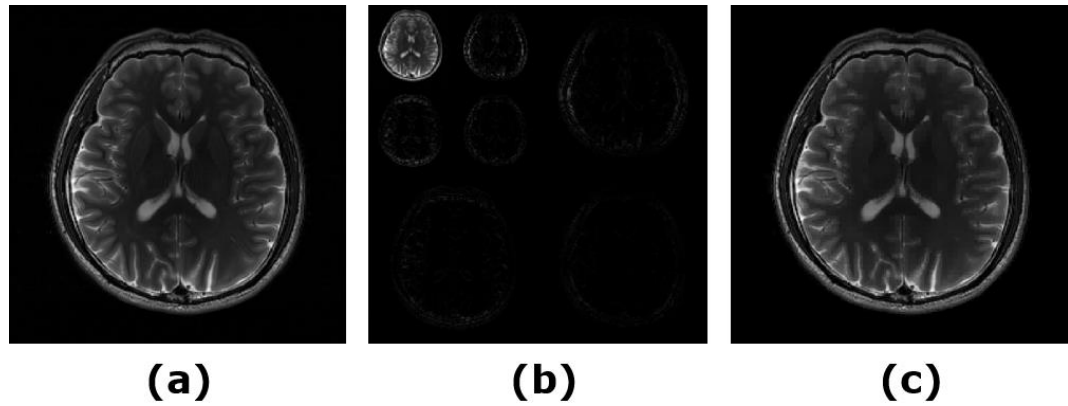


Figure 3-3: (a) The T1 weighted brain image. (b) Sparse representation of brain image in wavelet transform domain. Majority of DWT coefficients are approximately zero. (c) The brain image recovered from wavelet domain with 15% wavelet coefficients. The brain structure information was reserved effectively with about 6-fold smaller size.

The measured signal vector  $s$  can be expressed with the sparse representation as:

$$s = \Phi \Psi x \quad (3.9)$$

It can combine the sparse representation matrix  $\Psi$  and measurement matrix  $\Phi$  as a single matrix as  $A$ . The measured signal vector  $s$  is ultimately expressed as:

$$s = Ax \quad (3.10)$$

$A$  is required to obey the restricted isometry property (41), expressed as:

$$(1 - \delta_K)\|x\|_2^2 \leq \|Ax\|_2^2 \ll (1 + \delta_K)\|x\|_2^2 \quad (3.11)$$

Here  $\delta_K$  is the isometry constant which defines the performance of hybrid measurement matrix  $A$ . When the value of  $\delta_K$  approaches zero, the measurement matrix  $A$  causes less loss, ensuring the improved compressed sensing performance.

### 3.2.2 Sparse MRI

Restricted isometry property of matrix  $A$  is the golden standard to guarantee the recovery of sparse signals. However, verifying restricted isometry property is typically difficult due to the excessive computation cost. Another property named coherence of matrix  $A$  is implemented to evaluate the performance of compressed sensing. The mutual coherence describes the inner product between two columns in matrix  $A$  and it can be evaluated by calculating the Gram matrix ( $A^H A$ ) of  $A$ . High incoherence is achieved by the small diagonal entries in Gram matrix, leading to better recovery of sparse signals.

MR signals are acquired in the spatial frequency domain k-space in MRI. The measurement matrix is expressed as the sampling scheme. The matrix with less measurement is expressed as the partial Fourier encoding matrix in the case of undersampling. The parameter point spread function (PSF) of the sampling schemes is a nature tool to measure the incoherence of the measurement matrix (21). The PSF is a parameter to evaluate the interference between pixels in the spatial domain. It measures the contribution of a unit-intensity pixel at position  $i$  to a pixel at position  $j$  and can be expressed by:

$$PSF_{i,j} = e_j^* F_u^* F_u e_i \quad (3.12)$$

where  $e_i$  and  $e_j$  are the  $i$ th and  $j$ th vectors of the nature basis.  $F_u$  is the partial Fourier encoding operator. In fully sampled k-space, the interference between pixels is zero as  $PSF(i; j)|_{i \neq j} = 0$ . Undersampling in k-space causes pixels to be interfered with each other and non-zero value of  $PSF(i; j)|_{i \neq j}$ . The incoherence can be simply measured by the maximum of sidelobe-to-peak ratio (SPR), given by:

$$\max_{i \neq j} = \left| \frac{PSF(i, j)}{PSF(i, i)} \right| \quad (3.13)$$

Regular undersampling is employed in parallel imaging for accelerating data acquisition. However, larger magnitude is induced on sidelobes in PSF of regular sampling while multiple pixels are highly aliased. The poor incoherence of regular undersampling cannot satisfy the requirements of compressed sensing for recovering sparse signals. Unlike regular undersampling in parallel imaging, compressed sensing is implemented with a random or pseudorandom sampling pattern which achieves much better sampling incoherence. The energy of the acquired signals is highly concentrated on the low frequency components. Hence random sampling is preferred to take more measurements in the k-space center.

In 3D Cartesian MRI, the random sampling can be achieved in the phase encoding plane ( $k_y$ - $k_z$  plane). However, random sampling scheme is limited by the hardware system in 2D Cartesian MRI. Meanwhile, undersampling on the frequency encoding dimension does not reduce the acquisition time. Hence, random sampling is only performed on phase encoding dimension while the sampling incoherence is limited

in 2D Cartesian sampling. Non-Cartesian sampling schemes like radial sampling intrinsically contain more measurements in k-space center. The radial sampling scheme distributes undersampling interference among all the spatial directions, achieving high incoherence for better sparse signal recovery in compressed sensing.

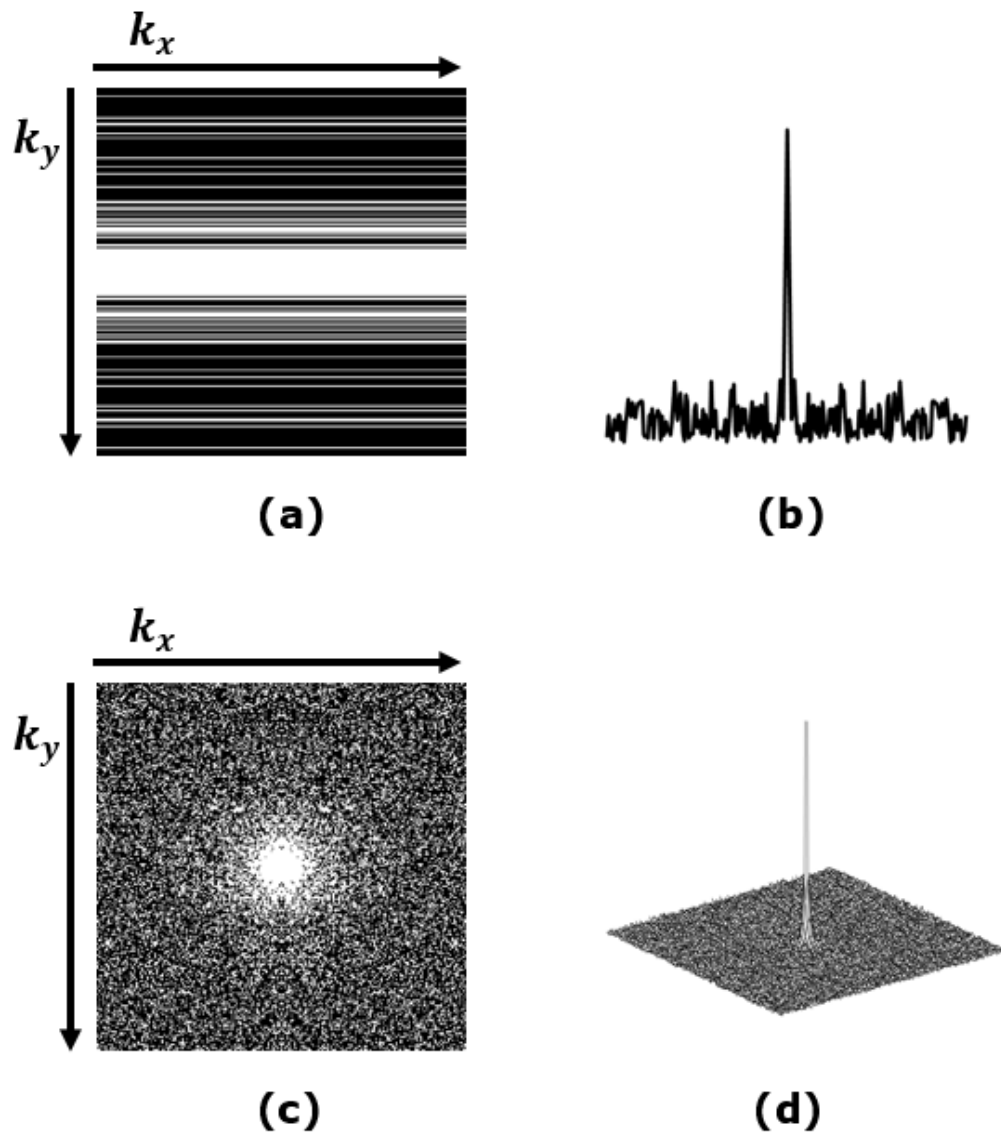


Figure 3-4: (a) Random sampling on phase encoding dimension in 2D Cartesian sampling. (b) Corresponding PSF of 2D Cartesian sampling scheme on phase encoding dimension. (c) 2D random sampling scheme. (d) PSF of the 2D random scheme with much better incoherence.

Figure 3-4 shows a comparison of the PSF in 2D Cartesian sampling scheme with random sampling on phase encoding dimension and 2D random undersampling scheme. Much better incoherence is achieved in 2D random undersampling. Besides the requirement of incoherence, sparse representation of the MR signals is required for the image recovery in compressed sensing. The sparsity of the signal vector can be measured the number of non-zero components, expressed by its  $L_0$  norm as:

$$\|x\|_0 = \sum_i |x_i|^0 \quad (3.14)$$

The sparse signal  $x$  is recovered by minimizing the  $L_0$  norm in compressed sensing as:

$$\begin{aligned} \operatorname{argmin}_x &= \|x\|_0 \\ \text{s. t. } s &= \Phi\Psi x = Ax \end{aligned} \quad (3.15)$$

In consideration of noise in the measurements, the Equation 3.15 is converted with a  $L_2$  norm as:

$$\begin{aligned} \operatorname{argmin}_x &= \|x\|_0 \\ \text{s. t. } \|s - Ax\|_2^2 &\leq \epsilon \end{aligned} \quad (3.16)$$

where  $\epsilon$  presents the estimated noise level.  $L_2$  norm is a measurement of data consistency between reconstruction results and measurements. The signal vector  $m$  shows the sparsity in an appropriate transform domain. Hence, the MRI images can be recovered by solving the equations as:

$$\begin{aligned} \operatorname{argmin}_f &= \|\Psi^H m\|_0 \\ \text{s. t. } \|s - \Phi m\|_2^2 &\leq \epsilon \end{aligned} \quad (3.17)$$

where  $H$  presents the Hermitian conjugate. Minimizing  $L_0$  norm is an NP-hard problem and leads to intensive computation. In consideration of computation cost, a  $L_1$  norm is used to replace the  $L_0$  norm if certain conditions are satisfied (41).

$$\begin{aligned} \operatorname{argmin}_f &= \|\Psi^H m\|_1 \\ \text{s. t. } &\|s - \Phi m\|_2^2 \leq \epsilon \end{aligned} \quad (3.18)$$

In practice, the constrained minimization problem is converted into an unconstrained format by using Lagrange multipliers as:

$$\operatorname{argmin}_m = \|s - \Phi m\|_2^2 + \lambda \|\Psi^H m\|_1 \quad (3.19)$$

Here  $\lambda$  is a penalty factor which trades off data fidelity and sparsity representation in  $L_2$  norm and  $L_1$  norm respectively. The MR signals are encoded in a Fourier transformed format by delicate gradient encoding, the Equation 3.19 is thus converted into MRI format as:

$$\operatorname{argmin}_x = \frac{1}{2} \|Fx - b\|_2^2 + \lambda \|Tx\|_1 \quad (3.20)$$

Here  $x$  presents the images to be reconstructed and  $F$  is the undersampled Fourier operator.  $T$  is a sparsity transform and typically selected as TV or DWT in MRI. The optimization problem in Equation 3.20 can be solved by Non-linear Conjugate Gradient (NLCG) descent (42), iterative shrinkage and thresholding algorithm (ISTA) (43) and fast iterative shrinkage and thresholding algorithm (FISTA) (44), etc.

### 3.2.3 Compressed SENSE

In practice, the receiving field map of an individual coil channel is limited. MR signals are acquired by multiple coil channels simultaneously. By SOS combination of multi-channel datasets, the SNR and field map homogeneity are improved in MRI. The conventional compressed sensing reconstruction is applied coil-by-coil which experiences the intensive computation burden and interference from low SNR. The compressed sensing can be combined with the parallel imaging which in the SENSE, formed compressed SENSE, for a faster and better sparse recovery (45,46). The compressed SENSE framework contains additional field map information than standard compressed sensing as:

$$\operatorname{argmin}_x = \frac{1}{2} \|FCx - b\|_2^2 + \lambda \|Tx\|_1 \quad (3.21)$$

where  $C$  represents the multi-channel field maps. With estimated field map information, compressed SENSE reconstructs multiple channel datasets simultaneously instead of channel-by-channel reconstruction. Meanwhile, the performance of compressed sensing highly relies on the incoherence of undersampling schemes. The additional field maps encoding is helpful to further increase the undersampling incoherence (46).

## 3.3 Simple Applications of Compressed Sensing

The experiments of compressed sensing were implemented on a  $T_1$ -weighted brain dataset provided by Huang (47). The matrix size of the brain image is 256\*256. Two resolution phantom datasets were acquired by the 2D FLASH based radial sampling scheme on a 3.0T super-conduct scanner (Philip Achieva, Philip Medical

Systems, Best, Netherland) equipped with a 30-element head array coil. The matrix size of these two phantom datasets were 384 readout points \* 200 spokes \* 30 channels and 384 readout points \* 18 spokes \* 30 channels respectively. The corresponding AF for these two phantom datasets was 3 and 33 respectively.

Figure 3-5 shows the procedures of a random undersampling simulation on the T1-weighted brain dataset. Random sampling scheme achieves a relatively ideal incoherence while noise-like artefacts are induced on the brain image. These noise-like artefacts have negligible power in the sparse transform domain like DWT.

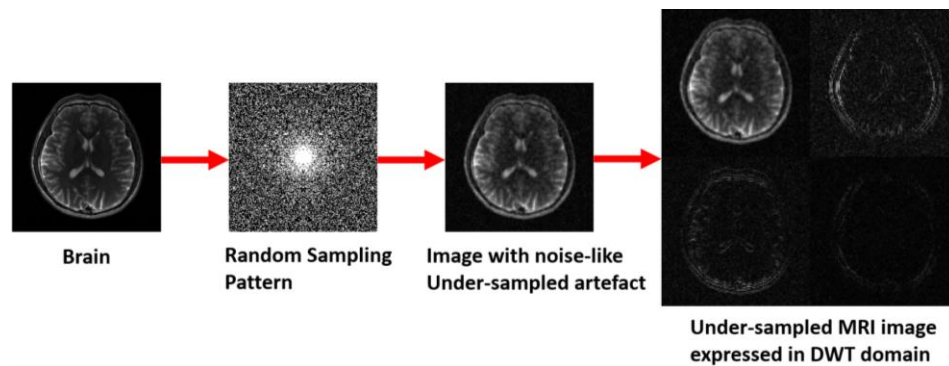


Figure 3-5: Basic procedure of simulation of the compressed sensing. Random undersampling pattern induces noise-like artefacts while these artefacts have negligible power in the DWT domain.

Figure 3-6 shows the reconstruction results of a simulated brain dataset at AF=6. Basic brain structures were recovered and noise-like undersampling artefacts were compressed successfully by compressed sensing. As MRI images were not completely sparse in the DWT domain, some detailed information was lost due to the filtering of small coefficients in DWT domain.

Figure 3-7 shows the generation of an additional multi-channel brain dataset by introducing additional 4 virtual field maps. Both initial brain dataset and 4-channel

brain dataset were undersampled by a uniform radial sampling pattern at  $AF=4$  and reconstructed by standard compressed sensing and compressed SENSE respectively.

Figure 3-8 shows a comparison of error maps to the reference brain image in compressed sensing and compressed SENSE. Using the initial brain image as the reference, the Root Mean Square Error (RMSE) in compressed sensing and compressed SENSE were 0.0128 and 0.0107 respectively. Better brain structures and fewer relative errors were observed in Compressed SENSE.

Figure 3-9 shows the performance of compressed SENSE for reconstructing the highly undersampled phantom dataset. The multi-channel field maps were estimated by ESPIRiT algorithm (39). The radial sampling scheme offered high incoherence while there was no obvious artefact observed in the image reconstructed by the NUFFT at  $AF=3$ . The structure and contrast of the resolution phantom were relatively simple, showing high sparsity in the sparse domain. Even if significant artefacts were induced on the image at  $AF=33$ , the phantom structure was still successfully recovered by compressed SENSE with few residual artefacts.

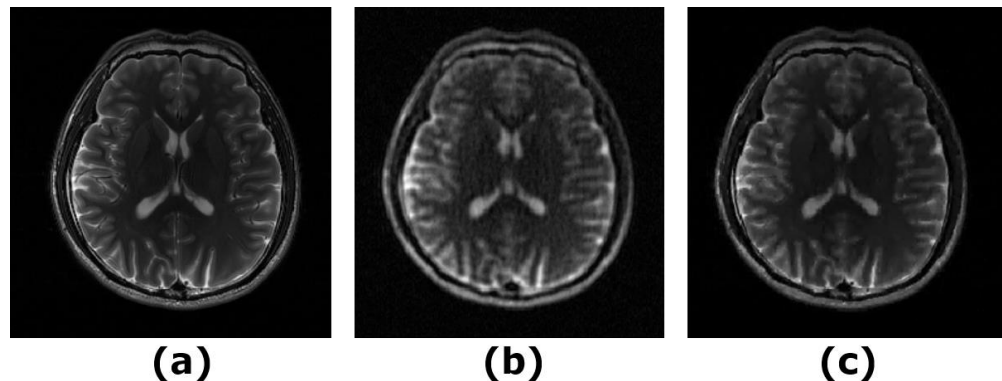


Figure 3-6: (a) Fully sampled reference brain image. (b) Randomly undersampled brain image at  $AF=6$ . (c) Brain image reconstructed by compressed sensing at  $AF=6$ .

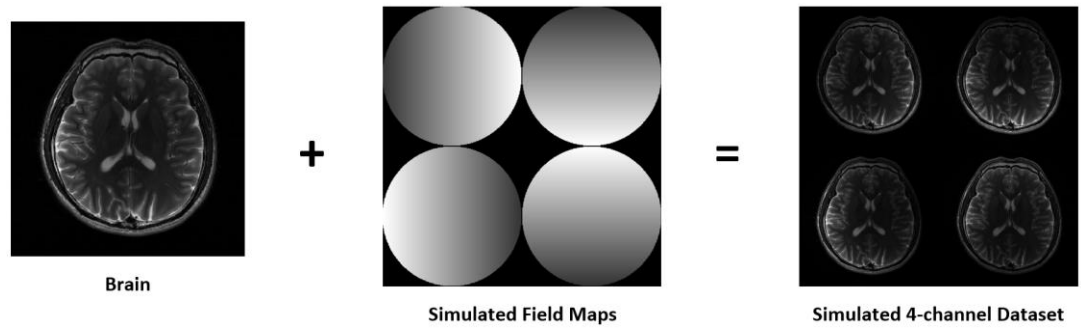


Figure 3-7: Simulation about producing a multi-channel brain MRI dataset with virtual receiving sensitivity maps.

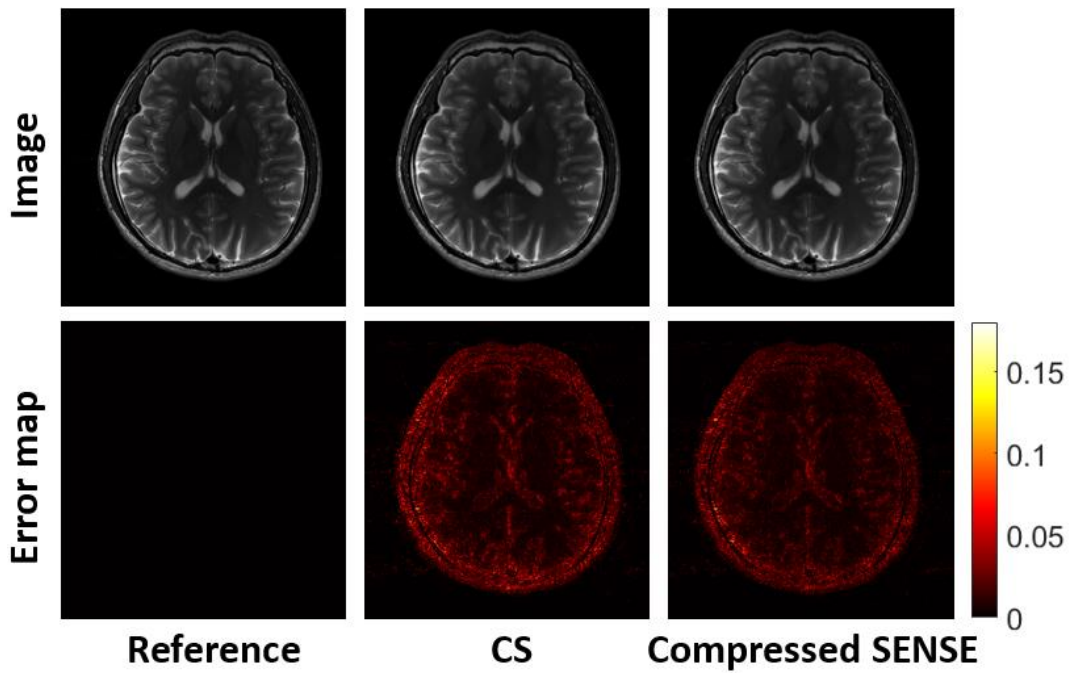


Figure 3-8: A comparison of compressed sensing and compressed SENSE in reconstructing a radial undersampled brain image at  $AF=4$ . Compared to the reference, fewer errors were observed in compressed SENSE

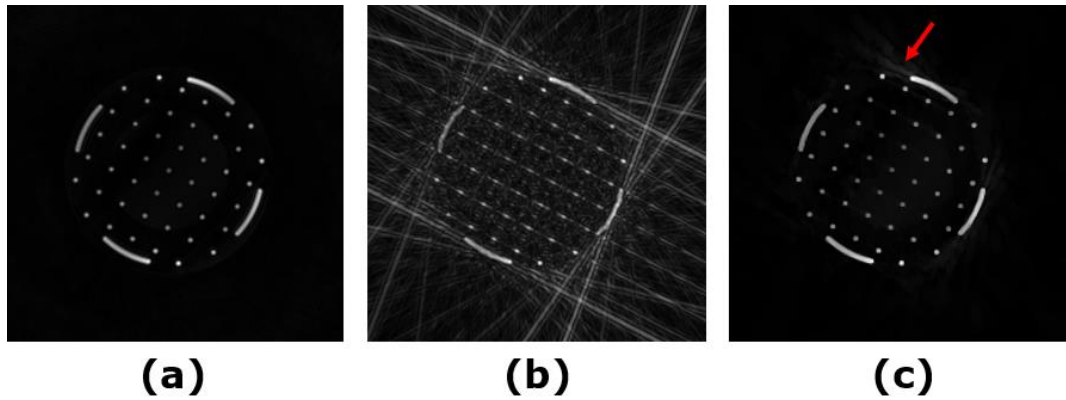


Figure 3-9: (a) NUFFT reconstruction of phantom dataset acquired by radial sampling pattern at  $AF=3$ . (b) NUFFT reconstruction of phantom dataset acquired by radial sampling pattern at  $AF=33$ . (c) Phantom image reconstructed by compressed SENSE at  $AF=33$ . The residual undersampling artefacts are labelled by a red solid arrow.

### 3.4 Conclusion

Parallel imaging accelerates the MRI data acquisition by utilizing the additional field map encoding information from receiving coil channels. Increased  $AF$  is achieved at the expense of SNR in parallel Imaging. By exploring the sparsity of MRI images, compressed sensing reduces the number of measurements effectively. The combination of compressed sensing and parallel imaging shows the robustness for reconstructing MRI images from the highly undersampled  $k$ -space.

## Chapter 4 Stack-of-Stars Central Out Golden Angle UTE Imaging

During MRI scans, the excited net magnetization vector  $M_{xy}$  of tissues decayed at a variety of rates due to the different proton densities and tissue structures. The parameter TE which presents the duration between signal excitation and the acquisition of k-space center decides the amount of decay for the tissue signal. In the conventional pulse sequence like SE and GRE, the minimum TE is limited as milliseconds which is sufficiently small for imaging the general tissues. However, from the earliest days of clinical MR, it was recognized that there were tissues with extremely short  $T_2$  (typically  $<1\text{ms}$ ), including cortical bone, tendons and ligaments, etc (48). The excited signal of these tissues will experience significant decay before the data acquisition in conventional pulse sequences. Consequently, these tissues become invisible in final reconstructed images, resulting in the loss of significant diagnosis information. Though, with the development of fast gradient echo pulse sequences, the shorter TE about 1 ms is now available. For the tissues with  $T_2$  below 1 ms, the final image quality is still degraded due to the significant signal decay.

To image the tissues with extremely short  $T_2$  value, UTE and zero time-echo (ZTE) techniques have been developed based on the non-Cartesian sampling pattern. Both ZTE and UTE start to acquire data as soon as possible after RF excitation, leading to central out k-space trajectory (49,50). Unlike UTE, ZTE turns on the readout gradients prior to the RF excitation while the TE is theoretically approaching zero. The readout gradients in ZTE are gradually varied for fulfilling the k-space. These

readout gradients are not switched off until completing the data acquisition. Hence, ZTE can reduce the acoustic noise caused by gradient switching effectively (50). However, the center of k-space in ZTE is crossed due to switching of hardware from transmit to receive mode. ZTE typically requires support from additional imaging protocols like single-point imaging to acquire the k-space center (51). High performance hardware is required for ZTE to support the hybrid acquisition model. Meanwhile, ZTE is limited for the full excitation 3D imaging due to this special acquisition model (49).

Compared to ZTE, UTE can achieve similar contrast and SNR efficiency for volumetric imaging of ultrashort- $T_2$  components (49,52). UTE can achieve the 2D imaging and 3D imaging with limited FOV by half pulse excitation and slab selective excitation respectively. The feasibility of imaging volume in UTE is a significant merit for clinical application. Furthermore, UTE is less sensitive to the hardware performance and can be used for the low field (<3T) MRI imaging.

Currently, there are three main designs of the pulse sequence to achieve the UTE imaging, including 2D slice-selective UTE imaging (6,7), 3D non-selective UTE imaging (9,53,54) and hybrid 3D UTE imaging (11,12,26,55-57). In this chapter, three kinds of UTE techniques are introduced briefly. A modified stack-of-stars central out golden angle radial sampling pulse sequence has been proposed for 3D UTE imaging. A pre-scan method is used to calibrate the sampling trajectory while an iterative DCF is implemented to improve the reconstruction quality.

## 4.1 2D UTE Imaging

In conventional Cartesian or non-Cartesian sampling pulse sequences, the k-space is gradually filled from  $-k_{max}$  to  $k_{max}$  with the pre-dephasing section of the readout gradient. In 2D slice selective imaging, a short TE can be achieved by implementing the non-Cartesian sampling (typically radial sampling) without the pre-dephasing gradient. The data acquisition is started simultaneously with the ramping up of readout gradient. The first sample point is not encoded by any gradients, presenting the central point of k-space. The sampled data is distributed non-uniformly on acquired spokes as well. The frequency gap between two adjacent samples is increased continuously until the readout gradient arrives at a constant strength.

RF pulse excitation is another factor which extends the TE significantly. Sufficient duration is desired for RF to excite a 2D profile with acceptable thickness while a refocusing gradient on slice dimension is required. Half pulse excitation technique is developed in 2D UTE to minimize the effective TE further. Two half RF pulses are used for excitation under the opposite selection gradients. The frequency leakage caused by truncation of half RF pulse is also removed in the combined profiles (6,7).

To maintain the excited profile and remove refocusing gradient completely, Variable-Rate Selective Excitation (VERSE) pulse has been developed to excite the MR signals during ramping down of the selective gradient (58,59). Currently, a minimum 8  $\mu$ s TE has been achieved in 2D UTE imaging with a special design of coil systems. Figure 4-1 shows a representative 2D UTE pulse sequence diagram with half pulse excitation and VERSE modification.

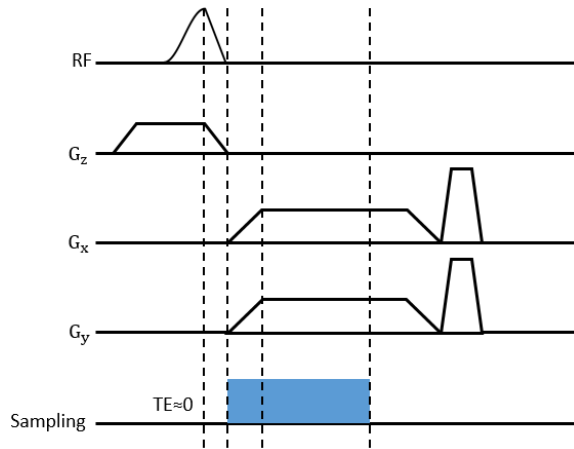


Figure 4-1: 2D UTE imaging sequence with a ramped half Gaussian soft pulse for excitation. The TE of the pulse sequence is theoretically approaching zero, limited by the switch duration of coil systems.

## 4.2 3D UTE Imaging

Compared with 2D slice-selective UTE imaging, 3D UTE imaging pulse sequence structure is relatively simple. A non-selective RF pulse with short duration is implemented to excite a volume in the absence of slice-selective gradients as shown in Figure 4-2. Besides the readout gradient on x-axis and y-axis in 2D radial encoding, another direction of the coordinate system z-axis has also been introduced as frequency encoding in 3D UTE imaging. The data acquisition starts accompanied with the ramping up of three readout gradients, forming 3D central out radial sampling. Through adjusting the ratio of gradient strength among three orthogonal directions delicately, the acquired spokes are available to fulfill the “sphere” k-space sufficiently (54). A time gap (typically <200us) is placed between the end of RF pulse and the start point of readout gradients to cover the dead time of coil receiving system (60,61). The minimum TE in 3D UTE imaging is mainly determined by this time gap.

3D imaging protocol offers intrinsic high SNR in UTE techniques. Meanwhile, the 3D UTE profiles can be reconstructed with an isotropic resolution which is desired for accurate clinical diagnosis.

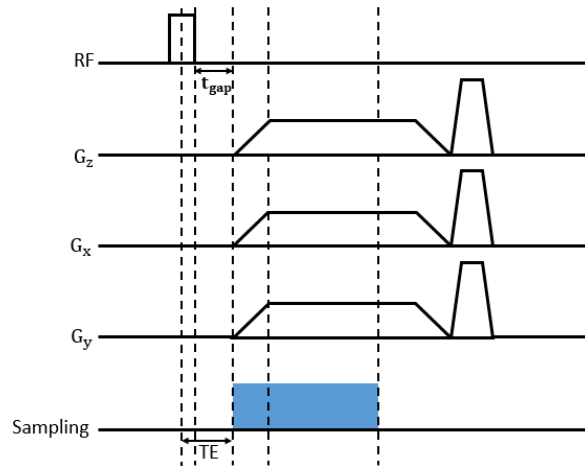


Figure 4-2: 3D UTE imaging pulse sequence diagram. Three readout gradients are implemented on x, y and z axes respectively, forming 3D central out radial sampling.

### 4.3 Hybrid 3D Sampling Pattern for 3D UTE Imaging

The data acquisition efficiency is degraded by half pulse excitation in 2D UTE and the excessive number of spokes is required in 2D UTE to satisfy the Nyquist sampling standard (7). Meanwhile, both half pulse excitation and VERSE modification are extremely sensitive to hardware imperfections (59). 3D UTE imaging offers intrinsic high SNR in MRI. By acquiring a sphere encoded k-space, a 3D image matrix can be reconstructed with an isotropic resolution. However, the time cost in both data acquisition and gridding reconstruction in 3D UTE is relatively large. The imaging acceleration is typically achieved by undersampling which degrades the image quality and induces streaking artefacts.

Besides two central out radial sampling based UTE imaging methods, a 3D hybrid sampling pattern called stack-of-stars sampling has been proposed for UTE imaging and become increasingly popular (11). This hybrid sampling achieves fast data acquisition and reconstruction simultaneously.

### **4.3.1 Stack-of-Stars Sampling**

Stack-of-stars sampling uses a selective RF pulse incorporated with a weak slice selective gradient to excite a segment of the imaging object. Instead of employing 3D radial sampling to achieve isotropic volumetric coverage, stack-of-stars sampling extends the conventional 2D radial sampling scheme into 3D acquisition scheme by adding an additional phase encoding gradient on the partition dimension (10). Hence, radial sampling and Cartesian sampling are employed in transverse  $k_x$ - $k_y$  plane and partition  $k_z$  dimension respectively in stack-of-stars sampling as shown in Figure 4-3, forming a hybrid 3D acquisition scheme.

The merit of this encoding scheme is the flexible selection of slab and slice thickness during acquisition and reconstruction. FFT is implemented to decouple the k-space of slices from the hybrid 3D dataset. NUFFT can be used to reconstruct each slice individually, offering much higher reconstruction efficiency than the conventional 3D radial sampling.

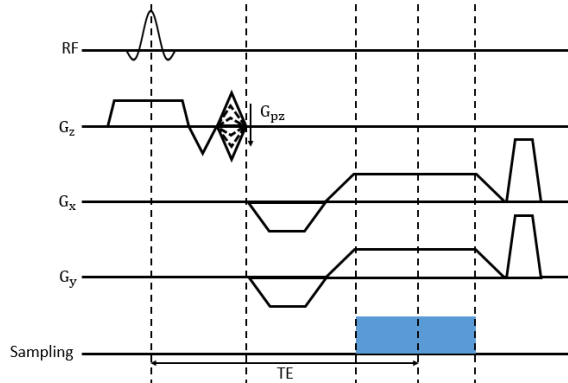
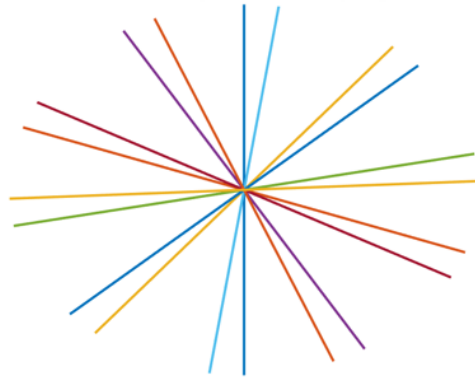


Figure 4-3: 3D stack-of-stars sampling pulse sequence diagram. Transverse plane and slice dimension are encoded by radial sampling and Cartesian sampling respectively. A shorter TE and TR can be achieved by combining the  $G_{pz}$  and refocusing section of slice selective gradient.

### 4.3.2 Golden Angle Radial Sampling

The general radial sampling rotates the spokes gradually to fulfill the k-space. Golden angle radial sampling is an advanced radial sampling technique which is typically implemented for accelerated MRI imaging. The angle between two adjacent acquired spokes is fixed and set as a golden angle (typically  $111.246^\circ$ ) which ensures approximately uniform coverage of k-space for any arbitrary number of consecutive spokes (10,29). Figure 4-4 shows a comparison between the conventional radial sampling pattern and the golden angle radial sampling pattern with only 10 spokes (the total number of spokes is 100). It is obvious that several spokes acquired by golden angle ratio can cover the k-space roughly.

### Golden Angle Radial Sampling



### Uniform Radial Sampling



Figure 4-4: A comparison of partial sampling pattern between uniform radial sampling and golden angle radial sampling. 10 spokes are selected from two radial sampling patterns with a total of 100 spokes. K-space is still roughly covered by a partial part of golden angle radial sampling.

Meanwhile, the spokes acquired by golden angle radial sampling will never be overlapped by other spokes. The overall acquired spokes can be subdivided into multiple temporal frames according to the time sequence. The sampling trajectories among subdivided frames are different which offers additional incoherence along the temporal dimension. Hence, golden angle radial sampling pattern is typically combined with compressed sensing for dynamic MRI reconstruction with high temporal-spatial resolution.

### 4.3.3 Stack-of-Stars Central Out Golden Angle UTE imaging

It is also practical to achieve the ultra-short TE in a hybrid stack-of-stars pattern by employing the central out radial sampling model. The design of stack-of-stars UTE is similar to the previous 3D UTE. A non-selective RF pulse with a short duration is employed to eliminate the slice selective gradients. The time gap between RF excitation data acquisition in conventional 3D UTE is occupied by the phase

encoding section on slice dimension in stack-of-stars UTE. Data acquisition starts immediately with ramping up of readout gradients after Cartesian phase encoding as shown in Figure 4-5. The minimum TE in stack-of-stars UTE is mainly determined by the duration of Cartesian phase encoding.

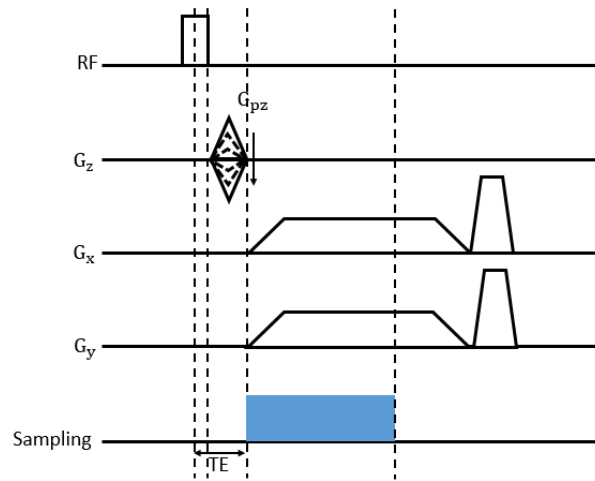


Figure 4-5: 3D stack-of-stars UTE pulse sequence diagram. TE is reduced by employing a short duration RF pulse and central out radial sampling pattern. The minimum TE is typically limited by the duration of phase encoding gradient  $G_{pz}$ .

#### 4.3.4 Stack-of-Stars UTE with Adaptive Time Echo

The minimum TE is also limited by the gradient systems in stack-of-stars UTE imaging. Shorter TE can be achieved by gradually reducing the phase encoding duration. However, gradient magnitude is supposed to be increased continuously to maintain the effective phase encoding while the protection system will be triggered by the excessive gradient strength. Hence, the minimum TE in stack-of-stars UTE is around 200  $\mu$ s which is typically larger than conventional 3D UTE.

To tackle with the limitation from phase encoding, an advanced stack-of-stars UTE with adaptive TE (56) has been proposed. For phase encoding, much smaller gradient magnitude and duration are required to encode central k-space than the outer k-space.

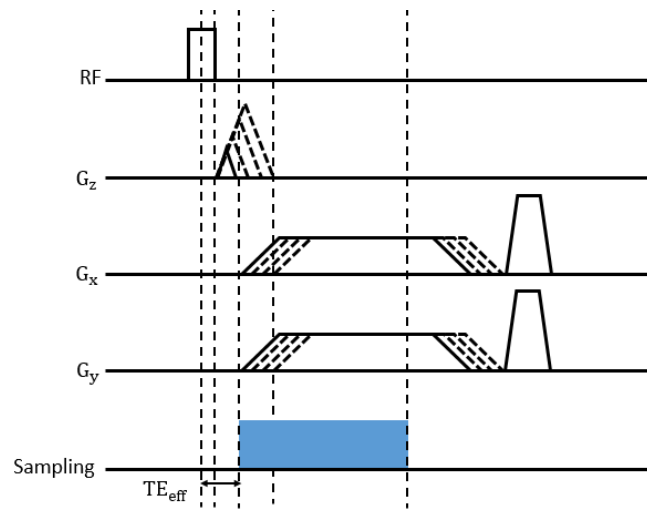


Figure 4-6: Advanced 3D stack-of-stars UTE pulse sequence diagram with adaptive TE. The duration of phase encoding gradient  $G_{pz}$  is increased gradually from central k-space to the outer k-space along the slice dimension. Minimum TE is achieved for k-space center which defines the basic image contrast.

Hence, an adaptive TE is achieved by gradually increasing the phase encoding duration on partition dimension from the central partition to the edge partitions in stack-of-stars UTE as shown in Figure 4-6. Therefore, the minimum TE is achieved for the central partition which defines the basic MRI image contrast. The minimum TE in this advanced stack-of-stars UTE is the same as conventional 3D UTE and only limited by the dead time of the coil system.

## 4.4 Trajectory Calibration

Hardware system imperfections like eddy current and timing delay induce gradient delay and gradient distortion. Consequently, the actual k-space trajectory deviates from the assumed one (62-64). In conventional Cartesian sampling, the deviation of samples in k-space just induces the additional phase modification in spatial domain while the reconstruction of magnitude map is not interfered (1). However, the radial sampling pattern contains multiple readout gradients among orthogonal directions while different deviations are induced among these readout directions. The gap of deviation results in a mismatch of readout gradients and thus induces significantly streaking artefacts.

In conventional radial sampling, k-space data is acquired at the constant section of readout gradient. The corresponding deviation of sampling trajectory is relatively stable and can be measured with pre-scans (65-67). Central out radial sampling acquires the central k-space data during ramping up of the readout gradient and thus it is much more sensitive to the gradient distortion and gradient delay. Here, we implemented a robust trajectory measurement method with additional signal shifting (68) to measure the actual sampling trajectory.

The trajectory measurement is achieved by acquiring MR signals from multiple slices located along the axis of the gradient of interest. Figure 4-7 shows the basic pulse sequence diagram for sampling trajectory measurement. A pair of slice selective gradients incorporates with a long duration of RF are implemented to excite the profile with extremely thin thickness. The following readout pattern is the same as the central out radial sampling for trajectory measurement. The slice

selected gradient and readout gradient are implemented at the same axis. If we use the  $x$ -axis as the example, the acquired signal  $S_i(k_x)$  can be expressed as:

$$S_i(k_x(t)) = \int_{-\infty}^{+\infty} \rho_i(x) e^{-j(2\pi k_x x + \Phi(x,t))} dx \quad (4.1)$$

where  $\rho_i(x)$  presents the transverse magnetization density (modulated by RF pulse) at position  $x_i$ .  $\Phi(x, t)$  is the phase accumulated by the  $B_0$  inhomogeneity in both spatial and temporal domains. With well  $B_0$  shimming,  $\Phi(x, t)$  can be neglected between two closed slices with relatively thin thickness. Meanwhile, due to the limited thickness of the excited profile on the  $x$ -axis, most of MR signals are acquired from the position  $x_i$ . Hence, the equation about  $S_i(k_x)$  can be re-written as:

$$S_i(k_x(t)) = \rho_i(x) e^{-j(2\pi k_x x_i)} \quad (4.2)$$

With proper slice gradient refocusing, the phase offset of the acquired signal is defined by the position of excited profile only. At the central position  $x_i = 0$ , there is no phase offset in the acquired MR signal. Both  $S_i(k_x(t))$  and its Fourier transform  $\hat{\rho}(k_x)$  are real and even. Inversely, it is available to introduce phase offset by exciting profile deviating from the center of the axis.

If two slices at position  $x_1$  and  $x_2$  are excited in two individual pre-scans, there will be a phase gap between acquired MR signals from two slices. The effective  $k$ -space coordinate  $k_x(t)$  can then be figured out as:

$$k_x(t) = \frac{\varphi_2 - \varphi_1}{2\pi(x_1 - x_2)} \quad (4.3)$$

where  $\varphi_1$  and  $\varphi_2$  are the phases of the acquired complex signal at positions  $x_1$  and  $x_2$ . To obtain the actual sampling trajectory accurately, it is essential to unwrap the phase of acquired MR signals. However, the magnitude of acquired signal decreases significantly from low k-value to high k-value while signal nulling occurs. The signal nulling results in critical phase determination and phase unwrapping. Significant errors are observed in measured k-space trajectories at high k-value (68).

To overcome the measurement error caused by signal nulling, an additional dephasing gradient has been introduced into the same axis in the pre-scan as shown in Figure 4-8. The dephasing gradient is placed prior to the readout gradient to be calibrated. The MR signal at the position  $x_i$  is acquired three times with the dephasing gradients  $G$ ,  $0$  and  $-G$  respectively. The dephasing gradient shifts the position of peak magnitude of the acquired MR signal. Consequently, the signal nulling of the acquired signal occurs at different time points in these three pre-scans. The acquired signal  $S_i^G$  modified by a dephasing gradient is expressed as:

$$S_i^G(k_x(t)) = \hat{\rho}(k_x(t) + k_G)e^{-j(2\pi k_x x_i)}e^{-j(2\pi k_G x_i)} \quad (4.4)$$

Additional phase offset  $\varphi_G = e^{-j(2\pi k_G x_i)}$  is introduced by the dephasing gradient while the points with magnitude approaching zero are distributed at symmetrical  $k_x$  value. The dephasing gradient is designed as:

$$k_G = \frac{1}{\Delta s} \quad (4.5)$$

where  $\Delta s$  presents the thickness of excited profile in the pre-scan. The slice positions are designed as multiples of  $\Delta s$  while the effective phase offset introduced

by dephasing gradient  $\varphi_G = 1$ . The equivalent effect from dephasing gradient has been eliminated while the SNR of acquired signal at position  $x_i$  is improved effectively by averaging the  $S_i^{-G}$ ,  $S_i$  and  $S_i^G$ .

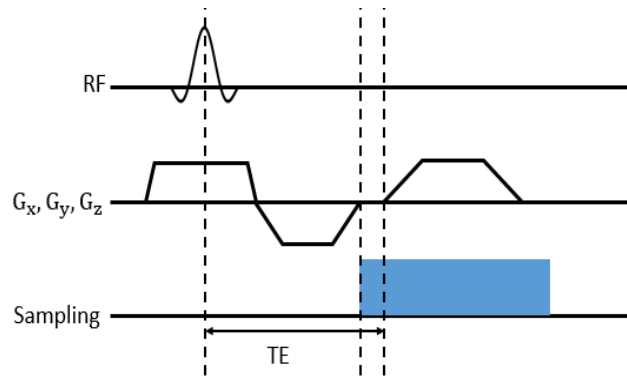


Figure 4-7: Pulse sequence for measuring the central out radial sampling trajectories. All the gradients are placed on the same axis while multiple slices are excited at different positions on this axis. Three orthogonal axes are measured by individual pre-scans respectively.

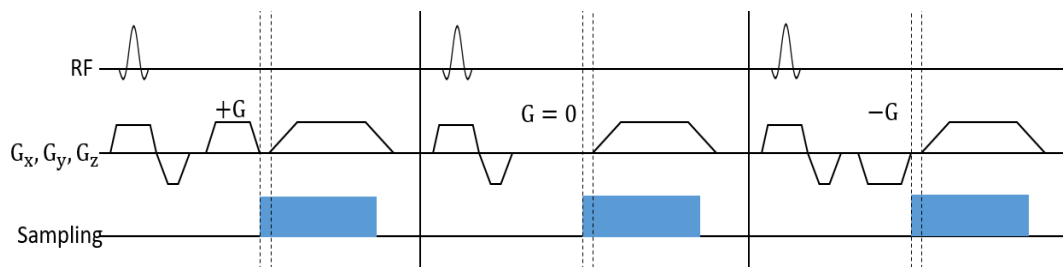


Figure 4-8: Advanced trajectory measurement pulse sequence diagram. An additional dephasing gradient  $G$  is introduced into the pre-scan to shift the position of signal nulling in the acquired MR signal. The SNR of acquired is improved by averaging pre-scans with dephasing gradient  $+G$ ,  $0$  and  $-G$  while the errors from signal nulling are compressed effectively.

## 4.5 Iterative Density Compensation Function

In non-Cartesian radial sampling, non-uniform sampling density is induced during data acquisition. The density of sample points in k-space center is much higher than the outer k-space. The DCF is designed to compress the blurring caused by excessive accumulation of low frequency components in k-space. The DCF can be simply obtained by a linear function or computing a Voronoi diagram (35,37). However, the central out radial sampling pattern in UTE induces an even higher sampling density in the k-space center compared with conventional radial sampling. The deviation of sampling trajectory caused by system imperfection demands an advanced DCF for gridding compensation. A relatively ideal DCF can be achieved by an iterative numerical method (69). The overall gridding equations in chapter 2.6 can be expressed as:

$$M_{scs}(k_x, k_y) = [(M \cdot S \cdot W) * C] \cdot R \quad (4.6)$$

where  $M_{scs}$  is the gridded data while  $k_x$  and  $k_y$  are k-space coordinates.  $M$  is the original MR signal and  $W$  represents the DCF.  $C$  and  $R$  are the convolution function and Cartesian grid respectively. The non-Cartesian sampling function  $S$  typically offers high sampling density and low sampling density in central k-space and outer k-space respectively. As mentioned in Equation 2.30,  $S$  consists of a series of Dirac functions. Without loss of generality,  $W$  can be defined to be nonzero only at the sampling locations  $(k_x, k_y)$  and thus  $W = S \cdot W$ . The Equation 4.6 is simplified as:

$$M_{scs}(k_x, k_y) = [(M \cdot W) * C] \cdot R \quad (4.7)$$

The Fourier equivalent to the Equation 4.7 in spatial domain is:

$$m_{scs}(x, y) = [(m * w) \cdot c] * r \quad (4.8)$$

An ideal DCF can compensate unbalanced sampling density in  $S$  so that weighting and convolution do not affect the image  $m$ . Hence,  $w$  is supposed to be a delta function at position  $(x, y)$  within the FOV while an accurate reconstruction can be achieved as:

$$(m * w) \cdot c = m \cdot c \quad (4.9)$$

Currently,  $w$  is zero in the spatial domain except at a certain position within the imaging FOV as:

$$\begin{aligned} w(x, y) &= 1, & x = y = 0 \\ w(x, y) &= 0, & x < \sqrt{x^2 + y^2} < d \end{aligned} \quad (4.10)$$

Consecutively, the combination of  $w$  and  $c$  is supposed to be a Dirac function to support the accurate reconstruction and minimize convolution effect as:

$$w \cdot c = \delta(x, y) \quad (4.11)$$

By convolving both sides of Equation 4.11 by  $w$ , a function  $w$  can be given as:

$$w * (w \cdot c) = w \quad (4.12)$$

In frequency domain, the Equation 4.12 is expressed as:

$$W \cdot (W * C) = W \quad (4.13)$$

Dividing both sides of Equation 4.13 by the  $(W * C)$ , a relatively ideal DCF can be obtained by a stable iteration as:

$$W_{i+1} = \frac{W_i}{(W_i * C)} \quad (4.14)$$

The denominator approaches unity when  $W_{i+1} = W_1$ . Hence, the sampling density is forced to be unity at the sampling coordinates with sufficient iterations. The initial iteration can be started with:

$$W_1 = \frac{S}{(S * C)} \quad (4.15)$$

## 4.6 Stack-of-Stars 3D UTE Imaging

### 4.6.1 3D Stack-of-Stars UTE Pulse Sequence Design

A stack-of-stars central out golden angle Fast Low Angle Shot (FLASH) pulse sequence with adaptive TE was designed for 3D UTE imaging as shown in Figure 4-6. A non-selective hard pulse with a 40 us period was employed to excite the 3D profile. A triangle-shaped phase encoding gradient  $G_{pz}$  was started immediately after RF excitation. The duration of  $G_{pz}$  was adapted from 120 us to 240 us, encoding the partitions from the central k-space to the edge of k-space along slice dimension respectively. Readout gradients on x-axis and y-axis were turned on at the end of  $G_{pz}$ . The degree between the spokes acquired in two adjacent TR periods was  $111.246^\circ$ , forming golden angle central out radial sampling. The effective TE in this pulse sequence was 140 us, corresponding to the sum of effective RF duration and minimum duration of  $G_{pz}$ .

A pre-acquisition step was employed to alleviate the damping effect of switching coil systems. Data acquisition was started with the ramping up of  $G_{pz}$ . Decades of pre-samples were acquired while these sample points were eliminated in ultimate reconstruction. All the pulse sequences were performed on a whole-body 1.5T MRI super-conduct scanner (XGY Medical Equipment Company, Yuyao, China). The gradient system equipped in the scanner achieves a maximum gradient strength of 30 mT/m and a slew rate of 150 T/m/s.

#### **4.6.2 Stack-of-Stars 3D UTE Brain Imaging**

3D brain UTE was performed on one healthy volunteer (male, age=28) on a whole-body 1.5T MRI super-conduct scanner (XGY Medical Equipment Company, Yuyao, China) equipped with the 8-element head matrix coil array. A 3D stack-of-stars central out golden angle FLASH pulse sequence was employed for brain imaging. Two scans were performed in transverse and sagittal orientations to image the head tissues with short  $T_2$  value like meninges and nose cartilage.

The corresponding imaging parameters included: TR/TE=5 ms/0.14 ms, FOV=260\*260\*240 mm<sup>3</sup>, FA=6°, number of points in each spokes=294 (consists of 24~48 pre-samples, 60 samples acquired during readout gradient ramping up), number of partitions=40 (interpolated into 60 in the reconstruction), and spatial resolution = 1.02\*1.02\*4.0 mm<sup>3</sup>. A total of 800 spokes were acquired for each partition while the total scan duration was around 2.5 mins.

In order to certificate the essential of short TE, an additional 3D stack-of-star golden angle FLASH pulse sequence was performed on transverse orientations for comparison. The relevant imaging parameters included: TR/TE=5 ms/2.47 ms,

FOV=260\*260\*240 mm<sup>3</sup>, FA=6°, number of points in each spokes=512 (central 256 points were used in reconstruction), number of partitions=40 (interpolated into 60 in the reconstruction), and spatial resolution = 1.02\*1.02\*4.0 mm<sup>3</sup>. A total of 400 spokes were acquired for each partition while the total scan duration was around 1.3 mins.

A 2D standard GRE pulse sequence with a long TE was performed on the transverse orientation for further comparison. The relevant imaging parameters included: TR/TE=500 ms/10 ms, FOV=260\*260 mm<sup>2</sup>, FA=70°, a k-space with matrix size 256\*256 was acquired, number of slices=30, spatial resolution = 1.02\*1.02\*4.0 mm<sup>3</sup> and total scan duration=106 s.

#### **4.6.3 Stack-of-Stars 3D UTE Knee Imaging**

3D UTE knee datasets were acquired in one healthy volunteer (male, age=28) and one patient with a metal implant in ankle section (male, age=42). Imaging was performed on a whole-body 1.5T MRI super-conduct scanner (XGY Medical Equipment Company, Yuyao, China) equipped with the 8-element knee matrix coil array, using a 3D stack-of-stars central out golden angle FLASH pulse sequence. Three scans were performed on two volunteers in transverse, coronal and sagittal orientations to image the cartilage. The relevant imaging parameters included: TR/TE=4.72 ms/0.26 ms, FOV=180\*180\*240 mm<sup>3</sup>, FA=6~30°, number of points in each spokes=294 (consists of 24~48 pre-samples, 60 samples acquired during readout gradient ramping up), number of partitions=40 (interpolated into 60 in the reconstruction), and spatial resolution = 1.0\*1.0\*4.0 mm<sup>3</sup>. A total of 800 spokes were acquired for each partition while the total scan duration was around 2.5 mins.

An additional 2D GRE pulse sequence with a long TE was performed on the patient with a metal implant in transverse orientation for comparison. The relevant imaging parameters included: TR/TE=290 ms/7.6 ms, FOV=220\*220 mm<sup>2</sup>, FA=50°, a k-space with matrix size 256\*256 was acquired, number of slices=18, spatial resolution = 0.86\*0.86\*3.0 mm<sup>3</sup> and total scan duration was around 2.3 mins.

#### **4.6.4 Pre-scan for Trajectory Calibration**

Pre-scans were performed on x-axis, y-axis and z-axis to measure the equivalent sampling trajectory on three orthogonal axes respectively. All pre-scans were performed on a whole-body 1.5T MRI super-conduct scanner (XGY Medical Equipment Company, Yuyao, China) equipped with the 8-element head matrix coil array, using a modified 1D central out golden angle radial FLASH pulse sequence. A 14000 us sinc RF pulse with 6 sidelobes was implemented to excite a 3 mm slice with a relatively flat profile. Two profiles were excited at the positions +6mm and -6 mm respectively. Additional dephasing gradient  $G$  was designed to satisfy  $k_G = 0.33/mm$  to induce adequate phase offset between the acquisitions with dephasing gradient  $+G$ , 0 and  $-G$  in pre-scans. A sphere phantom with the solution doped with CuSO<sub>4</sub> at a concentration of 1.955mol/L and NaCl at a concentration of 3.6mol/L was implemented as the imaging object. The  $T_1$  and  $T_2$  of the phantom were measured as 160 ms and 130 ms respectively.

The pre-scan pulse sequence parameters included: TR/TE=500 ms/10 ms, FA=90°, a total of 1600 spokes and 1036 sample points in each. The design of long TR ensures sufficient recovery of longitudinal magnetization signal of SNR phantom. The first 100 samples in the spokes were pre-samples to avoid damping during the

switching of coil system. 60 samples were acquired during readout gradient ramping up which is kept the same as acquisition model in UTE imaging. Other 876 samples were acquired on the constant window of readout gradients.

## 4.7 Image Reconstruction and Analysis

In order to evaluate the performance of trajectory calibration and iterative DCF, the acquired 3D hybrid UTE datasets were reconstructed by NUFFT with theoretical trajectory, calibrated trajectory, simple DCF and iterative DCF respectively. The optimized DCF was obtained by 10 iterations. Figure 4-9 has shown a comparison of theoretical trajectory and measured trajectory. With proper eddy current compensation, there is no significant deviation between measured trajectories and theoretical trajectories. However, for the samples acquired in central k-space, the gradient distortion during gradient ramping up resulted in the fluctuation of sampling trajectories. The obvious difference between theoretical trajectories and measured trajectories was obtained in central k-space.

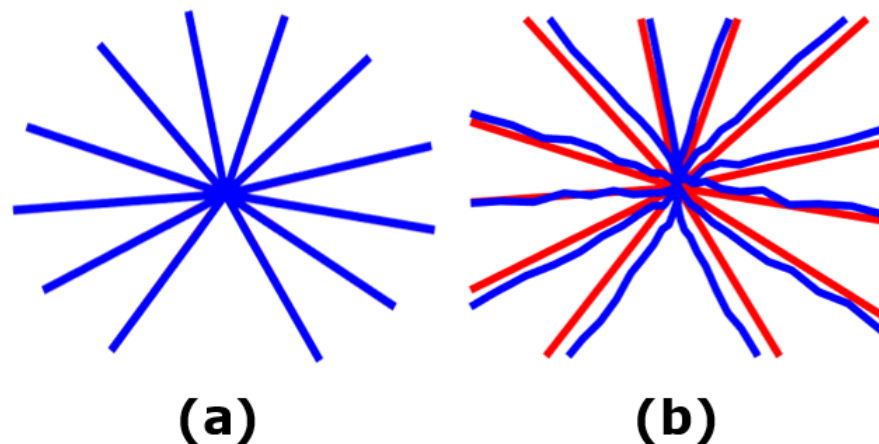


Figure 4-9: (a) A comparison of theoretical sampling trajectories (red lines) and measured sampling trajectories (blue lines). (b) A zoomed view of theoretical sampling trajectories and measured sampling in k-space center.

Figure 4-10 shows a slice of brain image reconstructed with different gridding parameters. Significant blurring was obtained in the image reconstructed with simple DCF. Simple DCF is insufficient to compress the accumulation of signal intensity in k-space center during gridding reconstruction. Iterative DCF gridding achieved an effective intensity compression for low frequency components. Some distortion and blurring artefacts were obtained in the image reconstructed with iterative DCF and theoretical trajectories. The blurring artefacts and distortion were removed while a better contrast of brain tissues was achieved in the calibrated image. Figure 4-11 shows a comparison of UTE imaging and conventional VIBE imaging at a certain slice of brain. The MR signals from both receiving coils and brain were excited simultaneously while the coil signals decayed rapidly due to the extremely short  $T_2$  value. In UTE images, the signals from head coil elements were captured and imaged successfully. These coil elements were invisible in the VIBE image. Figure 4-12 shows a comparison of the proposed UTE and standard GRE in three different slices of brain. In the slice of the nose, the nose cartilage and the eye optic nerve, which have short  $T_2$  values, have been displayed with prior quality in the UTE image. Hypointensity of nose cartilage and the eye optic nerve was obtained in GRE images due to the excessive decay. Some internal structures of these two tissues became invisible in GRE images. This signal intensity enhancement from UTE is extremely helpful in the clinical diagnosis of fractured nose cartilage or abnormal eye optic nerve (56). The third column of brain images demonstrate an enhancement in the signals of short  $T_2$  teeth in mouth slice. The weak signal of teeth was obtained in UTE images. The teeth were completely invisible in GRE images.

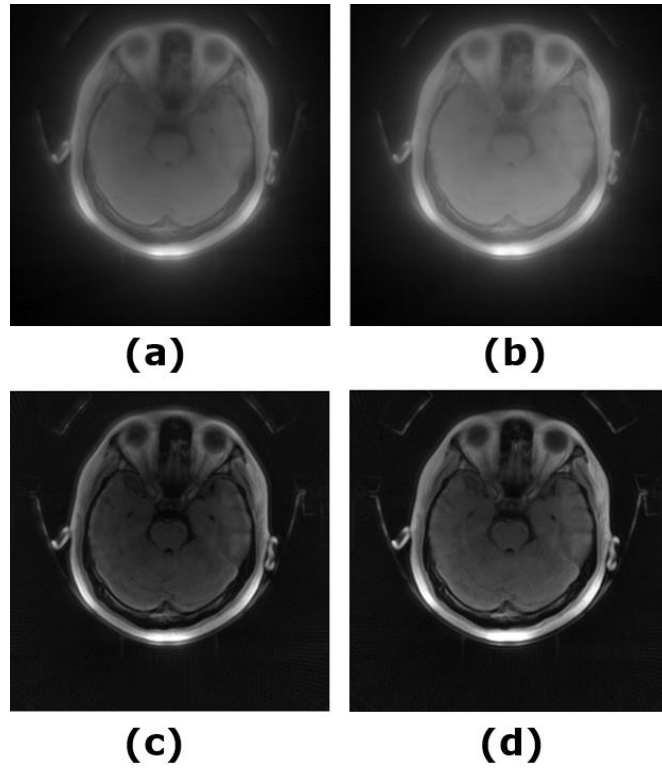


Figure 4-10: (a) Reconstruction with theoretical trajectories and simple DCF. (b) Reconstruction with measured trajectories and simple DCF. (c) Reconstruction with theoretical trajectories and iterative DCF. (d) Reconstruction with measured trajectories and iterative DCF.

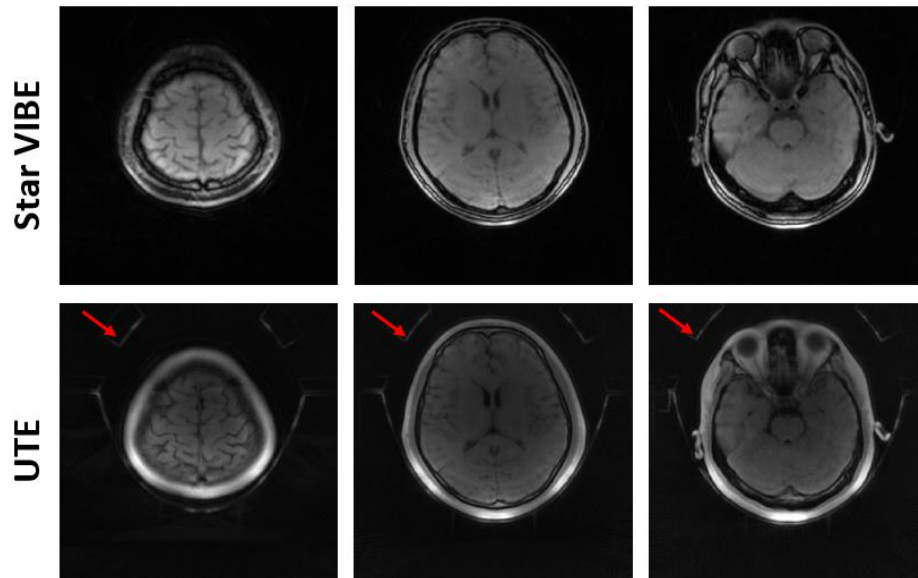


Figure 4-11: A comparison of brain images acquired using advanced 3D stack-of-stars UTE imaging and stack-of-stars VIBE imaging. The short  $T_2$  coil signals were captured in UTE images labelled by red indicators.

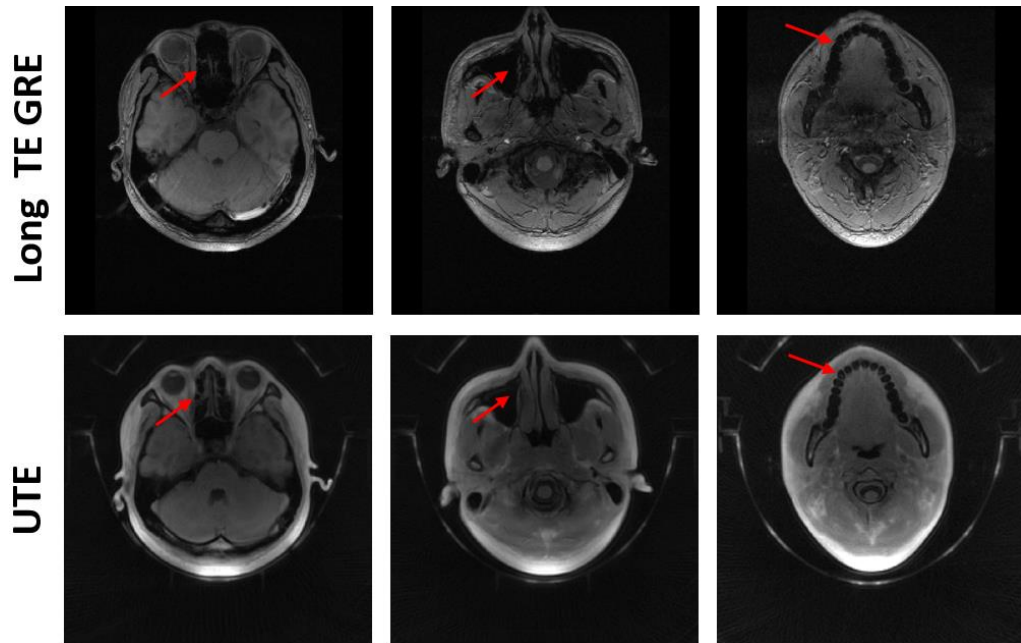


Figure 4-12: A comparison of brain images acquired using advanced 3D stack-of stars UTE pulse sequence with parameters: TR/TE=5.0/0.14ms, FA=6°, FOV=260mm \* 260mm \* 250mm, matrix size 256 \* 256 \* 64 and 2D GRE pulse sequence with parameters TR/TE=500ms/10ms, FOV=260\*260mm, FA=70°, matrix size 256 \* 256, number of slices=30. The intensity enhancements of nose cartilage, the eye optic nerve and teeth were observed in UTE images

Figures 4-13 shows a representative slice of UTE knee image of a healthy volunteer in sagittal orientation. The zoomed view of knee joint has displayed the cartilage in detail which is helpful in clinical diagnosis and treatment monitoring of the degradation of cartilage due to the daily wear and tear of joints.

Figures 4-14 shows a comparison of the proposed UTE imaging with different FA in a representative slice of knee with a metal implant. The metal implant is strong paramagnetism and it induces an inhomogeneous local magnetic field. Significant signal decay and geometry distortion are observed in the metal implant regions in conventional MRI (70-72). In Figure 4-14, there were limited signal dephasing and artefacts in UTE images. The ultra-short TE minimized the additional dephasing

caused by the metal implant. Abnormal muscle tissues (labelled by a red cycle) were invisible in GRE images while they were displayed clearly in UTE images.

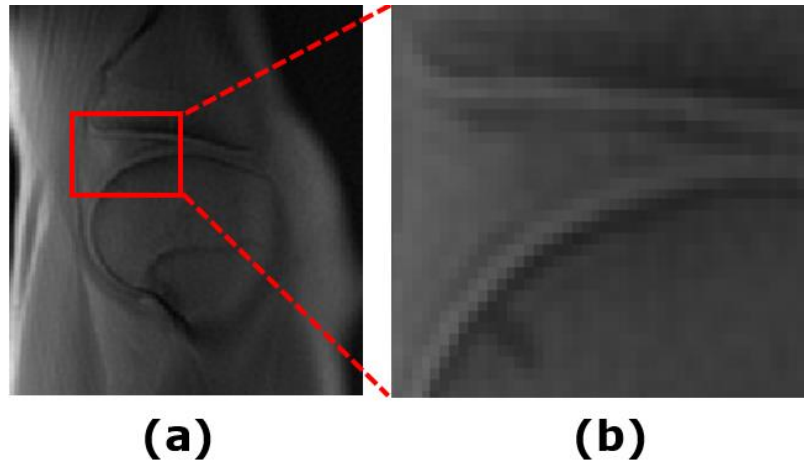


Figure 4-13 (a) A slice of knee image acquired by advanced 3D stack-of stars UTE pulse sequence with parameters: TR/TE=5.0/0.14ms, FA=6°, FOV=180mm \* 180mm \* 240m, matrix size 256 \* 256 \* 80. (b) A zoomed view of knee joint, the internal structure of cartilage can be obtained in detail.



Figure 4-14: A representative slice of knee with metal implant acquired using advanced 3D stack-of stars UTE pulse sequence with parameters: TR/TE=5.0/0.26ms, FA=6°, 12° and 30° (from left to right), FOV=180mm \* 180mm \* 240m, matrix size 256 \* 256 \* 80. The metal implant sections and abnormal muscle regions were labelled by red arrows and a red cycle respectively.

## 4.8 Discussion

It is essential to develop an advanced 3D UTE pulse sequence to image the tissues with extremely small  $T_2$ . The TE can be reduced effectively by removing the pre-dephasing gradient in radial sampling, forming the central out radial sampling pattern. Both conventional 2D UTE imaging and 3D UTE imaging are developed from the central out radial sampling pattern. However, the implementation of half pulse excitation directly increases the data acquisition period and sensitivity to the hardware imperfections in 2D UTE. 3D UTE contains a relatively simple pulse sequence diagram while the images can be reconstructed with an isotropic resolution. But the long data acquisition and computational costly 3D gridding reconstruction strictly limits its clinical application.

An advanced 3D UTE imaging protocol is developed on a stack-of-stars central out golden angle pattern. It offers fast data acquisition and reconstruction in 3D UTE imaging. With the design of adaptive phase encoding on the partition dimension, the minimum TE in this advanced UTE sequence is comparable with the conventional 3D UTE sequence.

To tackle with the hardware imperfections, we implemented pre-scans to measure the sampling trajectory rather than calibrate the eddy current. The advanced trajectory measurement pulse sequence obtains the actual sampling trajectory accurately. The image artefacts and distortions caused by sampling deviation were compressed effectively by the calibrated trajectory. The imaging quality was further improved by an iterative DCF, which minimizes the PSF interference from the DCF.

Compared with conventional long TE images, the UTE images have demonstrated a significant enhancement of signal in short  $T_2$  tissues including nose cartilage, eye optic nerve, teeth and knee cartilage, etc. Even the signals from the receiving coil elements were captured in UTE images, showing the robustness of advanced 3D stack-of-stars UTE imaging. Meanwhile, UTE also shows the merits of imaging tissues near the metal implants. The geometry distortion and signal dephasing caused by  $B_0$  inhomogeneity is minimized by the ultra-short TE.

The drawback of the proposed UTE sequence is the same as other UTE techniques. Central out radial sampling pattern degrades the acquisition efficiency by half. The number of spokes in central out radial sampling is around 3 times larger than the phase encoding steps in Cartesian sampling (48). The problem of excessive data acquisition period can be alleviated by introducing acceleration techniques like compressed sensing into the reconstruction. The combination of golden angle radial sampling and compressed sensing enables a relatively high AF with less distortion.

## **4.9 Conclusion**

An advanced 3D UTE imaging protocol is developed from a stack-of-stars central out golden angle sampling pattern. Trajectory measurement and iterative DCF were combined as a robust calibration framework to improve the image quality. Several clinical experiments have certificated the robustness of the proposed UTE imaging protocol in alleviating MR signal decay. A significant signal enhancement was obtained in the short  $T_2$  tissues in UTE images.

## Chapter 5 Motion Resolved UTE Lung

### Imaging with Oxygen Enhancement

Lung imaging is still a challenging topic for MRI. The low proton density in lung tissues leads to low MR signal while the rapid  $T_2^*$  decay of lung tissues (typically  $<500\mu\text{s}$  at high field strength) causes further degradation of the MR signal (73,74). The periodical rigid motions including respiratory and cardiac motion result in significant motion artefacts which further limit the application of MRI for lung parenchyma imaging.

In recent years, UTE techniques are increasingly popular for imaging the lung tissues with short  $T_2^*$  relaxation time. A variety of studies have certificated the priority of UTE for direct lung parenchyma visualization (11,12,55,73). The radial based UTE achieves oversampling in central k-space which offers intrinsic motion robustness (75). The artefacts caused by rigid motion perform as the blurring in radial images (76).

Here, we implemented the advanced stack-of-stars UTE pulse sequence directly for free-breathing UTE lung imaging. A motion signal was extracted from a self-gated stack-of-stars sampling pattern. Acquired spokes were subdivided into multiple motion states according to the extracted motion signal. Multiple motion states were reconstructed simultaneously to investigate the variation of lung tissues during the respiratory and alleviate the motion blurring.

To further improve the contrast of tissues, the oxygen-enhanced technique is combined with UTE imaging for investigating the function of the lung including ventilation and perfusion. The improvement of MR signal caused by oxygen enhancement enables a more accurate clinical diagnosis in lung tissues.

## 5.1 Motion Estimation and Subdivision

The proposed UTE sampling scheme in chapter 4 employs central out golden angle radial sampling in transverse  $k_x - k_y$  plane and Cartesian sampling along the partition  $k_z$  dimension respectively. The sampling scheme acquires all the spokes along  $k_z$  at a given rotation angle in prior to acquisitions in  $k_x - k_y$  plane, forming the inner loop. The inner loop acquisition is continuously repeated for different rotation angles as shown in Figure 5-1.

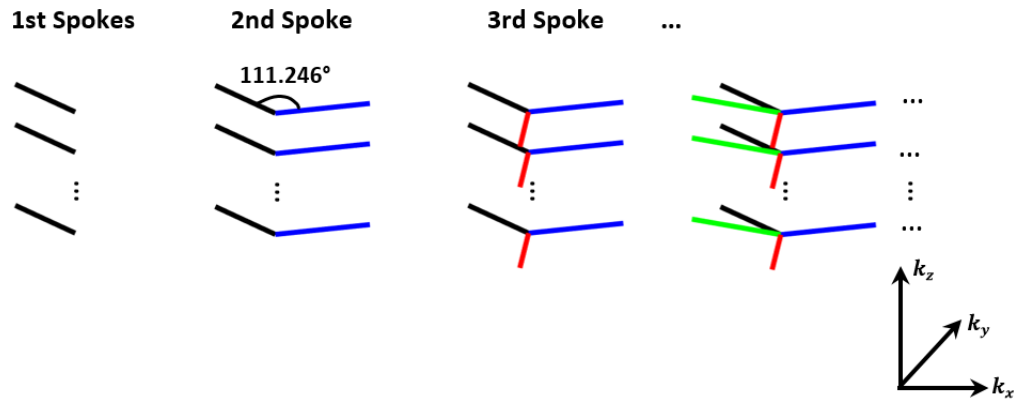


Figure 5-1. Stack-of-stars central out golden angle sampling trajectories, the partition dimension and transverse plane are encoded as inner-loop and outer-loop respectively.

It is obvious that the k-space center along the  $k_z$  dimension is repeatedly acquired during the data acquisition. A projection profile of the entire imaging volume is easily observed by applying 1D partition-direction FFT on the central k-space data

along the slice dimension where  $k_x, k_y = 0$ . During the data acquisition, the projection profile will experience slight fluctuation which is caused by periodic motion. Inversely, it is available to extract the motion signal based on analyzing the shift of the projection profile through coil clustering and principle component analysis (PCA) (77,78).

The projection profiles from all coil elements are concatenated into a large 2D matrix while PCA algorithm is implemented along the concatenated coil dimension to detect the respiratory motion. PCA can determine the most significant signal variation model among the coil channels. The peak principle component in the frequency range from 0.1 Hz to 0.5 Hz which represents the typical respiratory frequency is selected as the respiratory motion signal.

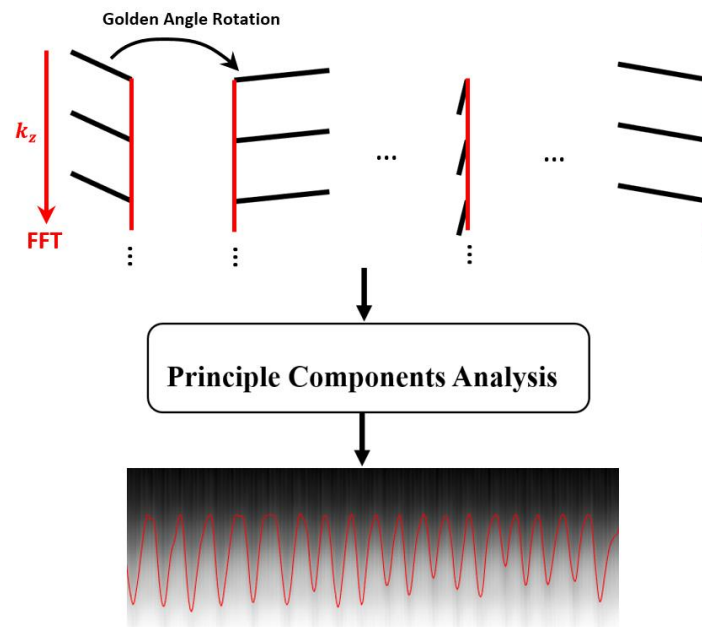


Figure 5-2: Procedures to estimate the motion signals from stack-of-stars sampling schemes. The repeated acquired k-space center is converted into the projection of the excited profiles on the partition dimension. The PCA algorithm is implemented to analyze the variation of these projection curves to estimate the rigid motion signal.

With the support of PCA algorithm, the respiratory phase of each acquired spokes was obtained. Hence, the acquired spokes in the stack-of-stars UTE scheme can be resorted and subdivided into multiple motion states according to the estimated respiratory signal as shown in Figure 5-2. Due to the intrinsic property of golden angle radial sampling, approximately uniform coverage of k-space with distinct sampling patterns in each motion state is achieved in the stack-of-stars UTE scheme (10,29). Reconstruction with the spokes which are acquired at similar respiratory phases directly compresses the respiratory blurring.

The motion resolved UTE lung imaging is achieved by subdividing and reconstructing multiple respiratory states simultaneously at the expense of introducing undersampling streaking artefacts. The AF is directly proportional to the motion state resolution. Sufficient data acquisition is required to support additional motion subdivision and enable fewer streaking artefacts in reconstructed image series.

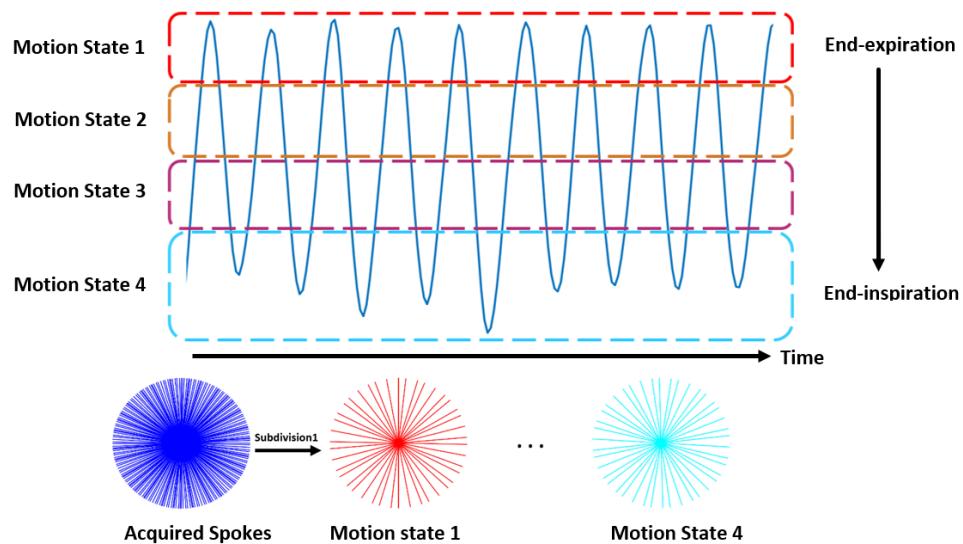


Figure 5-3: Motion subdivision for the continuously acquired spokes. The spokes are initially resorted according to the estimated respiratory signals and then subdivided into 4 motion states here.

## 5.2 Oxygen-Enhanced UTE Lung Imaging

Enhancing the signal intensity in lung tissues is an increasingly popular research topic in recent years. By implementing appropriate external gaseous contrast media, the signal intensity of lung can be improved significantly, enabling functional lung imaging. MRI with hyperpolarized noble gas like Xe<sup>129</sup> (79,80) and He<sup>3</sup> (81,82) offers a non-invasive, ionizing-radiation-free method to image pulmonary structure and function with priority signal intensity. However, the excessive cost of hyperpolarized noble gas limits their clinical applications. Compared with hyperpolarized noble gas MRI, oxygen-enhanced MRI is a cost-effective approach for investigating lung function (83).

The signal improvement in oxygen-enhanced MRI is achieved by the reduction of  $T_1$  value in lung tissues. The molecular oxygen can reduce the  $T_1$  value reported firstly by Young et.al (84) and visually illustrated on excised rat lungs by Goodrich et al in 1991 (85).

Oxygen has the paramagnetic property and plays a role as the paramagnetic contrast agent in oxygen-enhanced MRI. The majority of oxygen molecules dissolve in blood while these paramagnetic molecules increase the inhomogeneity of local magnetic field. Consequently, molecular motion is enhanced while the energy exchange efficiency between proton paramagnetic molecules is improved, shortening the  $T_1$  relaxation time (84,85). With the same imaging protocols like Half Fourier-acquired single-shot turbo spin-echo (HASTE), the signal intensity of lung is improved due to the reduction of  $T_1$  value. A relative enhancement ratio

(RER) map or percent signal enhancement (PSE) map (86) can be obtained to describe the pointwise intensity variation caused by oxygen enhancement as:

$$\text{PSE} = \frac{S_{O_2} - S_{air}}{S_{air}} \cdot 100\% \quad (5.1)$$

where  $S_{O_2}$  and  $S_{air}$  represent the signal intensity before and after oxygen enhancement respectively. The signal intensity in lung tissues is typically increased from 10% to 50%, depending on the imaging pulse sequence and corresponding parameter assignments (87-90). The PSE map offers additional ventilation and perfusion information for improved clinical diagnosis. A variety of studies has certificated that the ratio of  $T_1$  reduction and signal enhancement is directly proportional to the partial pressure of oxygen (91-93).

Since UTE sequence is increasingly popular in lung imaging, some investigators also tried to measure  $T_1$  by UTE sequence, which can provide high-resolution images and allow free-breathing during the experiment (94,95). A variety of researches show the robustness of UTE for oxygen-enhanced lung imaging (96,97). In this work, we implemented a 5 minutes pure oxygen inhalation to reduce  $T_1$  and increase the volume of blood of lung tissues effectively, enabling the advanced signal enhancement. The 3D UTE imaging protocol in chapter 4 is implemented to acquire the data before and after oxygen enhancement, enabling free-breathing UTE lung imaging with improved SNR and advanced tissue details. Motion subdivision is further implemented on oxygen-enhanced datasets, compressing the motion blurring. The PSE map among different respiratory phases is investigated which offers additional ventilation information from lung tissues.

## **5.3 Free-Breathing UTE Lung Imaging Applications**

### **5.3.1 3D Free-Breathing UTE Lung Imaging**

3D UTE Lung datasets were acquired in three healthy volunteers (1 female and 2 males, mean age =  $26.2 \pm 2.7$  years). MRI Imaging was performed on a whole-body 1.5T MRI super-conduct scanner (XGY Medical Equipment Company, Yuyao, China) equipped with the 8-element body matrix coil array, using a stack-of-stars central out golden angle FLASH pulse sequence. All the scans were performed in coronal orientations to image the lung tissues with a short  $T_2$  value. The relevant imaging parameters included: TR/TE=5 ms/0.14 ms, FOV=496 \* 496 \* 240 mm<sup>3</sup>, FA=3~12°, number of points in each spokes=294 (consists of 24~48 pre-samples, 60 samples acquired during readout gradient ramping up), number of partitions=40 and spatial resolution = 1.94 \* 1.94 \* 4.0 mm<sup>3</sup>. A total of 1600~3200 spokes were acquired for each partition while the total scan duration ranged from 5 mins to 10 mins.

The acquired spokes were resorted according to the extracted respiratory signal. 4 respiratory motion states from end-inspiration to end-expiration (400~800 spokes in each state) were produced by subdividing the continuously acquired spokes as described in chapter 5.1. All the states images were reconstructed and compared with the lung image before motion resolving.

### **5.3.2 UTE Lung Imaging with Oxygen Enhancement**

3D oxygen-enhanced UTE lung datasets were acquired in three healthy volunteers (1 female and 2 males, mean age =  $26.2 \pm 2.7$  years). Imaging was performed on a whole-body 1.5T MRI super-conduct scanner (XGY Medical Equipment Company,

Yuyao, China) equipped with the 8-element body matrix coil array, using a stack-of-stars central out golden angle FLASH pulse sequence. The relevant imaging parameters included: TR/TE=5 ms/0.14 ms, FOV=450 \* 450 \* 240 mm<sup>3</sup>, FA=3~12°, number of points in each spokes=294 (consists of 24~48 pre-samples, 60 samples acquired during readout gradient ramping up), number of partitions=40 and spatial resolution = 1.76 \* 1.76 \* 4.0 mm<sup>3</sup>. A total of 1600 spokes were acquired for each partition while the total scan duration was around 5 mins.

Two datasets including the air dataset and the oxygen-enhanced dataset were acquired for all the volunteers with a free-breathing model. The air dataset was acquired by a 3D UTE scan without oxygen inhalation. After finishing the acquisition for the air dataset, volunteers wore a non-rebreathing face mask immediately and started to ventilate with the pure oxygen at a flow rate of 15L/min. After 5 minutes wash-in time, another 3D UTE scan was performed to acquire the oxygen-enhanced dataset.

The acquired spokes in both the air dataset and the oxygen-enhanced dataset were resorted according to the extracted respiratory signal. 4 respiratory motion states from end-inspiration to end-expiration (400 spokes in each state) were produced by subdividing the continuously acquired spokes. A PSE map was calculated for respiratory motion averaged lung images and motion resolved lung images. Before PSE calculation, the high-resolution images were low-pass filtered to low resolution to improve signal-to-noise (SNR). The hyperoxic images were registered to normoxia images using non-rigid registration algorithms (98,99). The variation of PSE maps from inspiration to expiration was investigated and analyzed.

## 5.4 Image Statistical & Analysis

The calibration framework in chapter 4 is implemented in the UTE lung imaging. Figure 5-4 shows the UTE lung imaging results in six representative partitions. Clear tissue details of lung and high SNR were achieved by the proposed UTE scheme. Both cardiac motion and respiratory motion were compressed by the radial sampling pattern while there was no ghost-like motion artefact in UTE lung images.

Figure 5-5 shows a further zoomed view of upper-left section of lung tissues in three representative partitions. The structure of blood vessels and bronchus in lung were obtained in UTE imaging. The sharpness of blood vessels and bronchus was degraded due to the respiratory motion blurring.

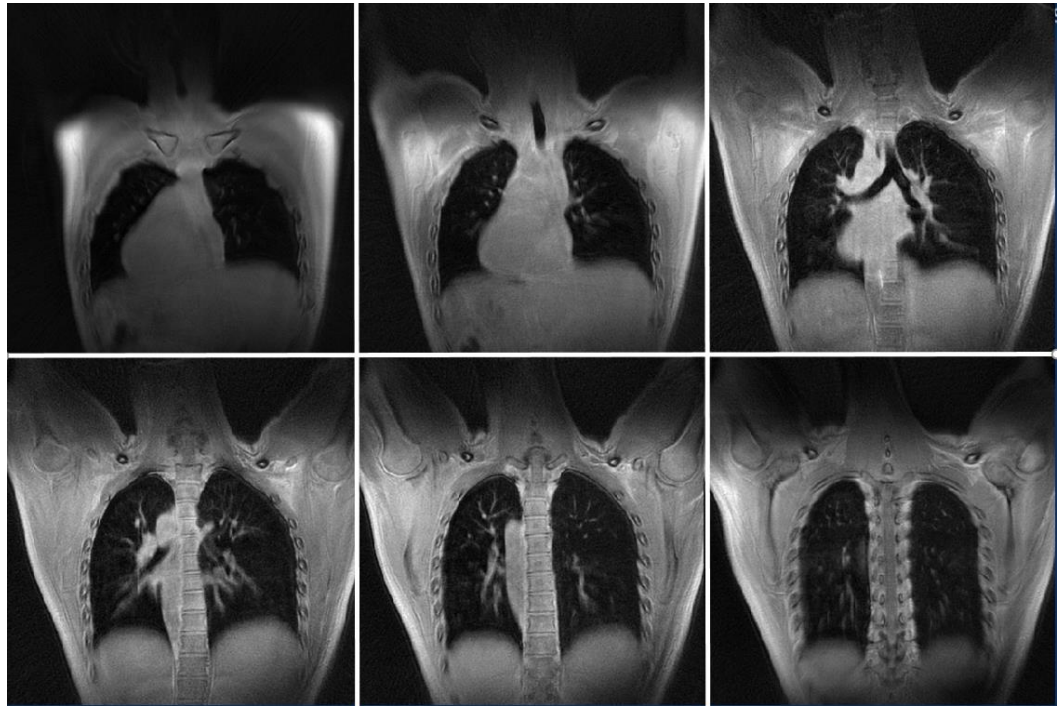


Figure 5-4: Six representative slices of UTE lung images. High SNR in lung tissues was achieved by the proposed 3D UTE imaging protocol.

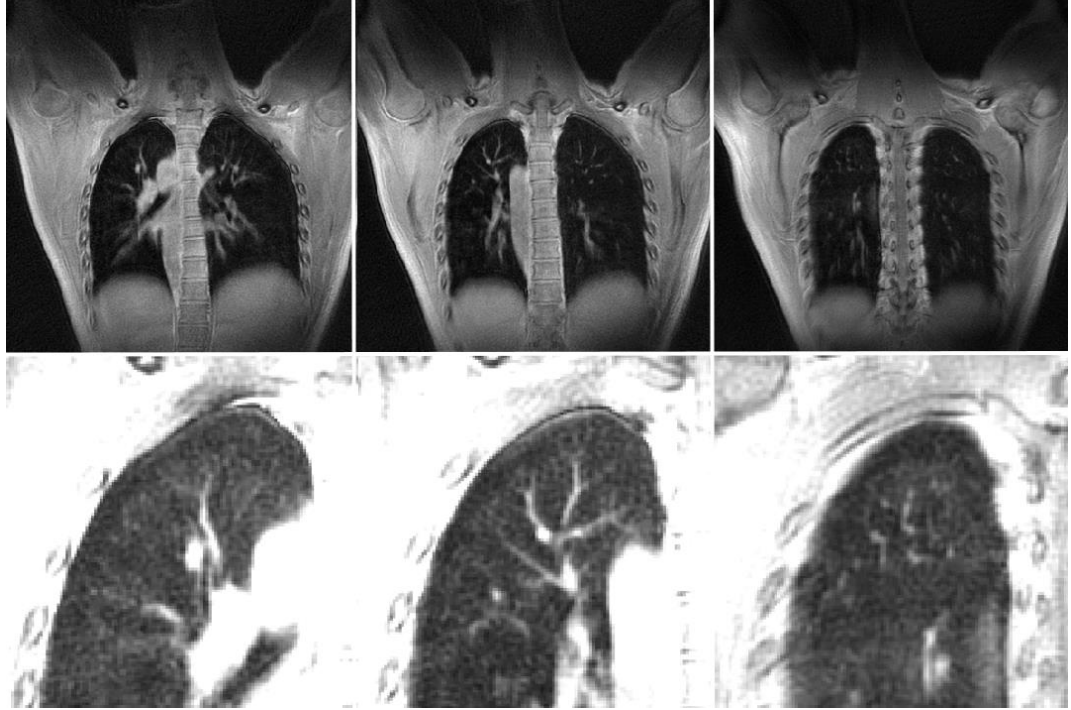


Figure 5-5: A zoomed view of lung tissues in three representative slices in 3D UTE imaging. The internal structure of lung tissues was clearly displayed in UTE images.

Figure 5-6 shows a comparison of UTE imaging before motion subdivision and UTE imaging after motion subdivision in one representative partition. Due to the reduction of spokes, the SNR was decreased in two motion resolved images compared with the motion averaged image. It is obvious that significant motion blurring was obtained in diaphragm section in averaged respiratory phase. The sharpness of the internal structure in lung was also degraded by the respiratory motion blurring. These motion blurring artefacts were effectively removed in motion resolved images. The blood vessels and bronchus with advanced tissue details and sharpness were obtained in both inspiration phase image and expiration phase image. The position of diaphragm edge in inspiration phase image and

expiration phase image corresponds to the range of diaphragm blurring in averaged respiratory phase image, showing the accuracy of motion subdivision. The respiratory resulted in a significant position shift of diaphragm and other tissues among different motion phases.

Figure 5-7 shows a comparison of three groups of oxygen-enhanced UTE lung images acquired with different FAs at end-expiration phase. The oxygen enhancement effect was observed in all the datasets. The mean percent signal enhancement (MPSE) was 3.33%, 4.89% and 8.88% for the dataset set acquired at FA =3°, 6° and 12° respectively. With the increase of FA, the  $T_1$  weighting was improved in FLASH-based UTE imaging. 12° was selected as the optimized FA which traded off oxygen enhancement ratio and SNR in the proposed 3D UTE schemes.

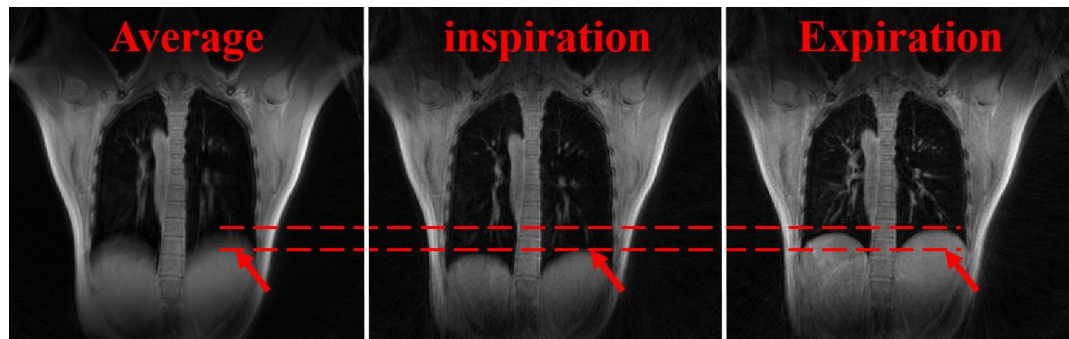


Figure 5-6 A comparison of UTE lung images in different motion phases. The lung images without motion subdivision expressed significant motion blurring. The motion blurring was compressed effectively in two motion resolved lung images. The respiratory motion leads to a significant position shift of diaphragm and other lung tissues between inspiration phase and expiration phase.

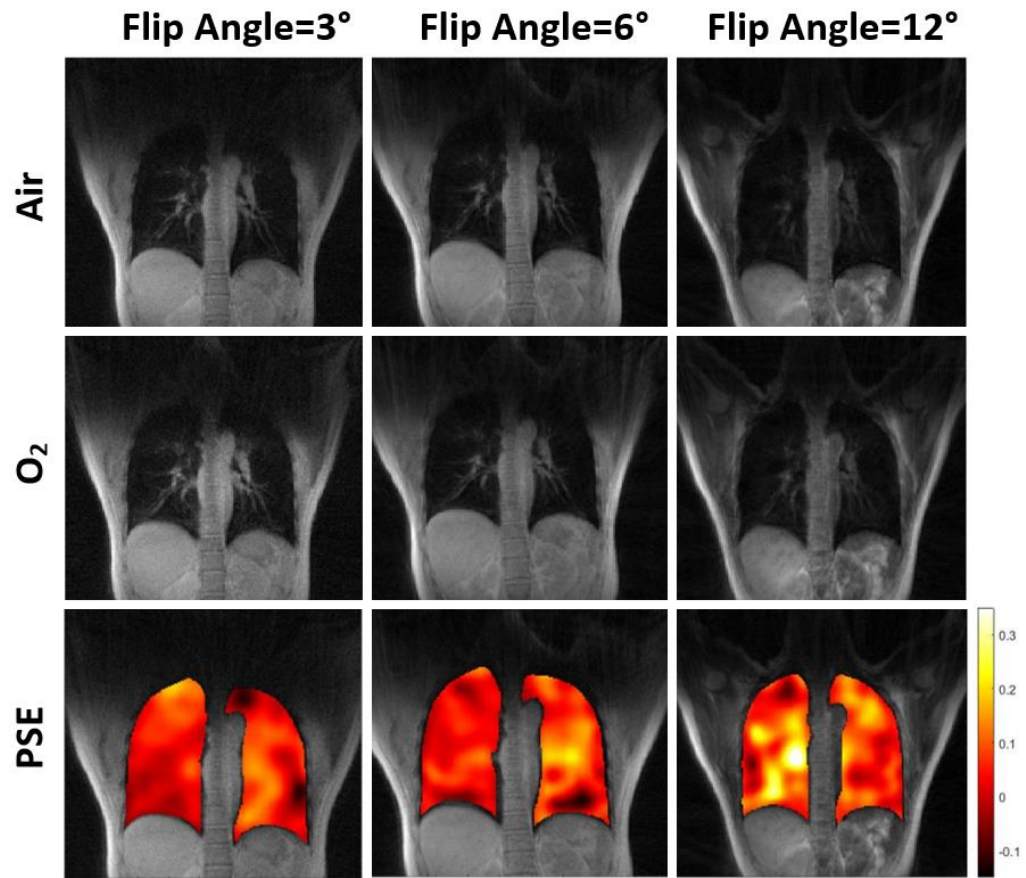


Figure 5-7 3D stack-of-stars central out golden angle UTE lung images and corresponding PSE maps at the end of expiration with variable flip angles from 3° to 12°. The corresponding mean of PSE is 3.33%, 4.89% and 8.88%.

Figure 5-8 shows the hyperoxic and normoxic UTE images and PSE maps of averaged respiratory phase and 4 subdivided respiratory phases from expiration to inspiration at the flip angle of 12°. Improved tissue details and less motion blurring were observed in all the motion resolved images. The MPSE without phase segmentation was 9.63%, matching the results in Figure 5-7. The MPSE of 4 respiratory phases from expiration to inspiration were 8.88%, 9.17%, 8.28%, 6.15%. A decline tendency of oxygen concentration was obtained from expiration to inspiration.

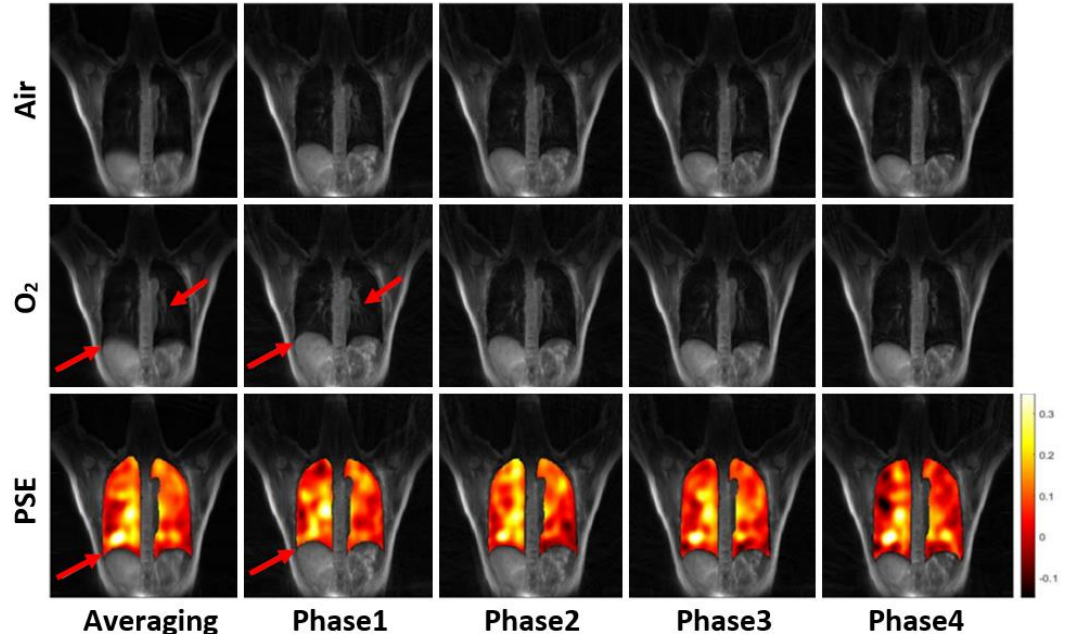


Figure 5-8: 3D stack-of-stars central out golden angle UTE  $T_1$  weighed lung images and its corresponding PSE map. The first column on left is reconstructed from all spokes without phase segmentation. The other 4 columns correspond to 4 respiratory phases from inspiration to expiration.

## 5.5 Discussion

Stack-of-stars central out golden angle UTE scheme enables the free-breathing lung imaging with high SNR and better tissue details. The MR signals in lung tissues with short  $T_2$  values were successfully captured and imaged in the proposed UTE scheme. Two periodic rigid motions in lung sections were compressed by the intrinsic averaging effect of radial sampling pattern while these two motions resulted in blurring in the proposed scheme (75). The cardiac motion blurring mainly happens on the heart section while this section is not the object of UTE lung imaging and thus can be ignored. The respiratory motion results in significant

motion blurring in diaphragm section. The sharpness of internal structure of lung tissues like blood vessels and bronchus is also degraded by the respiratory blurring.

By using the self-gating property of the stack-of-stars sampling pattern, extra motion states were subdivided according to the extracted motion signals. Golden angle radial sampling scheme enables a relatively uniform coverage of k-space in all of the subdivided respiratory motion states. By reconstructing the motion states with the spokes acquired at similar respiratory phases, the motion blurring was effectively compressed. Advanced tissues structure was obtained in the subdivided phase images, enabling accurate diagnose of lung diseases like pulmonary nodules, cystic fibrosis and chronic obstructive pulmonary disease (COPD) (11,12,55). It is also practical to explore the variation of lung tissues caused by respiratory by reconstructing the sufficient motion states images.

Motion subdivision also plays a significant role in oxygen-enhanced UTE lung imaging. Oxygen-enhanced MRI acquires air dataset and oxygen dataset in two individual scans. The calculated PSE map can be regarded as a standard for evaluating the lung functions like ventilation and perfusion. However, the respiratory motion leads to calculation errors in the PSE map. Significant calculation errors were obtained in the sections with significant motion blurring in PSE maps. Hence, all of the images are required to be registered before calculating the enhancement of signal intensity in lung tissues. Self-gating and motion subdivision does not require any motion models in registration. Hence, the interpolation errors in previously proposed registration techniques can be effectively reduced by the motion subdivision.

Implementing the motion subdivision before the registration can minimize the matching errors between air UTE images and oxygen-enhanced UTE images. Meanwhile, reconstructing multiple respiratory motion states may also be helpful to clinical diagnosis of lung diseases. The variation of oxygen concentration from inspiration to expiration can be resolved by investigating the PSE maps among different respiratory phases, offering additional respiratory function information.

The limitation of the motion resolved UTE imaging is the long acquisition time. The data acquisition efficiency is significantly degraded by the central out radial sampling pattern compared with other sampling patterns while sufficient spokes are required to support motion subdivision without undersampling artefacts. One solution is to use the acceleration techniques like compressed sensing to achieve high acceleration reconstruction by exploring the sparsity on the motion dimension. Meanwhile, self-gating approach is not limited to the central out golden-angle radial sampling. The golden angle stack-of-spiral pattern (12,55,56) is also an option which achieves ultra-short TE, high efficient data acquisition, motion estimation and motion subdivision simultaneously.

## **5.6 Conclusion**

The motion resolved UTE method achieves compressed motion blurring, improved tissues details and high SNR for imaging lung tissues with short  $T_2$  values. The reconstruction of additional motion states offers additional complementary information for clinical diagnosis. Combing motion-resolved UTE with oxygen-enhanced MRI provides a further improvement in signal intensity and abundant ventilation information of the lung.

## Chapter 6 Improved DCE-MRI Imaging

DCE-MRI possesses an unparalleled capacity for detecting and characterizing tumors and other lesions (100-103). Typically, multiple 3D images need to be rapidly acquired in different contrast-enhancement phases for monitoring the fast signal-intensity changes during the contrast agent period (104). The demand for rapid imaging speed with high spatial and temporal resolutions is challenging for MRI hardware system and limits its clinical applications. The general parallel imaging based acceleration techniques including SENSE (17) and GRAPPA (18) employ spatial information of multiple receiver coils with varied sensitivity maps to reconstruct the undersampled dataset. The AF in parallel imaging is limited by the degradation of SNR. Compressed sensing is another option which has already shown a great potential to overcome the limitations of general acceleration techniques like AF, spatial and temporal resolution, etc. (21,22).

Compressed sensing for dynamic MRI imaging is implemented based on the fact that continuously acquired image series express sparsity in temporal domain with appropriate sparsity transforms like temporal TV (105-107). An irregular undersampling pattern is required to induce incoherent artefacts on temporal dimension. The image series can be recovered by exploring temporal sparsity with a nonlinear reconstruction algorithm. Currently, compressed sensing is an increasingly powerful approach to accelerate data acquisition in dynamic MRI. Multiple compressed sensing accelerated reconstruction schemes have been proposed for dynamic MRI. In this chapter, two popular reconstruction schemes incorporated with the stack-of-stars golden angle sampling pattern for dynamic MRI

are introduced in detail. An advanced reconstruction framework is developed for improving the dynamic performance. The performance of the proposed method and the other two schemes were compared and quantified within a simulated dataset and several clinic liver DCE-MRI datasets.

## 6.1 Golden Angle Radial Sparse Parallel

Golden Angle Radial Sparse Parallel (GRASP) is a recently proposed technique which combines motion-robustness and temporal incoherence of stack-of-stars golden radial sampling pattern, acceleration capability of parallel imaging and compressed sensing for highly accelerated free-breathing DCE-MRI (108). A variety of research work has shown the priority of GRASP for free-breathing imaging of body tissues like abdomen and prostate (108-110). The basic framework of GRASP is shown in Figure 6-1:

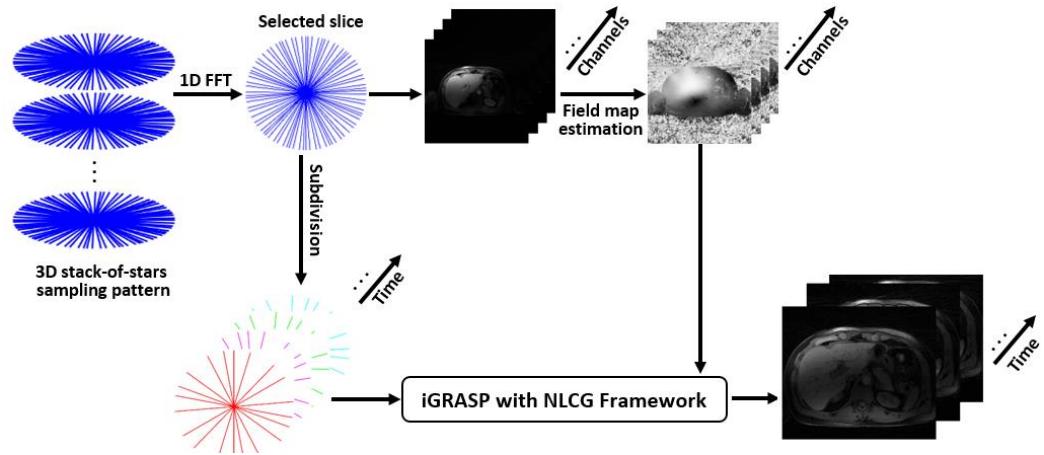


Figure 6-1: GRASP reconstruction framework. Field maps are extracted from multi-coil reference images which are given by the coil-by-coil NUFFT reconstruction of the k-space data at a certain slice. The k-space is decomposed by 1D FFT on the slice dimension in hybrid 3D datasets. The spokes are first resorted into undersampled dynamic time frames according to the acquisition time order. The GRASP reconstruction with NLCG algorithm is then applied to recover the image series by exploring the temporal sparsity among the subdivided time frames.

The overall acquired 3D dataset is fully sampled by stack-of-stars golden angle sampling pattern. The slices are decomposed by implementing FFT function on the partition dimension at first. Each slice image is then reconstructed by NUFFT directly without undersampling artefacts while these images are the temporally averaged results among the total scan duration. The dynamic variation along the temporal dimension is lost. These slice images are regarded as reference images and used to estimate multi-channel field maps by some post-imaging processing algorithms like Walsh algorithm (38) and ESPIRiT method (39). Consecutively, the fully sampled dataset was subdivided into multiple frames according to the time order. The sub-sampling patterns between these time frames are different which offers additional incoherence along the temporal dimension as shown in Figure 6-2.

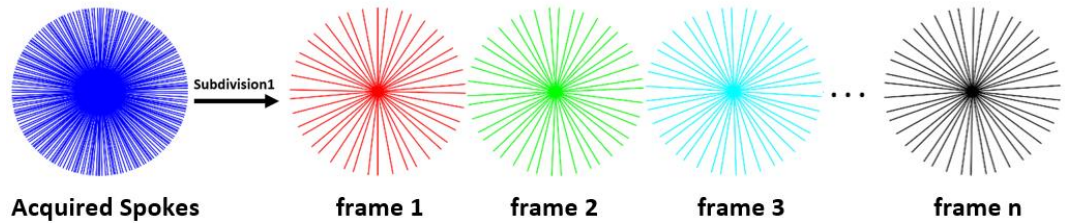


Figure 6-2: Time frame subdivision from the fully golden angle sampled k-space dataset. The sub-sampling pattern within time frames is different between each other, offering the temporal sparsity.

GRASP employs temporal TV as the sparsity transform to explore the temporal sparsity among subdivided time frames. The corresponding reconstruction model is mathematically expressed as:

$$\operatorname{argmin}_x = \frac{1}{2} \|FCx - b\|_2^2 + \lambda_T \|Tx\|_1 \quad (6.1)$$

where  $x$  is the subdivided time frame series to be reconstructed while  $b$  is the acquired dataset.  $C$  and  $F$  represent the multi-channel field maps and the encoding

operator respectively. The combination of  $C$  and  $F$  works as the multi-channel encoding operators, performing the compressed SENSE model to improve the reconstruction quality further.  $T$  is the temporal sparsity transform while it is typically selected as temporal TV in GRASP.  $\lambda_T$  is the penalty factor applied on the sparsity constraint which trades off the data consistency versus the complexity of solution given by  $L_1$  norm  $\|\cdot\|_1$ .

GRASP shows superiority in imaging static tissues. NLCG (42) is employed to obtain the optimal solution of GRASP model. However, the repeated gridding/de-gridding procedures in NLCG result in an excessive long reconstruction period. Besides the reconstruction efficiency, periodic rigid motion is another challenge for GRASP. During the imaging of tissues with rigid motion like liver and lung, some degree of motion blurring still exists in the reconstructed image which degrades the reconstruction quality of GRASP.

## 6.2 L+S Decomposition

Besides the GRASP based technique, combining compressed sensing and low-rank completion has shown priority in the reconstruction of highly undersampled dynamic MRI (111-113). Similar to the GRASP, the dataset is acquired by stack-of-star golden angle sampling pattern in the L+S decomposition. NUFFT is directly implemented to reconstruct the slice images while these slice images are used to estimate field maps by post-processing techniques. Consecutively, the spokes acquired in each slice are subdivided into multiple time frames according to the temporal order.

Besides the temporal subdivision, L+S approach decomposes the time frame series matrix  $M$  into a low-rank matrix  $L$  and a sparse matrix  $S$  which present a slowly

varied background component and a dynamic component respectively (114,115).  $S$  shows sparsity in the initial y-t space due to the compressed background. Sparser representation of  $S$  is achieved in an appropriate transform domain such as temporal TV where dynamic components are intrinsically sparse (113). Consequently, fewer measurements are required to recover the image series which enables a higher AF for dynamic MRI. The L+S decomposition approach is mathematically formulated as:

$$\operatorname{argmin}_{L,S} = \frac{1}{2} \|E(L + S) - b\|_2^2 + \lambda_L \|L\|_* + \lambda_T \|TS\|_1 \quad (6.2)$$

where  $b$  is a reshaped column of the acquired dataset while it is typically decomposed into  $L$  and  $S$  by Singular Value Decomposition (SVD) and Singular Value Thresholding (SVT) (113).  $E$  is a multi-coil encoding operator (equivalent to the combination of  $C$  and  $F$  in GRASP model) and  $T$  is the temporal sparsity transform which is typically selected as temporal TV.  $\lambda_L$  and  $\lambda_T$  are regularization weights designed empirically to balance the data consistency of  $\|E(L + S) - b\|_2^2$  and complexity of the solution given by the nuclear norm  $\|\cdot\|_*$  and  $L_1$  norm  $\|\cdot\|_1$ .

L+S model can express the dynamic image series naturally and offers higher temporal fidelity and robustness at high fold undersampling reconstructions. ISTA (43) provides faster convergence speed for L+S decomposition compared with NLCG in GRASP.

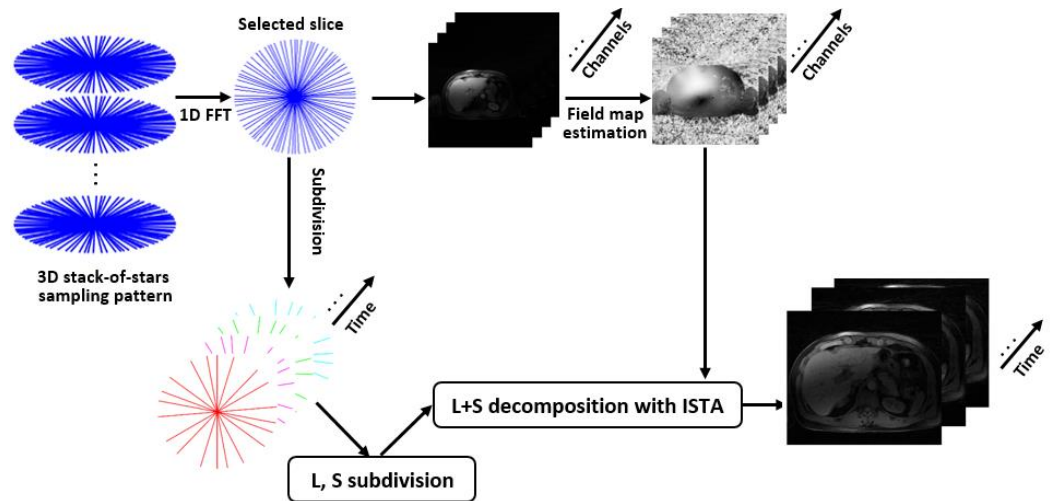


Figure 6-3: L+S decomposition reconstruction framework is similar to the previous iGRASP reconstruction framework. The spokes are first resorted into undersampled dynamic time frames according to the acquisition time order. A further subdivision is implemented on time frames to decompose low-rank components and sparse dynamic components in time series. The L+S decomposition reconstruction with ISTA algorithm is then applied to recover the image series by exploring the temporal sparsity among the dynamic sparse components.

### 6.3 Temporal Sparsity Constraints

Appropriate sparsity transform is required to express the MR images sparsely while the noise-like artefacts induced by undersampling have negligible magnitude in the transform domain, enabling the recovery of lossless MR images from the highly undersampled datasets. In DCE-MRI, background information is in a steady state while there is a limited temporal variation in the background region among time frames. Thus, the dynamic datasets are intrinsically sparse along the temporal dimension while a variety of temporal sparsity transforms such as temporal FFT, temporal PCA and temporal TV (46,116-118), etc. have been introduced in different studies to exploit this sparsity. Temporal TV has shown the advanced performance for compressing the undersampling artefacts. Both L+S decomposition and GRASP

based techniques typically employ temporal TV as the sparsity transform to promote sparsity among multi-coil datasets (108,113).

Temporal TV can compress all the temporal variations including temporally incoherent undersampling artefacts effectively, but it also leads to temporal averaging to some extent. SNR of the background regions is improved by “temporal averaging” effect as they are in equilibrium states. Nevertheless, dynamic contrast signal induced by injecting agent is gradually varied along the temporal dimension (101,102). The averaging effect degrades the dynamic contrast of DCE-MRI.

Temporal FFT is another sparsity transform which reserves the dynamic contrast better for DCE-MRI. In temporal FFT transform domain, the DC component and a few low frequency components typically occupy most of the power and they present the steady background and tissues with relatively slow change along the temporal dimension respectively. Temporal sparsity is explored by temporal FFT by gradually eliminating frequency components with negligible magnitude. The intensity of DCE signal is assumed to be varying temporally at low frequency. Few low frequency components are sufficient to match the relatively smooth variation of signal intensity of blood vessels. These low frequency components are reserved by temporal FFT while the dynamic contrast is maintained.

We introduce both the temporal FFT and temporal TV here, forming joint sparsity transform for L+S model. We combine the merits of temporal TV for compressing the artefacts and temporal FFT for maintaining the dynamic contrast simultaneously for an improved DCE-MRI reconstruction. The basic reconstruction framework of L+S decomposition in Figure 6-3 is maintained.

## 6.4 L+S with Joint Sparsity

The temporal TV constraints typically degrades dynamic contrast besides removing undersampling artefacts. We have introduced an additional sparsity constraint Temporal FFT into the L+S decomposition to recover the dynamic contrast as:

$$\operatorname{argmin}_{L,S} = \frac{1}{2} \|E(L + S) - d\|_2^2 + \lambda_L \|L\|_* + \lambda_T \|TS\|_1 + \lambda_F \|FS\|_1 \quad (6.3)$$

where  $F$  is the temporal FFT transform and  $\lambda_F$  is its corresponding penalty factor. The standard L+S decomposition employs the SVD and ISTA to solve the optimization problem in Equation 6.2 and achieves high computation efficiency (113).

SVD and shrinkage & thresholding operators are employed to obtain the low rank and sparse components. Soft-thresholding is consecutively implemented to process the temporal TV constraint to obtain the optimal solution of the L+S decomposition model. The number of gridding/de-gridding procedures is drastically reduced while the reconstruction efficiency of L+S decomposition is much higher than standard GRASP. To accelerate the convergence further, Beck has developed an advanced ISTA algorithm named FISTA (44). Besides the basic framework of ISTA, FISTA contains a specific linear combination procedure of previous two iterative stages. Hence, FISTA preserves the computation simplicity of ISTA but with a better convergence rate.

However, both ISTA and FISTA cannot solve the reconstruction model with multiple  $L_1$  regularizations efficiently. To solve the L+S with joint sparsity model

in the Equation 6.3, the fast composite splitting algorithm (FCSA) (47,119), a combination of FISTA and composite splitting algorithm (CSA) (120), is employed in this work. CSA is implemented to split the problem with joint sparsity constraints into two sub-problems with a certain constraint and solve them separately. A linear combination of the solutions for two sub-problems is regarded as the solution for the entire problem. Figure 6.4 shows the procedures of FCSA for solving the L+S with joint sparsity in the proposed method.

The reconstructed image matrix  $M$  is processed by the SVD, forming  $M = U\Sigma V^H$ . A shrinkage operator is defined as  $\Lambda_\lambda(x) = \frac{x}{|x|} \max(|x| - \lambda, 0)$  where  $x$  is the input value and  $\lambda$  is the threshold with real value to build the SVT operator. SVT operator is applied for processing singular decomposition of  $M$  as  $SVT_\lambda = U \Lambda_\lambda V^H$  during the first iteration. The background component  $L$  is figured out by applying thresholding on the singular value of the matrix while the dynamic component  $S$  is also obtained by  $S = M - L$ . SVT operator is consecutively implemented to soft-thresholding the singular value as  $L_k = SVT(M_{k-1} - S_{k-1})$  in the  $k$ th iteration. Shrinkage-operator is applied for constraints in the temporal TV domain as  $S_{Tk} = T^{-1}(\Lambda_{\lambda T}(T(R_k - L_{k-1})))$  and in temporal FFT domain as  $S_{Fk} = F^{-1}(\Lambda_{\lambda F}(F(R_{k-1} - L_{k-1})))$  respectively. The solution of the dynamic components is obtained as a linear combination of the solutions in temporal FFT and temporal TV domains i.e.  $S_k = (S_{Tk} + S_{Fk})/2$ . The image series  $M_k$  is recovered by subtracting the residual signal  $M_k = L_k + S_k - E^*(E(L_k + S_k - d))$  from  $L_k + S_k$  to maintain data consistency.  $R_{k+1}$  is the input which is a specific linear combination of the previous two points  $M_{k-2}$  and  $M_{k-1}$  for the next iteration.

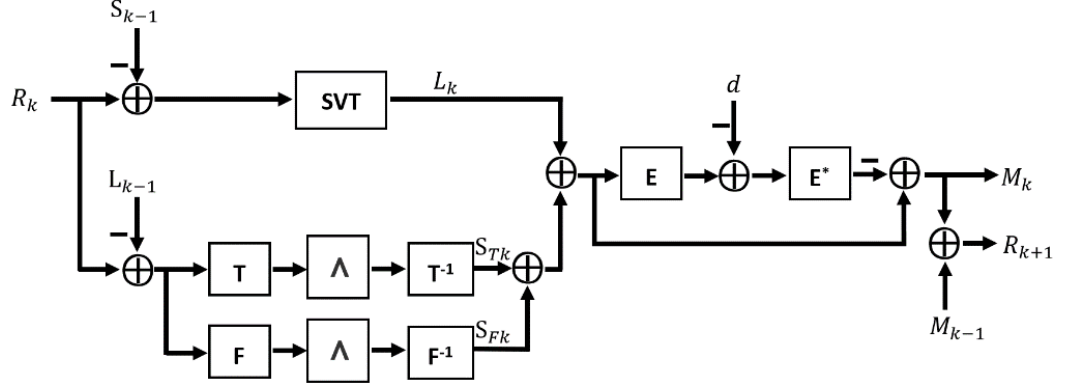


Figure 6-4. Operation for  $k$ -th iteration in the L+S decomposition with joint sparsity reconstruction framework.  $L_k$  is obtained by applying SVT for  $R_{k-1} - S_{k-1}$ . A shrinkage operator is implemented to the sparsity constraints in both the  $T$  and  $F$  domains to get  $S_{T_k}$  and  $S_{F_k}$  respectively.  $S_k$  is figured out by a linear combination of  $S_{T_k}$  and  $S_{F_k}$ . Image series  $M_k$  is then recovered as  $M_k = L_k + S_k$ . Additional residual signal  $E^*(E(L_k + S_k - d))$  is then subtracted to maintain the data consistency. The updated input  $R_{k+1}$  for the next iteration is obtained by a specific linear combination of the previous two points  $M_{k-2}$  and  $M_{k-1}$  which enforces faster convergence.

## 6.5 Dynamic Simulation with Model Phantom

In the previous chapters, we have demonstrated the basic principle of GRASP and L+S decomposition for accelerated dynamic imaging. An additional sparsity constraint is integrated into the L+S decomposition for reducing temporal averaging and improving dynamic contrast simultaneously. In this chapter, the performance of L+S with joint sparsity and other two reconstruction schemes are quantified by a simulated phantom dataset and several clinical liver DCE-MRI datasets.

It is typically difficult to acquire the fully sampled DCE-MRI dataset at high temporal resolution during clinical scans (101). The performance of different reconstruction schemes cannot be quantified due to the absence of reference images.

In this work, a simulated DCE-MRI dataset with fully sampled reference image

series enables the quantification of the dynamic contrast performance of the proposed method and the other two reconstruction schemes.

### **6.5.1 Phantom with Dynamic Variation**

A 2D Shepp-logan based computer model with a total of 384\*384 voxels was designed with dynamic contrast variation. Some MRI effects including  $T_2$  decay and  $B_0$  inhomogeneity are ignored during the simulation. The dynamic signals are exactly varied with the curve obtained in the clinical scan.

The phantom model consists of three background sections and six dynamic variation sections as shown in Figure 6-5. The gray level of three background regions was designed as 1, 0.4 and 0.2 respectively. The signal intensity of these background sections was kept in constant, forming the tissues without contrast enhancement.

A dynamic curve with 588 discrete points between the pre-contrast phase and the arterial phase was created based on the reference curve obtained in clinical DCE-MRI dataset. The magnitude of this dynamic curve ranges from 0 to 1. The virtual time gap between adjacent discrete points was designed as 0.143s. The arterial phase with peak dynamic signal intensity was arranged at the 187<sup>th</sup> point (26.6s) of the curve model. The signal intensity of dynamic sections was varied with this dynamic curve during the simulation as shown in Figure 6-6.

Figure 6-7 shows the process of generating a simulated dataset in detail. Eight exponentially decayed field maps are introduced to modify the signal intensity of phantom model point by point, forming multiple virtual coil channels. A golden angle (111.246°) radial sampling pattern was simulated during the dynamic period.

The sampling was executed by the NUFFT toolbox for accelerating the simulation (108). A certain radial spoke with 384 sample points was acquired at each discrete time point over the 84s virtual dynamic period. The ultimately acquired dataset contains 8 channels, a total of 588 spokes with 384 readout points within each spoke. An averaging image was directly reconstructed by NUFFT for the estimation of field maps. Another fully sampled matrix (588 spokes and 384 read point in each spoke) was acquired at each discrete time point simultaneously, forming the fully sampled reference. The matrix size for the reference dataset was  $384 \times 588 \times 588$ .

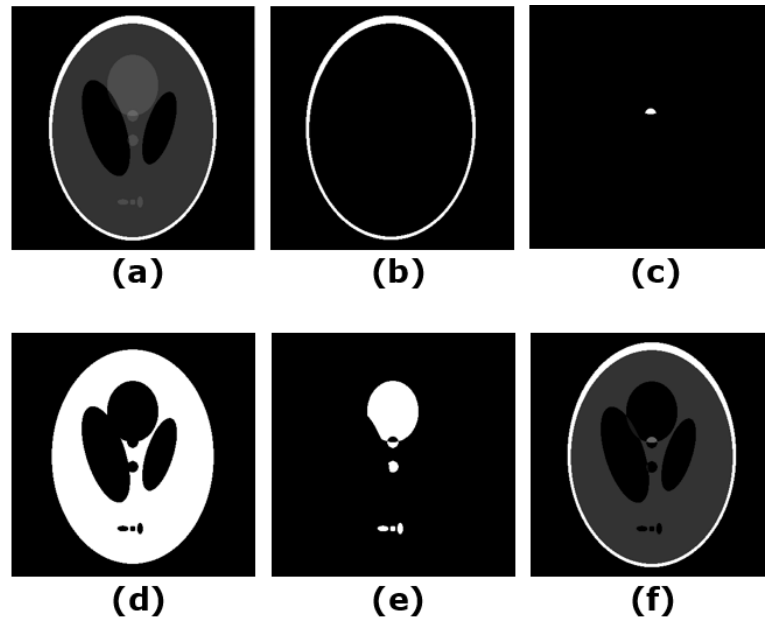


Figure 6-5: Design of Shepp-logan model for dynamic simulation: (a) A general Shepp-logan computer model provided by Matlab. (b)~(d) Three phantom background sections, the signal intensity of these sections was kept constant as 1 and 0.4 and 0.2 respectively. (e) Six dynamic sections of computer model, the signal intensity of these sections were varied by the dynamic curve. (f) The ultimate computer model before contrast enhancement.

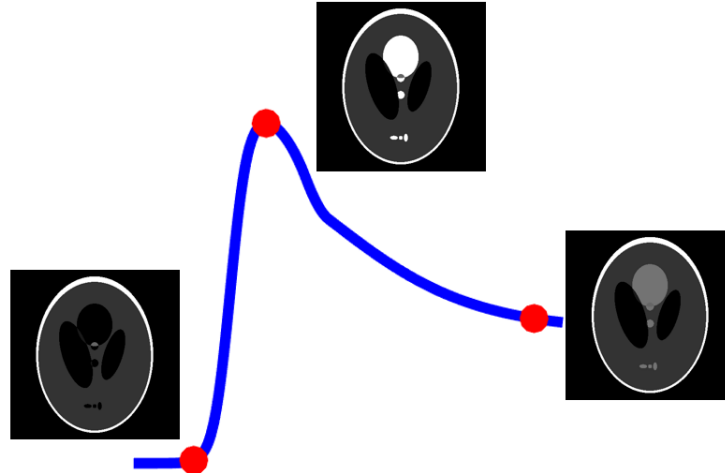


Figure 6-6: Signal intensity variation of dynamic sections in the computer model. A dynamic curve was created according to the DCE signal variation model obtained in clinical datasets. The dynamic curve model contains a total of 588 discrete points between pre-contrast phase and venous phase. The signal intensity of dynamic sections in phantom model was modified by this dynamic curve. The maximum dynamic signal occurs at 187<sup>th</sup> point, forming central arterial phase.

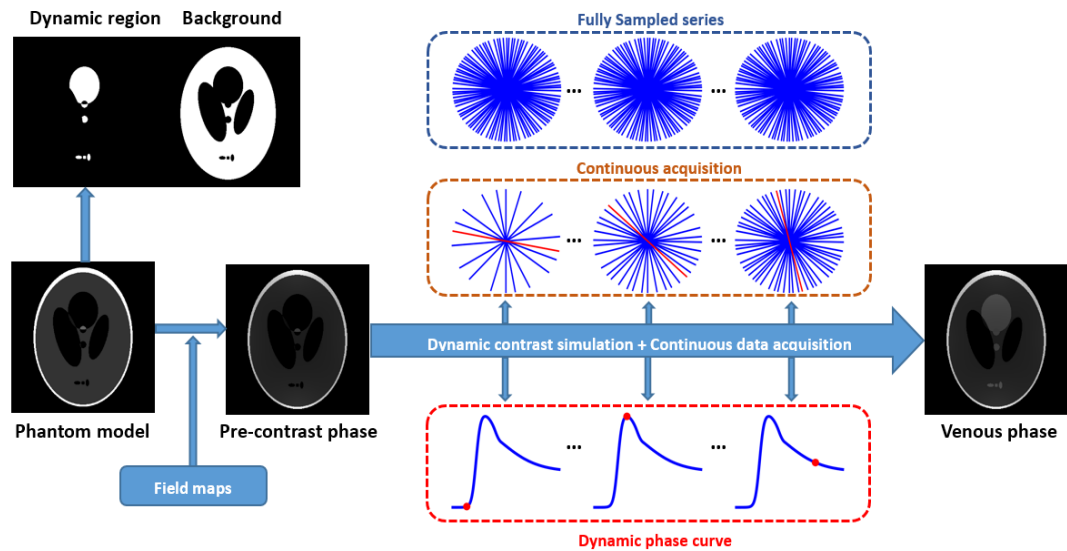


Figure 6-7: Flowchart of data acquisition during dynamic variation period. 8 field maps were integrated into phantom before data acquisition forming multiple virtual coil channels. The simulation of data acquisition contains a total of 588 steps between pre-contrast phase and venous phase. Two data acquisitions were executed at each time point, producing fully sampled reference DCE series and continuous DCE phantom dataset respectively.

## 6.5.2 Reconstruction Parameter Design

The simulated dataset was subdivided into 21 time frames with the temporal resolution 28 spokes/frame (4 s/frame). According to the Nyquist sampling standard, The corresponding AF is  $(384 \times 0.5\pi)/28 = 21$ .

The image series were reconstructed with a matrix size of  $384 \times 384 \times 21$  by NUFFT, GRASP, L+S decomposition and L+S with joint sparsity respectively. The source codes of GRASP and L+S decomposition were downloaded from the authors' websites (108,113). The optimization problem in GRASP was solved using NLCG with 24 iterations. The iteration number for both ISTA and FCSA was set as 20 and used to solve the optimization problem in L+S decomposition and L+S with joint sparsity respectively. All the reconstructions were performed using MATLAB 2020b (MathWorks, Natick, MA) on an Intel Core i7-10700 PC with a 2.9 GHz processor. The reconstructions of three schemes were repeated 10 times to quantify their reliable reconstruction efficiency accurately.

The weighting factors of sparsity constraints directly determine the image quality of reconstructed series. The regularization parameter of Temporal TV  $\lambda_T$  in all three reconstruction schemes was set the same for a fair comparison. To determine the optimal weighting factor for temporal TV, a variety of GRASP and L+S decomposition reconstructions were executed with the different  $\lambda_T$  ranging from  $0.1 * M_s$  to  $0.8 * M_s$  (step size 0.05), where  $M_s$  presents the maximum magnitude of the images series directly reconstructed by NUFFT. According to the evaluation of two experienced radiologists, an optimized value  $\lambda_T = 0.2 * M_s$  was

implemented for all three reconstruction schemes.  $\lambda_L$  and  $\lambda_T$  in proposed method followed the same setup as in L+S decomposition model.

Similar to the design of  $\lambda_T$ . Different values of  $\lambda_F$  were combined with the other two regularization parameters in L+S with joint sparsity. An adequate value of  $\lambda_F$  was designed for reconstruction with specific temporal resolution by testing different values and comparing the image quality as well as dynamic contrast signal intensity and ultimately selected by experienced radiologists. Besides the regularization parameters, other reconstruction parameters in GRASP, L+S decomposition and L+S with joint sparsity were carefully followed by authors' setups (108,113).

### **6.5.3 Quantification of Dynamic Performance**

The gray level of all reconstruction results has been normalized according to the mean value of steady background sections for comparing the dynamic contrast. Figure 6-8 shows three contrast phases of the Shepp-logan phantom images reconstructed by GRASP, standard L+S decomposition and L+S with joint sparsity respectively. All three reconstruction schemes successfully removed undersampling artefacts. The dynamic contrast in the selected region was visually degraded in three reconstruction schemes compared to the reference image. Besides the degradation of peak dynamic signal, temporal averaging also resulted in unexpected dynamic enhancement in the pre-contrast phase in three reconstruction schemes. There was no obvious dynamic degradation obtained in fully sampled reference series. The peak of dynamic signal was degraded by only 3.3% in reference, certifying the dynamic robustness of fully sampling.

The peak of dynamic signal was degraded by 17.6% and 20.3% for GRASP and standard L+S method compared to the reference, as shown in Table 6-1. GRASP provided a little bit better dynamic contrast than standard L+S decomposition as shown in Figure 6-9. With the support of an additional sparsity constraint, the best dynamic contrast was achieved by the proposed reconstruction scheme. The peak of dynamic signal was only degraded by 12.4% in the proposed method which is much lower than the standard L+S decomposition. Using the reference dynamic curve as the benchmark, the Euclidean distance of our proposed method is only 0.182 which is much smaller than 0.256 for GRASP and 0.306 for standard L+S method, suggesting that our proposed method can capture the dynamic varying arterial signals much better.

The average reconstruction time of GRASP is 490 s. Two L+S based methods showed much higher reconstruction efficiency while 111 s and 114 s are required by standard L+S decomposition and the proposed method. With the support of FCSA, an increase of 3% computation cost was caused by an additional sparsity constraint in the proposed method compared to standard L+S decomposition. The proposed method and standard L+S decomposition achieved similar reconstruction efficiency by using only about 25% of computation time for GRASP.

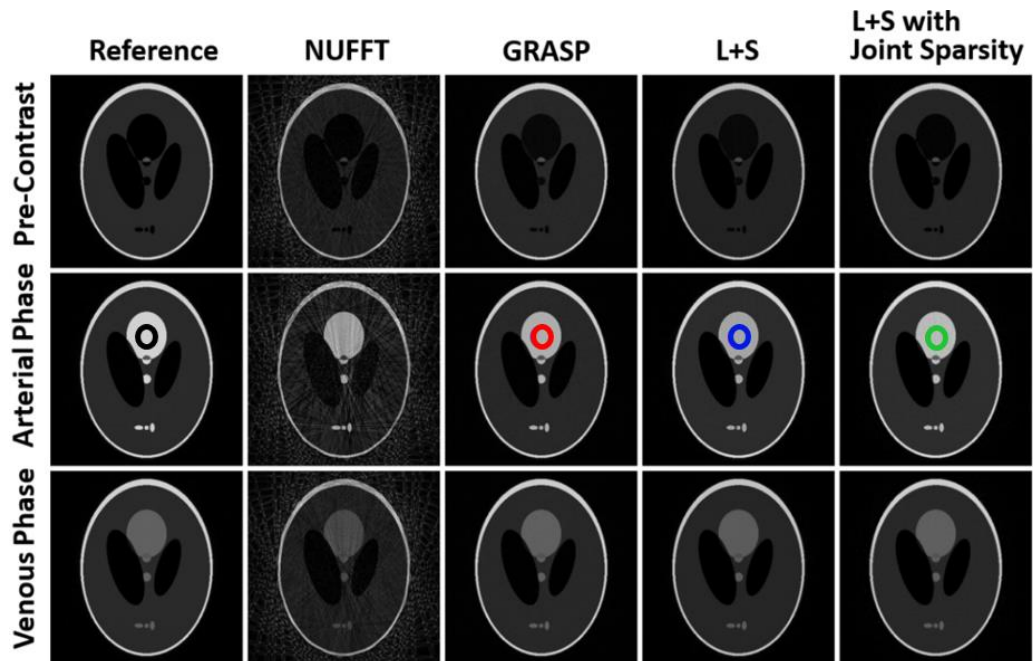


Figure 6-8: Three phase images corresponding to the reconstruction of the simulated phantom dataset at AF=22 (a total of 588 radial spokes and temporal resolution of 28 spokes/frame) using NUFFT, GRASP, L+S decomposition and the proposed method. Signal intensity in the selected region (labelled by circles) among all the frames was used to estimate the dynamic contrast performance in different reconstruction schemes.

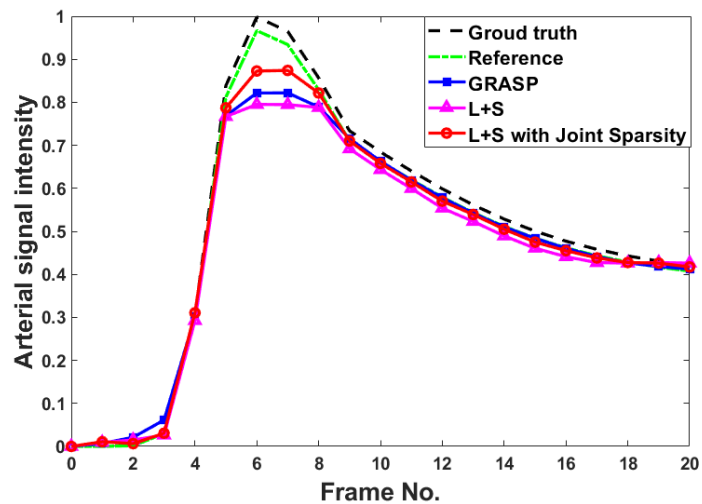


Figure 6-9: Dynamic signal variation for the phantom using ground truth, fully sampled reference, GRASP, L+S and L+S with joint sparsity. Using the ground truth and fully sampled reference as the benchmark, our proposed L+S with joint sparsity method demonstrated much better dynamic contrast compared with GRASP and standard L+S.

Table 6-1: Reconstruction time, Peak DCE signal and Mean DCE signal of the three reconstruction schemes in the simulated Phantom data. Reconstruction efficiency has been significantly improved in the proposed method due to L+S reconstruction while joint sparsity improved dynamic contrast in the proposed method.

<b>Reconstruction Scheme</b>	<b>Euclidean Distance</b>	<b>Reconstruction Time (sec)</b>	<b>Peak DCE signal</b>	<b>Mean DCE signal</b>
<b>Reference</b>	0.0829	-	0.9675	0.4832
<b>GRASP</b>	0.2557	490	0.8225	0.4701
<b>L+S decomposition</b>	0.306	111	0.7959	0.4575
<b>Proposed Method</b>	0.1819	114	0.8747	0.4742

## 6.6 Clinic Dataset and Reconstruction

Two liver DCE-MRI datasets provided by Lifeng research group were implemented to evaluate the clinical performance of different reconstruction schemes (108,121). The liver DCE-MRI was performed in two healthy volunteers on whole-body 1.5T scanners (MAGNETOM Avanto, Siemens AG, Healthcare Sector, Erlangen, Germany) incorporated with 12 channel body coil. Data acquisition was completed by a 3D FLASH based stack-of-star golden angle sampling pulse sequence with frequency selective fat suppression (transverse scan). An intravenous injection of 10 ml of gadopentate dimeglumine (Gd-DTPA) (Magnevist, Bayer Healthcare, Leverkusen) followed by a 20 ml saline flush was initiated accompany with the data acquisition simultaneously. The injection rate for both contrast agents was 2 ml/second. The total acquisition time is around 90 s.

The corresponding parameters for the acquired liver dataset included: TR/TE=3.52 ms/1.41 ms, FA=12°, FOV=370\*370 mm<sup>2</sup>, the total acquisition time is around 90 s. The acquired dataset contains: 12 channels, 40 partitions and a total of 600 spokes with 768 readout points in each spoke. The central 384 readout points in each spokes were remained for reconstruction. After 1D FFT along the slice dimension, a 2D slice corresponding to the central liver section was selected to evaluate the reconstruction performance. To reduce the computation burden and further alleviate streaking artefact, the 2D liver dataset was processed by coil unsteaking (122) and coil compression (123) prior to the reconstruction. The dataset was compressed from 384\*600\*12 to 384\*600\*8.

Following the same reconstruction arrangements in the phantom dataset, the liver dataset was subdivided into 21 frames between the pre-contrast phase and the arterial phase with the temporal resolution of 28 spokes/frame (4 s/frame). The corresponding acceleration ratio is AF=21. Image series were reconstructed using NUFFT, standard GRASP, L+S decomposition and L+S with joint sparsity.

All the time frames were reconstructed with the matrix size of 384\*384. The dynamic performance and image quality of GRASP, L+S decomposition and L+S with joint sparsity were compared without consideration of the respiratory motion. Furthermore, additional reconstructions for these three schemes were performed at temporal resolution 14 spokes/frame and 21 spokes/frame, certifying the robustness of L+S based techniques for highly under-sampled reconstruction.

All the reconstruction parameters including  $\lambda_T$  of GRASP followed the same setup of Lifeng (108). The same value of  $\lambda_T$  was set for two L+S based reconstruction

schemes for a fair comparison. The value of  $\lambda_F$  in the proposed method following the same setup in previous phantom reconstructions. Other parameters of L+S and L+S with joint sparsity followed the same setup of Otazo (113).

## 6.7 Image Analysis and Statistics

Figure 6-10 shows a comparison of three reconstruction schemes in the three representative contrast phases in a free-breathing liver DCE-MRI dataset at AF=22 (28 spokes/frame). The respiratory motion was not compensated here. Due to the increase of complexity of the imaging object, the reconstruction period for the liver dataset was typically larger than that for the simulated phantom dataset. The average reconstruction time for GRASP, L+S decomposition and L+S with joint sparsity is 705 s, 182 s and 185 s respectively. Two L+S based reconstructions schemes still achieved around 4 times faster reconstruction speed than the GRASP method. The extension of reconstruction period in the proposed method is still negligible compared with standard L+S decomposition.

Two L+S based techniques present better background structures of liver. Better dynamic contrast of tissues (labelled by solid arrows) was observed in GRASP and the proposed method. Blurring was observed in the standard L+S reconstruction (labelled by dashed arrows) due to the degradation of dynamic contrast.

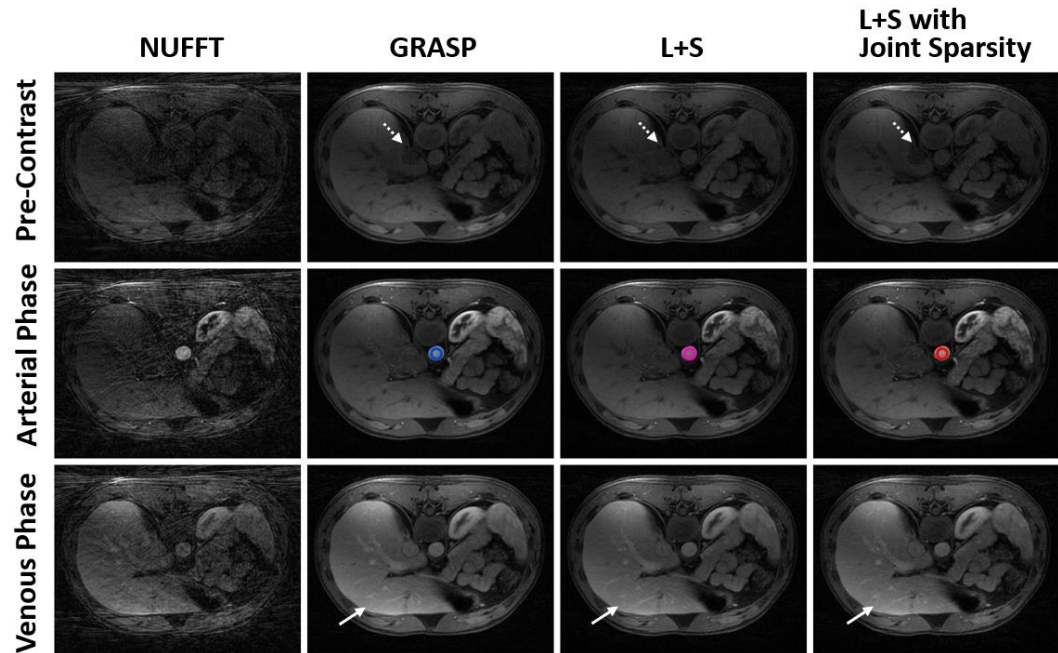


Figure 6-10: A comparison of different reconstruction schemes in the three representative phases in a liver DCE-MRI dataset at AF= 22 and 28 spokes/frame. Both our proposed method and the standard L+S method provide better background structures than GRASP. Our L+S with joint sparsity followed by FCSA demonstrated better dynamic contrast (solid arrow and dashed arrow). Arterial signal intensity in the selected region (labelled by circles) among all the frames was used to estimate the dynamic contrast performance in different reconstruction schemes.

The arterial section in reconstructed series was labelled while the average signal intensity in arterial region was regarded as the dynamic signal. There was no available reference for the clinical DCE-MRI dataset. The peak and average value of the dynamic signal curve in the selected arterial region were regarded as the standards to assess the dynamic performance and temporal fidelity of reconstruction frameworks.

Figure 6-11 shows the dynamic signal variation in the selected arterial region in NUFFT, GRASP, L+S decomposition and L+S with joint sparsity for a liver DCE-MRI dataset. The peak dynamic signal in liver dataset in the proposed method

demonstrated an increase in peak dynamic DCE signal by 24.8% and 33% than that of GRASP and standard L+S method respectively. Clear improvement of dynamic contrast was achieved by utilizing joint sparsity constraints in the proposed method.

Figure 6-12 demonstrates a further comparison of three reconstruction schemes in the venous phase at different AF=22, 29 and 43 in a liver DCE-MRI dataset. Visible blurring artefact was obtained in GRASP at AF=43. The detail of abdomen tissues is not degraded significantly in L+S decomposition and L+S with joint sparsity. The L+S based schemes show the robustness for highly undersampled dataset reconstruction.

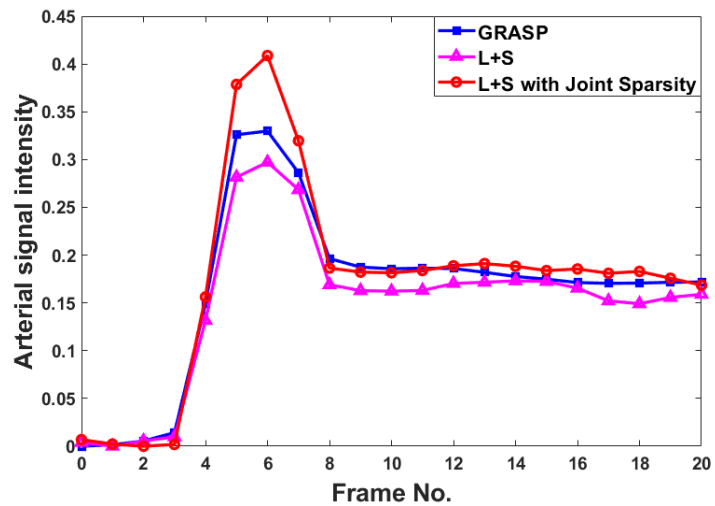


Figure 6-11: Dynamic signal variation in the arterial region for the liver DCE-MRI dataset by using GRASP, L+S and L+S with joint sparsity. Improved dynamic contrast was achieved by our proposed L+S with joint sparsity. Significant improvement of peak dynamic signal was observed in proposed L+S with joint sparsity.

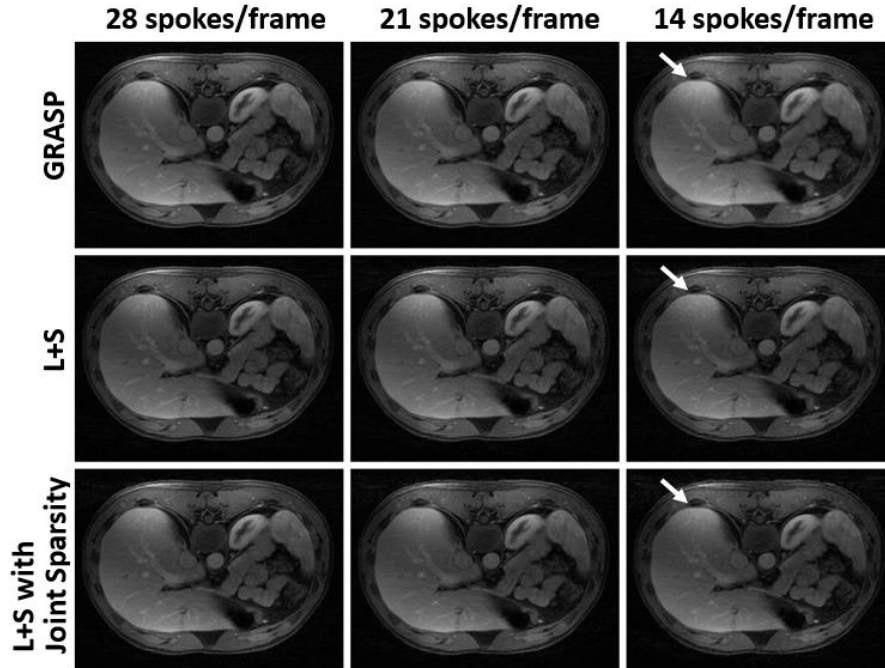


Figure 6-12: A comparison of the reconstructed images of GRASP, L+S decomposition and L+S with joint sparsity at different temporal resolutions in the venous phase of a liver DCE-MRI dataset. A total of 21, 28 and 42 frames were reconstructed at different temporal resolutions respectively. Blurring artefacts and degradation of image quality as observed in GRASP. Fewer blurring artefacts and degradation were observed in L+S with joint sparsity. The penalty factor for the three reconstruction schemes was set the same among all the reconstructions.

## 6.8 Discussion

DCE-MRI requires rapid data acquisition to monitor the fast signal-intensity changes during the contrast agent period. The general acceleration techniques like parallel imaging and 2D compressed sensing cannot achieve the excessive AF and maintain the image quality simultaneously.

Based on the fact that majority of background tissues are in steady states during the scan, the image series are intrinsically expressed on temporal dimension. Implementing compressed sensing to explore the temporal sparsity of image series

is an effective method to achieve high spatial-temporal resolution reconstruction for DCE-MRI.

Stack-of-stars golden angle radial sampling perfectly satisfies the requirement of temporal compressed sensing. A continuous data acquisition model is sufficient to cover the whole dynamic variation period. Then the acquired spokes are subdivided into multiple time frames according to the temporal acquisition order. The sub-sampling patterns among time frames are completely different which induce incoherent streaking artifacts among the time series. Meanwhile, due to the repeatedly acquired k-space center, the image contrast of radial sampling corresponds to the average over the acquisition window. This averaging effect offers intrinsic motion robustness for radial sampling, enabling a free-breathing scan.

Two reconstruction frameworks GRASP and L+S decomposition are introduced in this chapter for dynamic imaging with high spatial-temporal resolution. Both of them combines parallel imaging, compressed sensing and golden angle radial sampling pattern to explore the temporal sparsity and compress undersampling artefacts effectively. Both two reconstruction framework shows significant advantage in imaging static tissues. The tissues information is recovered successfully while the streaking artefact is compressed effectively.

To reconstruct a series of DCE-MRI images on the temporal dimension, the overall reconstruction period of two frameworks is significantly extended compared with the general 2D compressed sensing. GRASP implements NLCG algorithm to find the optimal solution. However, the repeated gridding/de-gridding steps result in

extremely low reconstruction efficiency. To reconstruct the images series at high temporal resolution, dozens of minutes may be required by GRASP to complete the iteration.

With the support of ISTA, a much faster convergence speed is achieved in L+S decomposition. The number of gridding procedures is significantly reduced by ISTA as well. The overall reconstruction efficiency of L+S decomposition is much higher than that of GRASP. Several minutes are typically sufficient to complete the reconstruction in L+S decomposition. Through subdividing the image series into low-rank background components and dynamic sparse components, L+S decomposition also offers higher temporal fidelity and better tissue contrast at excessively high AF.

Both GRASP and L+S decomposition employ temporal TV as sparsity transform to promote sparsity among multi-coil datasets. Additional temporal averaging was produced by temporal TV, leading to unexpected dynamic contrast degradation. With the same penalty factor design, L+S decomposition experienced more dynamic degradation. To maintain the image quality, and recover the dynamic contrast, an additional sparsity constraint has been introduced into the L+S decomposition in this chapter. The low frequency components in temporal domain were assumed to be sufficient to match the dynamic variation curve. The FCSA was implemented to solve the optimization problem with joint sparsity effectively, maintaining the merit of reconstruction efficiency in L+S based method.

During clinical scans, it is difficult to obtain the fully sampled reference dataset with sufficiently high spatial-temporal resolution. The performance of DCE-MRI

reconstruction is typically evaluated by experienced radiologists (108). There is no standard evaluation criteria for quantifying the performance of different reconstruction schemes. Hence, a simulation framework was created here. The benefit of Bloch equation simulation is that the ground truth like dynamic signal variation is obtained exactly. The dynamic performance of the proposed method and other reconstruction schemes were enabled by the parameters like Euclidean distance and magnitude of the dynamic signal.

The proposed L+S with joint sparsity achieved improved dynamic contrast and better image quality when comparing with GRASP and standard L+S decomposition in reconstructing the simulated phantom dataset and the liver DCE-MRI dataset. Meanwhile, both standard L+S decomposition and the proposed L+S based methods achieved around 4 times faster reconstruction speed than the GRASP method. The computation cost from additional sparsity constraint is negligible with the support of FCSA.

## **6.9 Conclusion**

L+S with joint sparsity demonstrates the use of combining L+S model with joint sparsity constraints for improved dynamic contrast, high temporal resolution and computationally efficient free-breathing DCE-MRI. The improvement of dynamic contrast provides better image quality and tissues contrast which benefits the clinical diagnosis a lot. The use of FCSA algorithm minimized the computation cost caused by the additional sparsity constraint. The merit of fast reconstruction enables a wide range of on-line clinical applications.

## **Chapter 7 Motion Corrected DCE-MRI**

In previous chapters, we have quantified the performance of GRASP, standard L+S decomposition and L+S with joint sparsity in terms of image quality, dynamic contrast and reconstruction efficiency, etc. The k-space data acquired by the golden angle radial sampling pattern offers additional temporal sparsity and motion robustness for GRASP and L+S decomposition. However, the radial sampling is insufficient to compress the artefacts caused by periodic rigid motion such as respiratory motion and cardiac motion. The artefacts caused by periodic motion are still distributed among all directions, inducing the motion blurring and degrading the reconstruction image quality (75,108).

In this chapter, several motion compression techniques integrated into GRASP based reconstruction frameworks are introduced in detail. A relatively simple and effective motion correction algorithm has been proposed and directly integrated into the L+S decomposition model. A simulated phantom dataset and several clinic liver DCE-MRI datasets are implemented to certificate the merits of the proposed weighting algorithm.

### **7.1 Motion Subdivision in Extra Dimension GRASP**

In chapter 5, we have demonstrated that the k-space center was repeatedly acquired by stack-of-star golden angle sampling pattern. The PCA algorithm was implemented to extract respiratory motion signals from variation of the projection profile of objects (77). It is available to resort the spokes within each time frame according to the motion phase information.

Extra-dimension GRASP (XD-GRASP) introduces an additional motion dimension into the GRASP based framework (121). Each time frame is further subdivided into multiple motion states (typically 4 states) in XD-GRASP as shown in Figure 7-1. The AF is directly increased by the motion resolution. An Additional sparsity constraint is applied on motion dimension to explore the sparsity among different motion states. XD-GRASP reconstructs multiple motion states images within each time frame which compresses the motion blurring artefacts effectively and provides the additional motion phase information for clinical diagnosis.

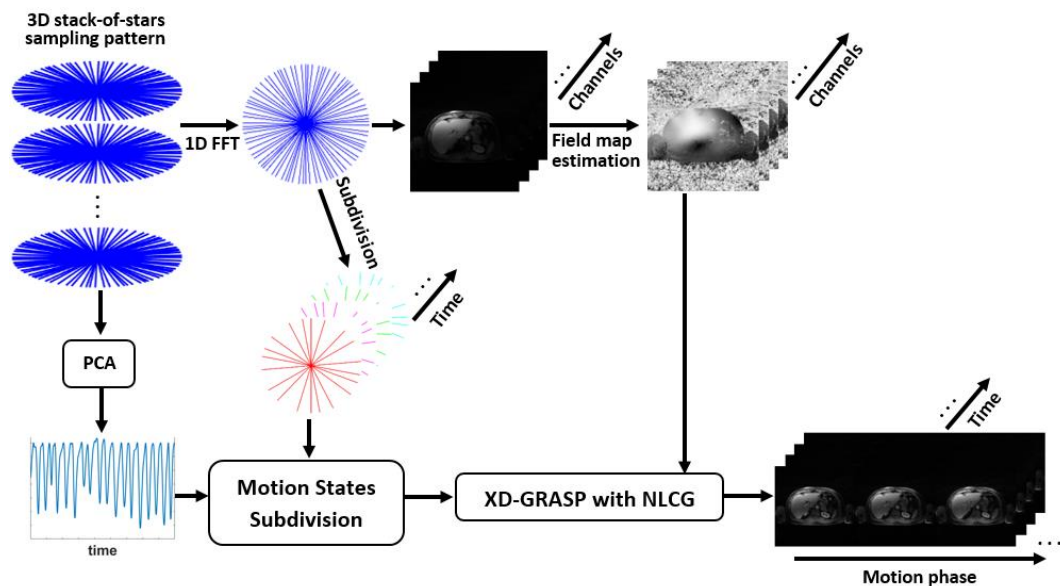


Figure 7-1: XD-GRASP reconstruction framework. The PCA algorithm is implemented to extract motion signals from repeatedly acquired k-space center along the slice dimension. The acquired spokes within time frames are resorted and subdivided into multiple motion states according to the extracted motion signal. An extra motion dimension is produced in XD-GRASP besides the temporal dimension. The XD-GRASP reconstruction with NLCG algorithm is then applied to recover the image series with multiple motion states by exploring the temporal sparsity among the time frames and motion sparsity among motion states.

The XD-GRASP reconstruction scheme is mathematically formulated as:

$$\operatorname{argmin}_x = \frac{1}{2} \|FCx - b\|_2^2 + \lambda_T \|T_1 x\|_1 + \lambda_m \|T_2 x\|_1 \quad (7.1)$$

where  $T_1$  and  $T_2$  are the TV sparsity transforms on temporal dimension and motion dimension respectively.  $\lambda_T$  and  $\lambda_m$  are the corresponding penalty factors for the sparsity constraints.

Nevertheless, the AF for reconstructed images is directly increased by the motion states resolution in XD-GRASP. Sufficient spokes are required in each time frame to avoid the failed reconstruction caused by excessive AF. Hence, the temporal resolution in XD-GRASP is degraded than that in standard GRASP to some extent. The computation burden caused by motion dimension significantly extends the reconstruction time which limits clinic applications of XD-GRASP.

## 7.2 Respiratory Weighted GRASP

Respiratory-Weighted GRASP (RACER-GRASP) (122,124) combines the respiratory weighting function, coil compression and coil-unstreaking to improve reconstruction efficiency and quality simultaneously. Similar to the XD-GRASP, RACER-GRASP subdivides the acquired spokes into multiple motion phases (typically 4 phases) according to the extracted motion signal besides the temporal subdivision. However, RACER-GRASP explores temporal sparsity of each motion state individually while there is no sparsity explored among the motion states. The reconstructed motion states are combined with different weighting factors in k-space as shown in Figure 7-2. A certain motion phase (typically end-expiration

phase) which is locked by weighting factors is reconstructed by RACER-GRASP (124). The excessive AF caused by motion subdivision is reduced by this delicate combination of motion states.

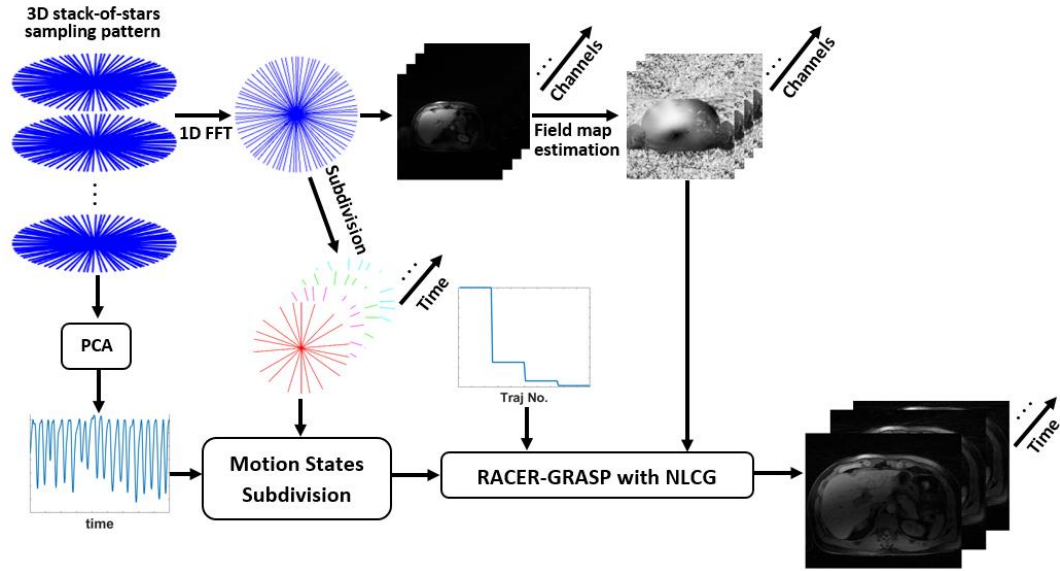


Figure 7-2: RACER-GRASP reconstruction framework. The PCA algorithm is implemented to extract motion signals from repeatedly acquired k-space center along slice dimension. The acquired spokes within time frames are resorted and subdivided into multiple motion phases according to the extracted motion signal. The RACER-GRASP reconstruction with NLCG algorithm is then applied to recover the image series with multiple motion states by exploring the temporal sparsity. An additional motion weighting matrix is implemented to control the contribution from different motion states and lock the desired motion phase during the iterative reconstruction.

The reconstruction framework of RACER-GRASP is similar to the standard GRASP and can be mathematically expressed as:

$$\operatorname{argmin}_x = \frac{1}{2} \|W(FCx - b)\|_2^2 + \lambda \|Tx\|_1 \quad (7.2)$$

where  $W$  indicates a respiratory weighting matrix calculated for k-space of each motion state. The value of weighting matrix elements is decayed exponentially from

the desired phase to other phases. Consequently, the contribution of k-space from desired phase and other motion phases is enhanced and compressed respectively for alleviating motion blurring. The design of weighting matrix is expressed as:

$$W(t) = b^{1-t}, \quad t \in [1, 4] \quad (7.3)$$

where  $b$  is a constant. To alleviate the computation burden caused by the additional motion phase loop, self-calibrating GRAPPA operator gridding (GROG) (125,126) is implemented to accelerate the RACER-GRASP reconstruction. Based on the acquired dataset, GROG trains the weighting factors for converting the non-Cartesian sampled k-space into conventional Cartesian based k-space. The repeated gridding/de-gridding steps are eliminated in RACER-GRASP by GROG. Therefore, an improved reconstruction efficiency is achieved by RACER-GRASP compared with standard GRASP and XD-GRASP (122).

Similar to XD-GRASP, RACER-GRASP requires sufficient spokes within time frames to support the additional motion subdivision. The temporal resolution is limited in RACER-GRASP. Only a certain motion phase was reconstructed in RACER-GRASP while additional motion state information is lost. Meanwhile, the GROG interpolation in RACER-GRASP relies on the training from acquired reference dataset. Unexpected convolutional artefact and SNR degradation are sometimes induced by GROG.

### 7.3 L+S Decomposition with Soft Weighting

Subdividing acquired spokes into multiple motion states is an effective method to compress motion blurring caused by respiratory or cardiac motion. However, the additional motion dimension loop significantly increases the computation burden and extends the overall reconstruction period. Here, we proposed a soft-weighting method for compressing motion blurring and maintaining the reconstruction efficiency simultaneously.

Similar to the RACER-GRASP, we created a respiratory weighting matrix to lock the certain motion phase during the reconstruction. There is no additional motion subdivision required in the proposed method, maintaining the reconstruction efficiency for all the frameworks. The spokes within each time frame are just resorted according to the extracted motion signal. We directly implemented a modified sigmoid function to control the contribution of spokes acquired at different motion phases. The modified sigmoid function is expressed as:

$$W(t) = \frac{1}{1 + e^{-t}} + c, \quad t \in [n_1 \ n_2] \quad (7.4)$$

where  $n_1$  and  $n_2$  are designed delicately to select the certain segmentation of sigmoid curve with the smooth but rapid transition between different respiratory phase bands.  $c$  is the DC component of the weighting function and it is typically designed with a small value. Hence, all the acquired spokes are involved in reconstruction to compress the undersampling artefacts while a certain respiratory phase is still locked.

For a fair comparison, we have converted the weighting function for multiple motion states in RACER-GRASP to the equivalent matrix for all spokes within the time frames. It is obvious that RACER-GRASP implemented a “stair-step” respiratory weighting function to maintain the contribution of spokes acquired at the expiration phase and compress the contribution of spokes acquired at other respiratory phases as shown in Figure 7-3. However, stair-step function works as the “hard bandpass” filter which introduces abrupt weighting factor variation among the acquired spokes while unexpected artefacts can be induced by this abrupt weighting truncation. According to the weighting matrix in Equation 7.3, RACER-GRASP can reconstruct the end-expiration and end-inspiration phases (edge motion phase) with less interference from other motion phases (122). Two inter-phases of respiratory still experience significant interference from the adjacent motion phases.

The modified sigmoid function achieves a smooth transition between the “passband” and “stopband”, alleviating the unexpected truncation artefacts. The single sigmoid function can be implemented to lock down the edge respiratory phases: end-inspiration phase and end-expiration phase. Availability of other respiratory phases is achieved by combining two modified sigmoid functions in opposite directions. Feasible respiratory phases are achieved by shifting the modified sigmoid function with a certain step-size. The minimum step-size is limited by the number of acquired spokes within each time frame and the motion state resolution.

The variation of imaging object within respiratory cycles is explored in detail by shifting a sigmoid based respiratory weighting curve with a small step-size as shown in Figure 7-3c. The soft weighting is introduced into the standard L+S

decomposition scheme to achieve high reconstruction efficiency and effective motion blurring compression simultaneously. The L+S with soft weighting reconstruction framework is shown in Figure 7-4.

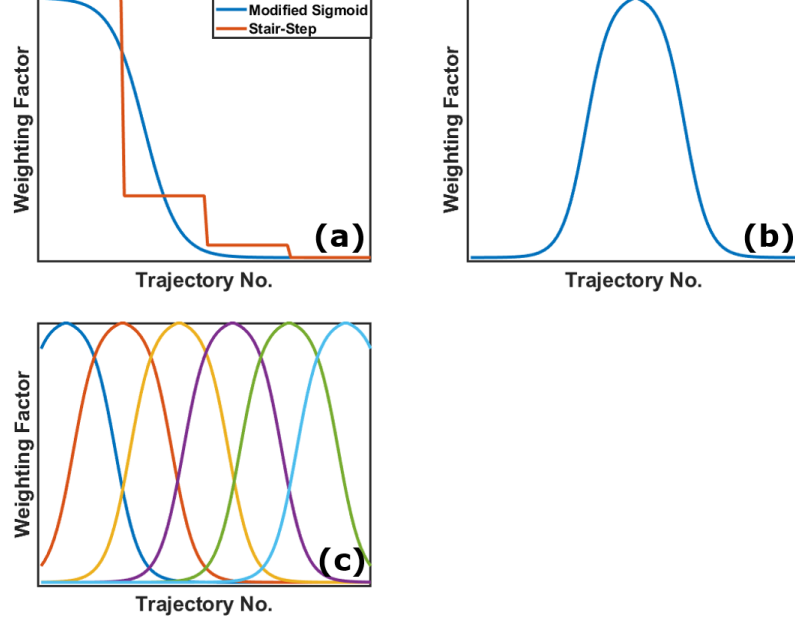


Figure 7-3: The design of soft weighting functions. (a) Stair-step weighting function used in RACER-GRASP and the proposed modified sigmoid function. (b) Combined sigmoid functions for other motion phases. (c) Shifting the proposed weighting function with a certain step-size for the reconstruction of different motion states.

The modified L+S with soft weighting scheme is mathematically expressed as:

$$\operatorname{argmin}_{L,S} = \frac{1}{2} \|W\{E(L+S) - d\}\|_2^2 + \lambda_L \|L\|_* + \lambda_T \|TS\|_1 \quad (7.5)$$

where  $W$  is the soft weighting matrix within each time frame.  $E$  is the multi-coil encoding operator and  $d$  is the acquired data.  $T$  is the temporal TV sparsity transform applied on sparse components  $S$ .  $\lambda_L$  and  $\lambda_T$  are two penalty factors which trade off the data consistency versus the complexity of solution given by the nuclear norm  $\|\cdot\|_*$  of low-rank components  $L$  and  $L_1$  norm  $\|\cdot\|_1$ .

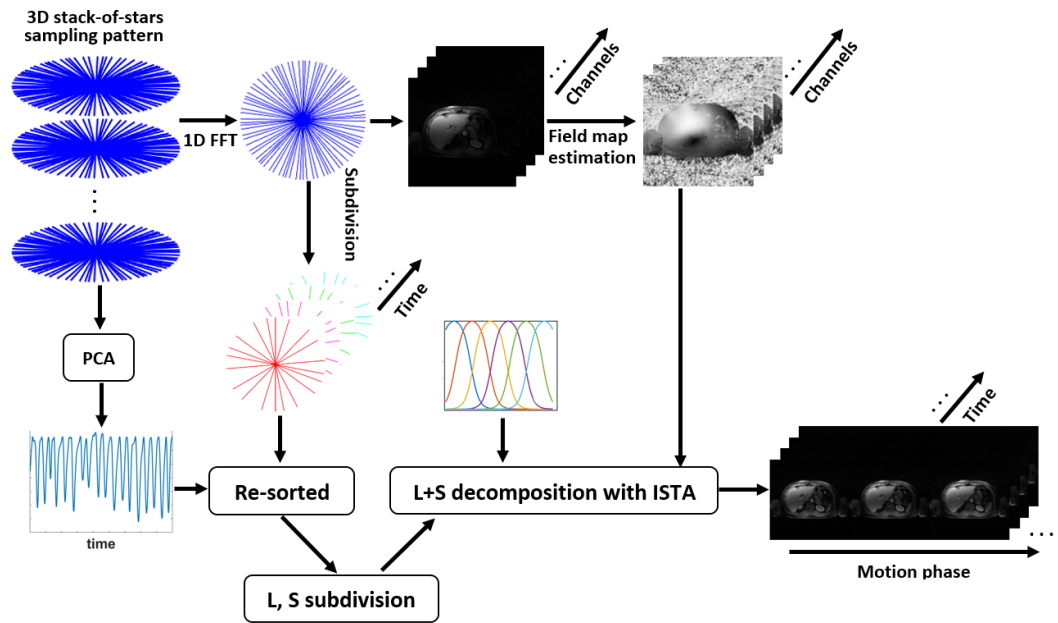


Figure 7-4: L+S with soft weighting reconstruction framework. The acquired spokes within time frames are resorted according to the extracted motion signal. A soft weighting matrix is implemented to control the contribution from spokes acquired at different motion phases and lock the desired motion phase during reconstruction. Feasible motion states can be reconstructed by shifting the weighting matrix.

## 7.4 Dynamic and Motion Simulation with Model Phantom

### 7.4.1 Phantom Simulation Design

A phantom model with dynamic intensity variation and periodic motion was created, producing a motion interfered DCE phantom dataset. One of the most significant benefits of this simulation framework is that the ground truth of motion is known exactly, enabling the accurate quantification of the performance of different motion compression methods.

To simulate the abdomen structure, a 2D Shepp-model model with a total of 768\*768 voxels was created with modified structures as shown in Figure 7-5. The

design of a large voxel matrix reduces the motion gap between adjacent motion states caused by discrete digital simulation. The phantom model was subdivided into two background sections and five dynamic sections. The gray level of two background sections was designed as 1 and 0.2 and kept constant during simulation. The signal intensity of dynamic sections was varied with a designed dynamic curve. Three dynamic sections were designed as the motion sections. Besides the variation of gray level, the position of these motion sections was rotated periodically, simulating the physical displacement caused by periodic respiratory motion.

A dynamic curve with 1100 discrete points between the pre-contrast phase and the arterial phase was created. The magnitude of dynamic curve ranges from 0 to 1. The virtual time gap between adjacent discrete points was designed as 0.143 s while the whole dynamic variation period was around 157 s. The arterial phase with peak signal intensity was arranged at the 230<sup>th</sup> point (32.9s) of the curve model. The signal intensity of dynamic sections was varied with the dynamic curve. Figure 7-6 shows three contrast phases of the computer model at the same motion state.

The in-plane simulation was simulated. Corresponding to the dynamic curve model, a sinusoid motion curve with 1100 discrete points was created. The virtual time gap of motion curve was the same as dynamic curve model. 48 respiratory cycles were included in the motion curve, simulating the respiratory at the rate of 18.3 cycles/minutes. A total of 81 motion states were created between inspiration and expiration, offering high motion resolution during simulation. The motion sections were gradually rotated by the motion curve with a step-degree  $0.37^\circ$ . The rotation angles of motion sections were uniformly distributed over an interval of  $[-15^\circ, +15^\circ]$ .

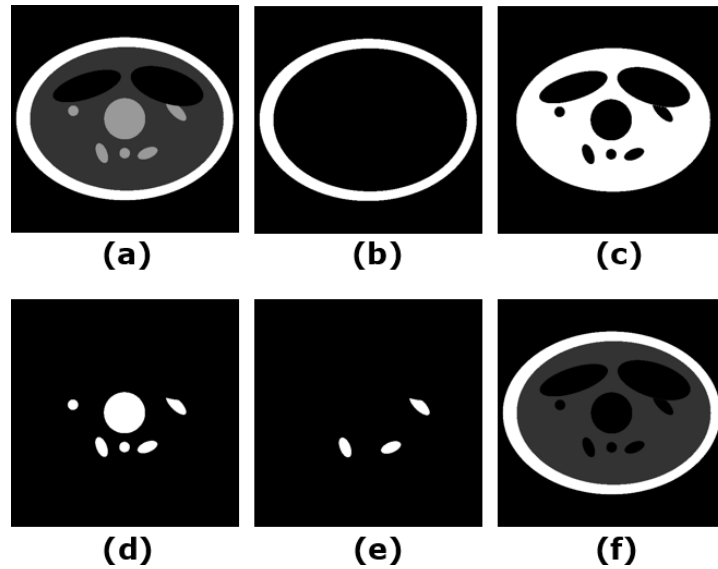


Figure 7-5: (a) A Shepp-logan computer model with modified internal structure. (b)~(c) Two background sections, the signal intensity of these sections was kept constant as 1 and 0.2 respectively. (d) Six dynamic sections of computer model, the signal intensity of these sections were varied by the dynamic curve. (e) Three motion sections of computer model, both the signal intensity and position of motion sections were varied. (f) The ultimate computer model before contrast enhancement.

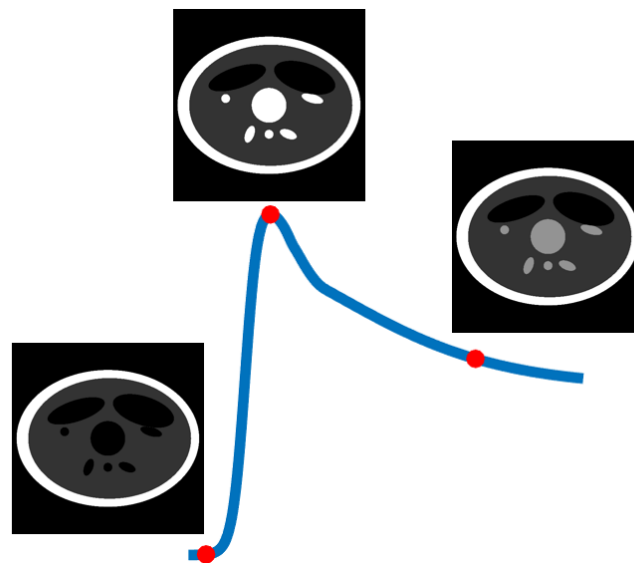


Figure 7-6: Three representative contrast phases of modified Shepp-logan model at the same motion state. The signal intensity of six dynamic sections were varied by a dynamic curve model with a total of 1100 discrete points. The maximum dynamic signal occurs at 230<sup>th</sup> point, forming central arterial phase.

Figure 7-7 shows the phantom model structure at 4 representative motion states before contrast enhancement. The data was simulated with golden angle radial sampling pattern. The dynamic phase and motion phase of phantom model were varied simultaneously and continuously on the temporal dimension. The phantom stages at each discrete time point were recorded. A total of 1100 phantom series with the matrix size 512\*512 (central region) were recorded as the reference.

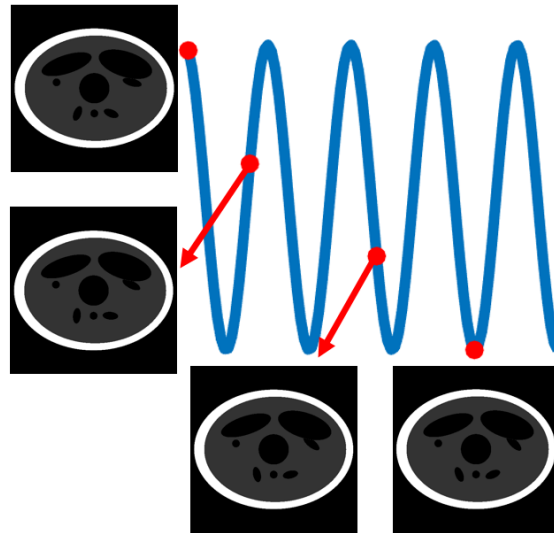


Figure 7-7: 4 representative motion states of computer model before the dynamic contrast simulation. The motion sections were gradually rotated by the motion curve with a step-degree  $0.37^\circ$ . The rotation angle motion sections ranged from  $-15^\circ$  to  $15^\circ$ .

A certain radial spoke with 768 sample points was acquired at each discrete time point. Oversampling along readout was implemented to reduce readout aliasing and gridding artefacts. Eight exponentially decayed field maps were integrated into the model before data acquisition. The ultimately acquired dataset contains 8 channels, a total of 1100 spokes with 784 readout points in each spoke. An averaging image was directly reconstructed by NUFFT to estimate the field maps.

## 7.4.2 Experiment Design

The simulated phantom dataset with dynamic contrast variation and the periodic motion was subdivided into 11 frames with the temporal resolution of 100 spokes/frame (14.3s/frame). The image series were reconstructed with a matrix size of  $512 \times 512 \times 11$  by NUFTT, GRASP and L+S decomposition respectively. According to the Nyquist sampling standard, the corresponding AF is 8. The reconstructions with standard GRASP and L+S decomposition were implemented to quantify the level of blurring artefact caused by periodic motion.

The same penalty factor  $\lambda_T$  of temporal TV was assigned in both GRASP and L+S decomposition for a fair comparison. A variety of values of  $\lambda_T$  ranging from  $0.1 * M_S$  to  $0.5 * M_S$  (step-size 0.05) has been experimented while an adequate value  $\lambda_T = 0.4 * M_S$  was adopted according to the evaluation of two experienced radiologists. Other reconstruction parameters setups were carefully followed. The number of iteration was set as 60 for both NLCG in GRASP and ISTA in L+S decomposition.

Additional reconstructions were performed with three motion corrected frameworks including XD-GRASP, RACER-GRASP (without GROG acceleration) and L+S decomposition with soft weighting. The source codes of GRASP, XD-GRASP, RACER-GRASP and L+S decomposition were downloaded from the authors' websites (108,113,121,122). Their reconstruction parameters setups were carefully followed. The spokes in time frames were resorted according to the designed motion signal model. Additional 4 motion states were subdivided within each time frame

with the motion state resolution 25 spokes/state for both XD-GRASP and RACER-GRASP.

The penalty factor  $\lambda_T$  was still set as  $0.4 * M_s$  in these three motion corrected reconstruction schemes for a fair comparison. Additional penalty factor  $\lambda_m$  on motion dimension in XD-GRASP was set as  $0.5 * \lambda_T$ , following the same setup of source code (121). 4 motion states were reconstructed simultaneously while a total of 44 images were reconstructed with the matrix size 512\*512 in XD-GRASP.

RACER-GRASP combines 4 motion states with different weighting factors as the output while only 11 frames were reconstructed at the end-inspiration phase with the matrix size 512\*512 in RACER-GRASP. To quantify the computation burden caused by additional motion subdivision, GROG algorithm was not implemented here for acceleration. The number of iteration was kept the same as 60 for NLCG in both XD-GRASP and RACER-GRASP.

L+S with soft weighting followed the same setup as the standard L+S decomposition. A modified sigmoid weighting function was integrated into the model to control the contribution of 100 spokes within each time frame. The end-expiration motion phase was locked by the weighting function. 11 frames were reconstructed with the matrix size 512\*512 in L+S with soft weighting.

### **7.4.3 Simulation Results & Analysis**

The gray level of image series reconstructed by different schemes was normalized based on the mean value of background sections. All the reconstructions were

performed using MATLAB 2020b (MathWorks, MA) on an Intel Core i7-4790 PC with a 3.6 GHz processor and repeated 10 times.

Figure 7-8 shows a comparison of conventional NUFFT reconstruction to standard GRASP and L+S decomposition without motion compression. Due to the decrease of the AF, the image quality of NUFFT reconstruction is better than that of NUFFT reconstruction at AF=22 in the previous chapter. Fewer undersampling artefacts were observed in NUFFT than before. Both standard GRASP and L+S decomposition compressed the streaking artefacts caused by undersampling effectively. There was no ghost motion artefact obtained in reconstructed series.

All three reconstruction schemes showed the motion averaging effect. Significant blurring was obtained in the motion sections, corresponding to the averaging effect of the acquisition window in radial sampling. No obvious dynamic enhancement was obtained in the pre-contrast phase in GRASP and L+S decomposition. The peak of dynamic signal in arterial phase was visually degraded compared to the reference, certifying the existence of temporal averaging effect in these two frameworks.

The mean reconstruction period for GRASP and L+S decomposition is 1018.9 s and 273.2 s respectively. Due to the increase of iteration number and data size, the reconstruction period of two schemes was increased. A much longer period is required by GRASP to complete the iterative reconstruction.

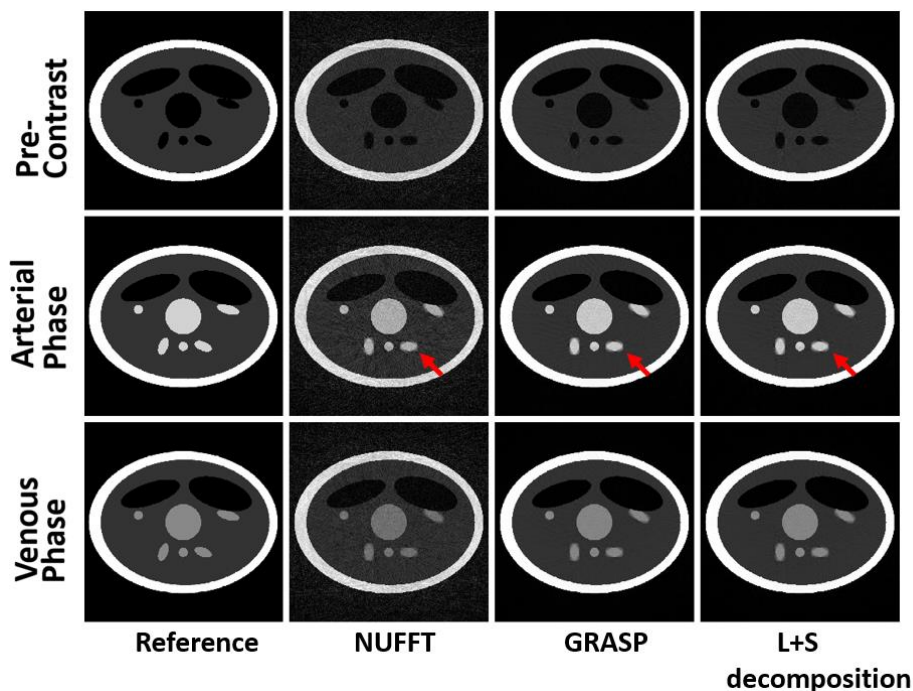


Figure 7-8: A comparison of reference at end-expiration stage to three reconstruction schemes without motion correction in three representative phase contrast in phantom dataset. Significant motion blurring was observed in NUFFT, GRASP and L+S decomposition. GRASP and L+S compressed the undersampling streaking artefacts effectively.

Figure 7-9 shows a comparison of reference to XD-GRASP, RACER-GRASP and L+S with soft weighting reconstruction schemes in the three representative phases of phantom model at end-expiration phase. All three motion corrected reconstruction schemes compressed streaking artefacts and locked the end-expiration phase accurately.

No significant motion blurring was obtained in XD-GRASP and RACER-GRASP. Due to the excessive AF in XD-GRASP (AF=32 for each motion state image), the SNR of XD-GRASP images was typically lower than the other two schemes while some streaking artefacts remained at the edge sides of phantom model in XD-GRASP. RACER-GRASP showed improved image quality than XD-GRASP.

Some blurring was observed on the edge side of motion sections in RACER-GRASP. The edge side blurring was alleviated further in proposed L+S with soft weighting.

Similar to the GRASP and L+S decomposition, the peak dynamic signal in arterial phase was degraded visually in XD-GRASP, RACER-GRASP and L+S with soft weighting. However, significant dynamic enhancement was obtained in pre-contrast phase in three motion corrected frameworks, showing the worse dynamic performance.

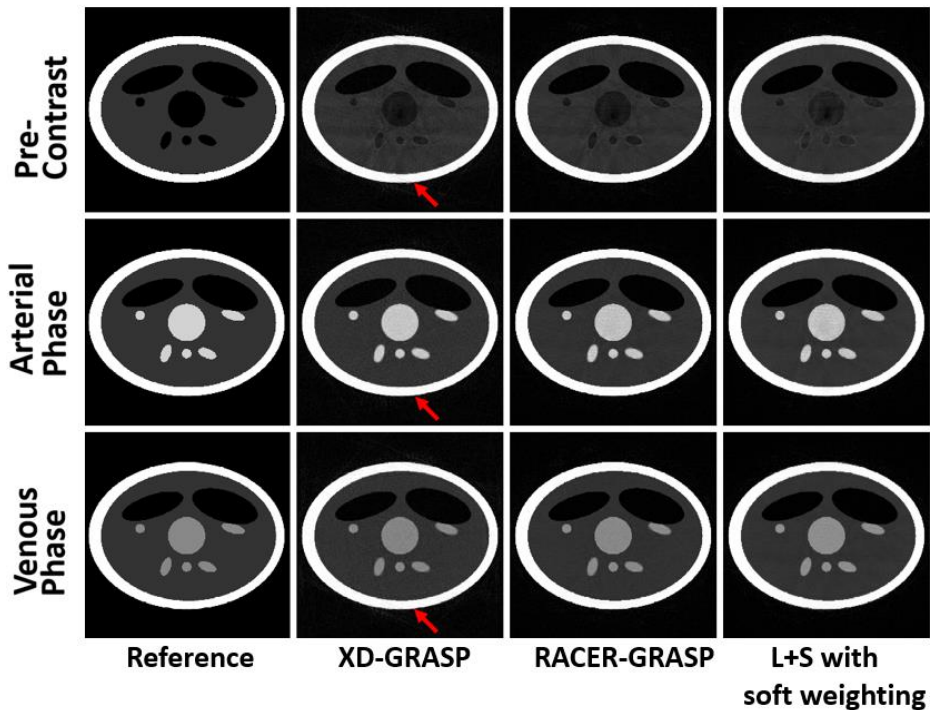


Figure 7-9: A comparison of reference at end-expiration stage to three reconstruction schemes with motion correction in three representative phase contrast in the phantom dataset. All the image series were reconstructed at AF= 8 and 100 spokes/frame. All three reconstruction schemes compressed motion blurring effectively. Some streaking artefacts remained in XD-GRASP. Better image quality was achieved in RACER-GRASP and the proposed method.

The mean reconstruction time for these three motion corrected reconstruction frameworks is 2661.7 s, 1847.3 s and 275.3 s relatively. It is obvious that additional motion subdivision significantly degrades the reconstruction efficiency in XD-GRASP and RACER-GRASP. XD-GRASP contains additional motion states reconstruction which requires more time to complete iteration than the RACER-GRASP. A similar reconstruction efficiency was obtained between L+S decomposition and L+S with soft weighting. Soft weighting results in negligible computation cost in the L+S based framework, preserving its reconstruction efficiency.

Figure 7-10 shows a zoomed view of a certain motion section (at end expiration) in reference and five different reconstruction frameworks in venous phase. The error maps between reference and reconstruction schemes were calculated and displayed. The proposed L+S with soft-weighting displayed much less difference to the ground truth compared with other reconstruction schemes. Using the selected motion section in reference as the benchmark, the RMSE value of GRASP, L+S, XD-GRASP and RACER-GRASP was 0.038, 0.037, 0.033 and 0.024 respectively.

Similar RMSE values were obtained between L+S decomposition and GRASP as they experienced the same level of motion blurring. The RMSE was not decreased as expected in XD-GRASP which may be interfered by low SNR. A significant decrease of RMSE was obtained RACER-GRASP, certifying the effective motion compression. The RMSE value of L+S with soft weighting was 0.02 which is much smaller than the other 4 schemes, suggesting that our method can capture the motion phase and compress motion blurring artefacts much better.

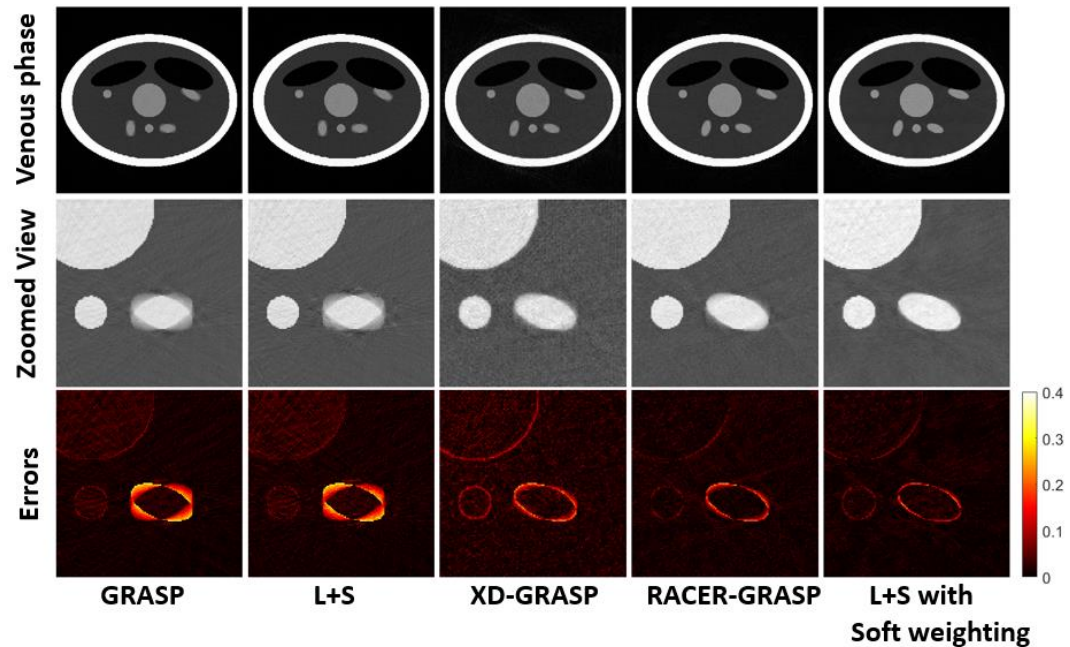


Figure 7-10: A comparison of GRASP, L+S decomposition, RACER-GRASP and L+S with soft weighting in venous phase at end-expiration stage. Three rows of images series corresponding to the venous phase image, zoomed view of a motion section in venous phase and the error maps in these five different reconstruction schemes. Significant motion errors were obtained in GRASP and L+S decomposition. L+S with soft weighting shows the least residual motion artefacts.

Figure 7-11a and Figure 7-11b show the dynamic signal variation of three GRASP based techniques and two L+S decomposition based techniques respectively. GRASP and L+S decomposition showed similar dynamic performance. Compared to the ground truth of dynamic curve model, the peak dynamic signal was degraded by around 17.3% in GRASP and 17.4% in L+S decomposition. Dynamic degradation is enhanced in motion corrected GRASP techniques. The peak of dynamic signal was degraded by 28.5% and 33.3% in XD-GRASP and RACER-GRASP respectively. A similar tendency was found in the L+S based techniques. The peak dynamic signal was degraded by 36.4% in L+S with soft weighting. The temporal averaging was improved unexpectedly by the motion correction methods.

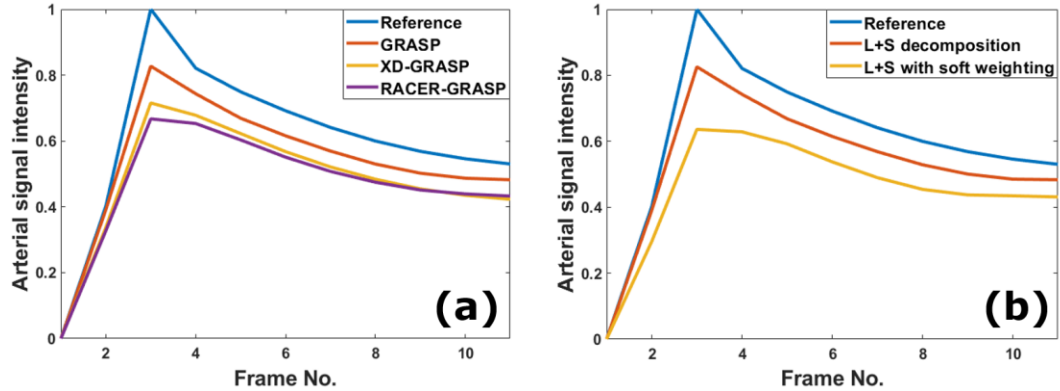


Figure 7-11: (a) Dynamic signal variation for the simulated phantom using reference, GRASP, XD-GRASP and RACER-GRASP. Two motion corrected GRASP techniques experienced more dynamic degradation than the standard GRASP. (b) Dynamic signal variation for the simulated phantom by using reference, L+S and L+S with soft weighting. A similar tendency about dynamic degradation was obtained in motion corrected L+S technique. L+S with soft weighting experienced more dynamic degradation than standard L+S decomposition.

## 7.5 L+S with Soft Weighting and Joint Sparsity

The motion subdivision or motion weighting can compress the motion artefacts effectively at the expense of increasing temporal blurring. Both these two motion correction methods theoretically amplify the contribution of temporal TV constraint in GRASP based and L+S based frameworks. The temporal blurring effect is increased which leads to further degradation of dynamic contrast.

It is available to introduce both the soft weighting and additional sparsity constraint into the L+S decomposition together, compressing motion blurring and recovering the dynamic contrast simultaneously. The reconstruction framework of the proposed L+S with soft weighting and joint sparsity is shown in Figure 7-12.

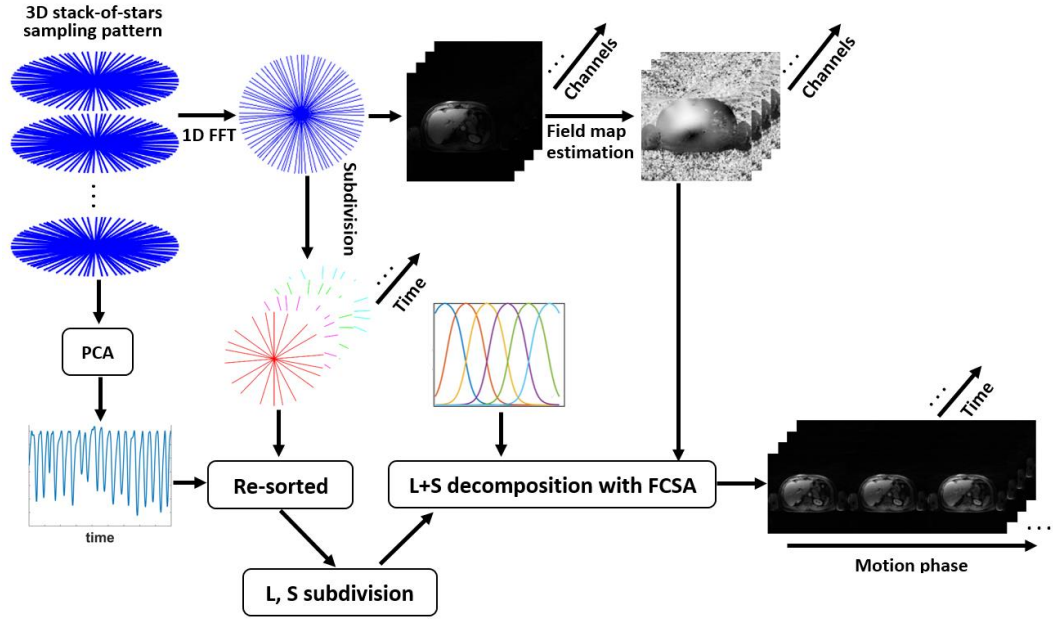


Figure 7-12: L+S with soft weighting and joint sparsity reconstruction framework. The acquired spokes within time frames are resorted according to the extracted motion signal. A soft weighting matrix is implemented to control the contribution from spokes acquired at different motion phases and lock the desired motion phase during reconstruction. FCSA is implemented to solve the optimization problem with joint sparsity constraints. Feasible motion states can be reconstructed by shifting the weighting matrix.

The proposed L+S with soft weighting and joint sparsity scheme is mathematically formulated as:

$$\operatorname{argmin}_{L,S} = \frac{1}{2} \|W\{E(L + S) - d\}\|_2^2 + \lambda_L \|L\|_* + \lambda_T \|TS\|_1 + \lambda_F \|FS\|_1 \quad (7.6)$$

where  $E$  is the multi-coil encoding operator and  $d$  is the acquired data.  $T$  and  $F$  present the temporal TV and temporal FFT sparsity transforms applied on the sparse component  $S$ .  $\lambda_L$ ,  $\lambda_T$  and  $\lambda_F$  are three penalty factors applied on the sparsity constraints which trades off the data consistency versus the complexity of solution given by the nuclear norm  $\|\cdot\|_*$  of low-rank components  $L$  and  $L_1$  norm  $\|\cdot\|_1$ .

The same experiment assignment was implemented in L+S with soft weighting and joint sparsity. A total of 11 time frames with the same temporal resolution 100 spokes/frame was reconstructed by the proposed method with the matrix size of 512\*512. Besides the additional temporal FFT sparsity constraint, all of the parameters in the proposed method were kept the same as L+S with soft weighting in chapter 7.4. The optimization problem in L+S with soft weighting and joint sparsity was solved by FCSA with a total of 60 iterations (the same as other schemes). The penalty factor  $\lambda_F$  followed the same value in chapter 6.5.

## **7.6 Simulation Results & Analysis**

Figure 7-13 shows a comparison of reference to XD-GRASP, RACER-GRASP, L+S with soft weighting and L+S with soft weighting and joint sparsity in the three representative phases of phantom model at end-expiration phase. Additional joint sparsity in the proposed method did not interfere the motion compression from the soft weighting. The end-expiration was accurately locked and there was no obvious motion blurring obtained in the proposed method. In arterial phase, the signal intensity in dynamic sections in the proposed method was much better than the other three reconstruction schemes. Temporal FFT still shows robustness of alleviating temporal blurring and recovering the dynamic contrast in the proposed method.

Figure 7-14 shows a zoomed view of a certain motion section (at end expiration) in four motion corrected schemes in venous phase. The difference maps between reference and reconstruction schemes were calculated and displayed. The proposed method showed a similar difference map to the L+S with soft weighting and is much better than the XD-GRASP and RACER-GRASP.

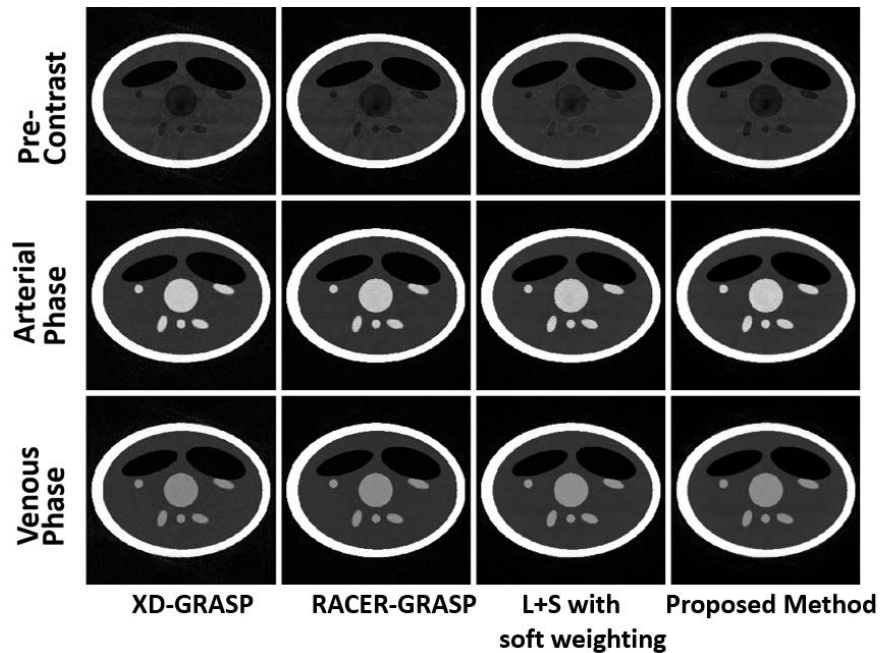


Figure 7-13: A comparison of four different motion correction schemes in three representative phase contrast in phantom dataset. All the image series were reconstructed at AF= 8 and 100 spokes/frame. All schemes reconstructed the end-expiration phase accurately. The improved dynamic signal was obtained in arterial phase in the proposed method.

The errors at the edge of the motion section in the proposed method were slightly increased while the residual motion artefacts in the background section were compressed further in the proposed method. The RMSE value in both L+S with soft weighting and L+S with soft weighting and joint sparsity is 0.02 which is much smaller than XD-GRASP and RACER-GRASP, showing the robustness of soft weighting. The performance of soft weighting was not degraded by joint sparsity in the proposed method.

Figure 7-15 and Table 7-1 show the dynamic signal variation of four motion corrected schemes. The best dynamic contrast was achieved by L+S with soft weighting and joint sparsity method. The peak dynamic signal in phantom dataset

in the proposed method demonstrated an increase in peak DCE signal by 14.6% and 9.3% than that of L+S with soft weighting and RACER-GRASP respectively.

Compared with L+S with soft weighting, significantly dynamic improvement was achieved in the proposed method by the joint sparsity. Similar dynamic contrast was obtained between XD-GRASP and the proposed method. The peak dynamic signal in proposed method increased by only 1.9% than that in XD-GRASP. However, compared with XD-GRASP, there was no obvious SNR degradation and residual artefact obtained in the proposed method.

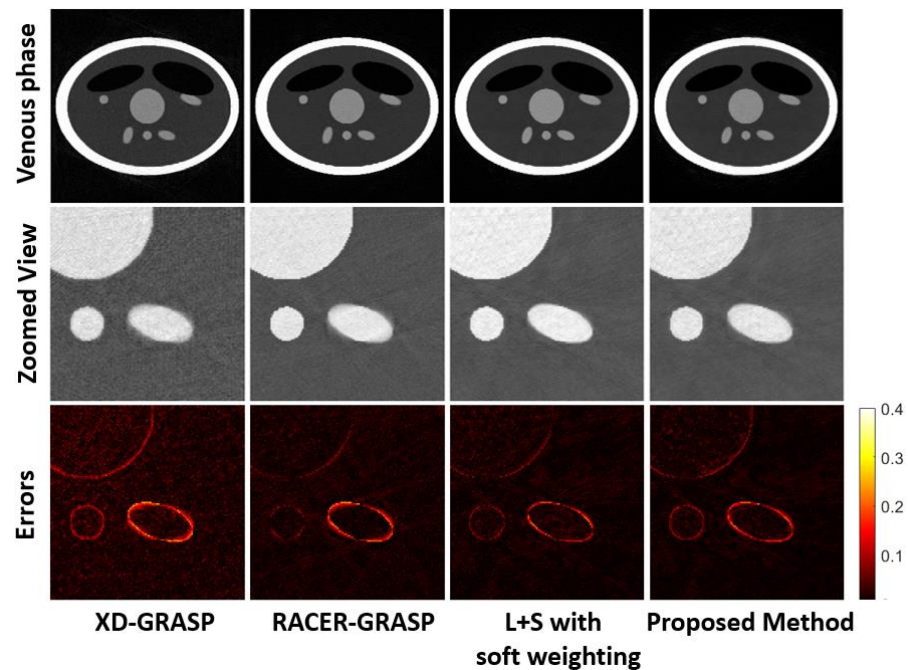


Figure 7-14: A comparison of four reconstruction schemes in venous phase at end-expiration stage. Three rows of image series corresponding to the venous phase image, zoomed view of motion section in venous phase and the error map in these 5 different reconstruction schemes. L+S with soft weighting and L+S with soft weighting and joint sparsity showed much fewer residual motion errors compared with XD-GRASP and RACER-GRASP.

Table 7-1: Reconstruction time, Peak DCE signal and Mean DCE signal of different reconstruction schemes in the simulated phantom data. Improved dynamic contrast, better motion correction and high reconstruction efficiency were obtained in the proposed method

Reconstruction Scheme	RMSE	Reconstruction Time	Peak DCE signal	Mean DCE signal
Ground Truth	-	-	1	0.5995
GRASP	0.037	1018.9s	0.8272	0.5288
XD-GRASP	0.033	2661.7s	0.7154	0.4762
RACER-GRASP (without GROG )	0.024	1847.3s	0.6672	0.4643
L+S decomposition	0.038	273.2s	0.8258	0.4489
L+S with soft weighting	0.020	275.3s	0.6362	0.5280
Proposed method	0.020	276s	0.7292	0.4811

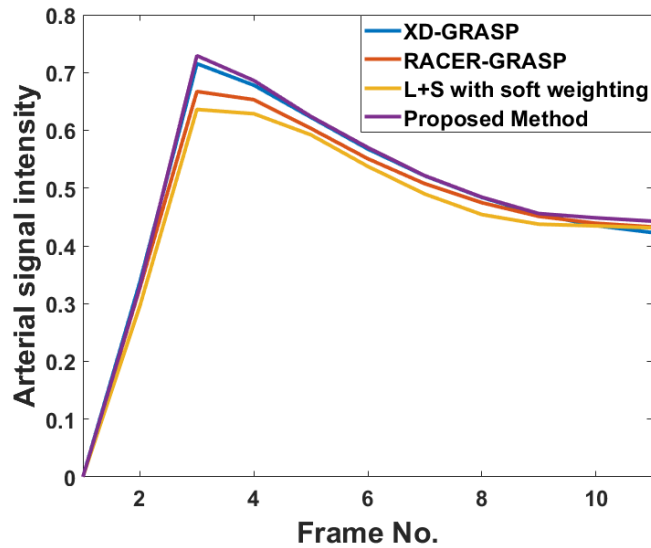


Figure 7-15: Dynamic signal variation for the simulated phantom using XD-GRASP, RACER-GRASP, L+S with soft weighting and proposed L+S with soft weighting and joint sparsity. Best dynamic contrast was achieved by the proposed method. The peak dynamic signal of the proposed method is a little bit higher than XD-GRASP and much higher than L+S with soft weighting and RACER-GRASP

Meanwhile, the overall reconstruction period of the proposed method was 276 s which is almost the same as the period in standard L+S decomposition and L+S with soft weighting. The reconstruction efficiency of the proposed L+S with soft weighting and joint sparsity is still much higher than GRASP based techniques.

## **7.7 Clinic Dataset and Reconstruction**

Two liver DCE-MRI datasets provided by Lifeng Research group were implemented to evaluate the dynamic performance and motion compression of different reconstruction schemes (108,121). The datasets were acquired with the same protocol and scanners as mentioned in chapter 6.6. An intravenous injection of 10 ml of Gd-DTPA (Magnevist, Bayer Healthcare, Leverkusen) followed by a 20 ml saline flush was initiated accompany with the data acquisition simultaneously. The injection rate for both contrast agents was 2 ml/second.

The corresponding parameters for the liver DCE-MRI dataset included: TR/TE=3.52 ms/1.41 ms, FOV = 360\*360\*240 mm<sup>3</sup>, number of partitions = 80, with 60% slice resolution reduction and 6/8 partial Fourier applied along the slice dimension. The dataset contains 8 channels, 1100 spokes with 512 readout points each. Oversampling along the readout direction was implemented to avoid readout aliasing and gridding artefacts caused by NUFFT. The central 384 data points on each spokes were remained. To reduce the computation burden and further alleviate streaking artefact, the 2D liver dataset was processed by coil unstacking and coil compression prior to the reconstruction. The dataset was compressed from 384\*1100\*12 to 384\*1100\*8.

Following the same temporal subdivision in phantom dataset, the liver dataset was subdivided into 11 frames between the pre-contrast phase and the arterial phase with the temporal resolution of 100 spokes/frame ( $\sim 15s/$  frame). The corresponding acceleration ratio is  $AF=6$ . PCA algorithm was implemented to extract respiratory motion signals from repeatedly acquired k-space center along the slice encoding direction. The spokes in time frames were resorted from the end-expiration phase to the end-inspiration phase according to the extracted respiratory signal.

Image series were reconstructed using NUFFT, XD-GRASP, RACER-GRASP with GROG, L+S with soft weighting and L+S with soft weighting and joint sparsity. 4 motion states were subdivided within each time frame with the motion state resolution 25 spokes/state for both XD-GRASP and RACER-GRASP.

The basic reconstruction parameters of GRASP based techniques and L+S decomposition based techniques followed the same setup of source code. The penalty factor for  $\lambda_T$  with an adequate value was selected by two experienced radiologists. The same sigmoid based weighting matrix was implemented in standard L+S with soft weighing and L+S with soft weighting and joint sparsity. The value of  $\lambda_F$  following the same setup in previous phantom experiments in chapter 6. The iteration number for all of the reconstruction schemes was set as 20. All the reconstructions were repeated 10 times while the averaging iteration period was used as the standard to evaluate their reconstruction efficiency.

All of the time frames were reconstructed with the matrix size of  $384*384$ . The average signal intensity in arterial region was regarded as the standard to evaluate the dynamic performance of different reconstruction schemes. Furthermore,

additional reconstructions for RACER-GRASP and L+S with soft weighting and joint sparsity were performed at temporal resolution 96 spokes/frame, 64 spokes/frame and 32 spokes/frame, certifying the robustness of the proposed method at highly undersampled reconstruction. All the reconstructions were performed using MATLAB 2020b (MathWorks, MA) on an Intel Core i7-4790 PC with a 3.6 GHz processor and repeated 10 times.

## 7.8 Image Analysis and Statistics

A comparison of different reconstruction schemes in three representative contrast phases in a liver DCE-MRI dataset at AF=6 (100 spokes/frame) is shown in Figure 7-16. Respiratory motion was compensated in XD-GRASP, RACER-GRASP, L+S with soft weighting and L+S with soft weighting and joint sparsity. End-expiration phase images were selected from these four schemes.

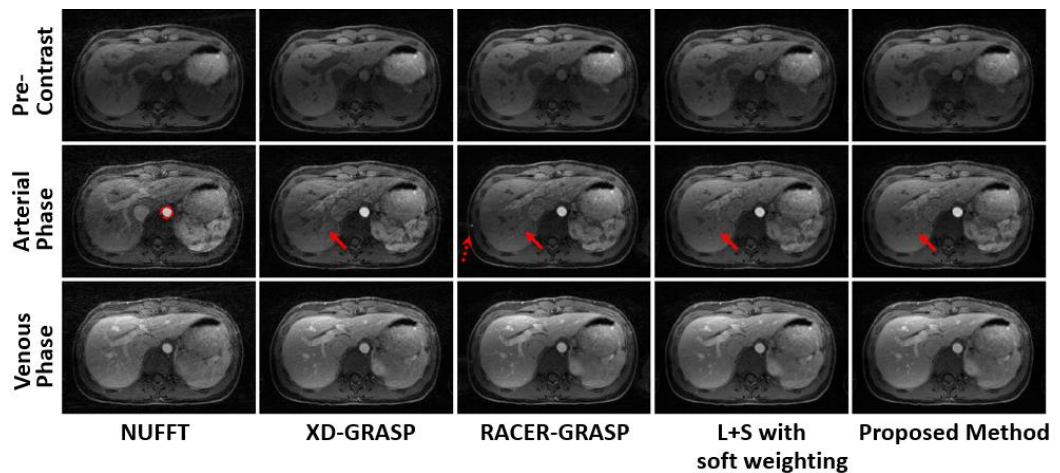


Figure 7-16: A comparison of different reconstruction schemes in three representative phases in a free-breathing liver DCE-MRI dataset. The reconstruction period for XD-GRASP, RACER-GRASP with GROG, L+S with soft weighting and the proposed method is 560.5s, 106s, 58.3s and 59.4s respectively. RACER-GRASP contains unexpected convolution artefacts (dashed arrow). The proposed method achieved the best dynamic tissue contrast and motion compression.

XD-GRASP and RACER-GRASP compressed motion blurring successfully by employing motion subdivisions. Residual streaking artefacts (labelled by solid arrow) and unexpected convolutional artefacts (labelled by dashed arrow) were obtained in XD-GRASP and RACER-GRASP respectively. Better motion correction and dynamic contrast were observed in the proposed method.

Figure 7-17 shows a zoomed view of the liver section in three representative phases in XD-GRASP, RACER-GRASP and the proposed method. It is obvious that some motion artefacts remained in the arterial phase in XD-GRASP. Less motion blurring was observed in RACER-GRASP. Best tissue detail was observed in L+S with soft weighting and joint sparsity, especially in arterial phase.

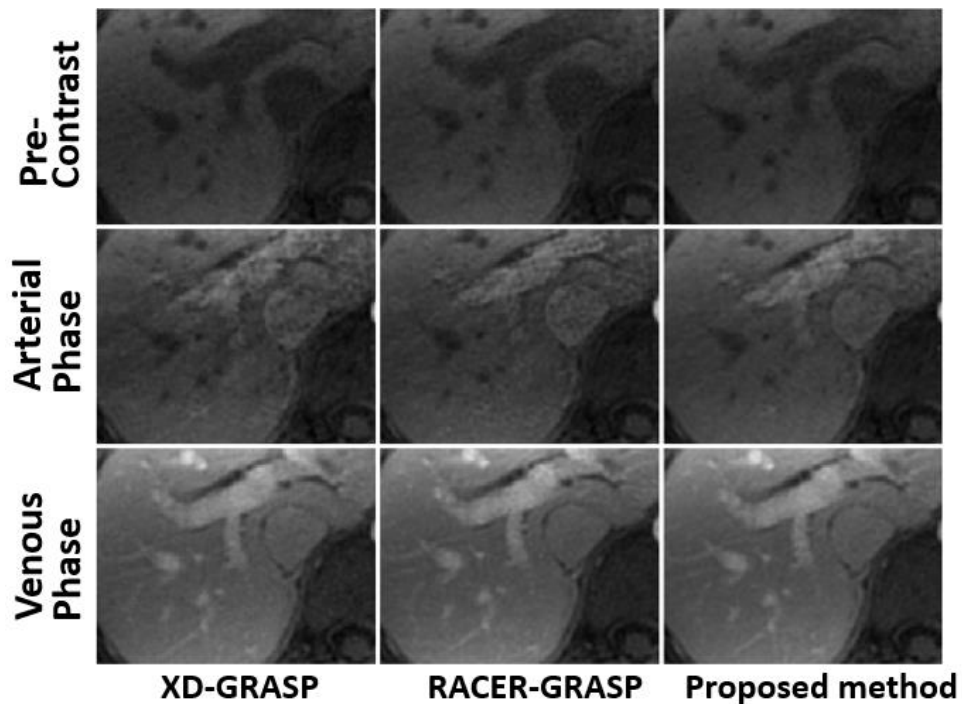


Figure 7-17: A further comparison of XD-GRASP, RACER-GRASP and the proposed L+S with soft weighting and joint sparsity reconstruction schemes in three representative phases with respiratory motion in zoomed view of liver section. Best tissue detail and dynamic contrast were observed in L+S with soft weighting and joint sparsity, especially in arterial phase.

Due to the decrease of the time frame number, the reconstruction period of all frameworks was reduced. The average reconstruction period for XD-GRASP, RACER-GRASP, L+S with soft weighting and L+S with soft weighting and joint sparsity is 560.5 s, 106 s, 58.3 s and 59.4 s respectively. With the support of GROG acceleration, RACER-GRASP presents much higher reconstruction efficiency than the XD-GRASP but GROG also induced convolutional artefacts in RACER-GRASP. The proposed method still shows the highest reconstruction efficiency without the need of GROG acceleration. The computation cost from motion compression and additional joint sparsity was minimized by the soft weighting method and FCSA respectively.

The dynamic contrast in the selected arterial region in XD-GRASP, RACER-GRASP, L+S with soft weighting and the proposed method is shown in Figure 7-18. The peak dynamic signal in liver dataset in the proposed method demonstrated an increase in peak DCE signal by 7.8%, 23.1% and 20% than that of XD-GRASP, RACER-GRASP and L+S with soft weighting respectively. The improved dynamic contrast enables better vessel structures and image quality in the proposed method.

Figure 7-19 shows a comparison of XD-GRASP and L+S with soft weighting and joint sparsity in 4 motion states from inspiration and expiration in venous contrast phase in the liver DCE-MRI dataset. The reduced streaking artefact and better tissue details were observed in the L+S with soft weighting and joint sparsity. The fidelity of feasible motion states reconstruction achieved by shifting modified sigmoid function was certificated further.

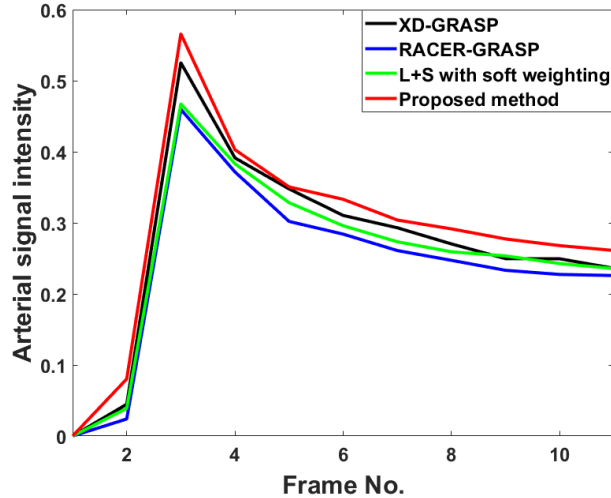


Figure 7-18: Dynamic signal variation among time frames in the arterial region in different reconstruction schemes. The peak dynamic signal in liver dataset in the proposed method demonstrated an increase in peak DCE signal by 7.8%, 23.1% and 20% than that of XD-GRASP, RACER-GRASP and L+S with soft weighting respectively.

Figure 7-20 shows an additional reconstruction of the proposed method with 12 motion states between inspiration and expiration. The image series reconstructed at high motion resolution explored the variation of liver tissues caused by respiratory motion in detail. The clear display of tissues variation within a respiratory cycle may provide potential information for the diagnosis of some diseases related to the respiratory. The further comparison between RACER-GRASP and L+S with soft weighting joint sparsity at temporal resolution 96 spokes/frame, 64 spokes/frame and 32 spokes/frame in liver dataset is shown in Figure 7-21. Less image quality degradation was observed in the proposed method with the increase of temporal resolution, demonstrating the robustness of soft weighting for motion compression at highly undersampled reconstruction again. Additional sparsity also successfully recovered the dynamic contrast of image series reconstructed at different AF. The better dynamic contrast was maintained in the proposed method.

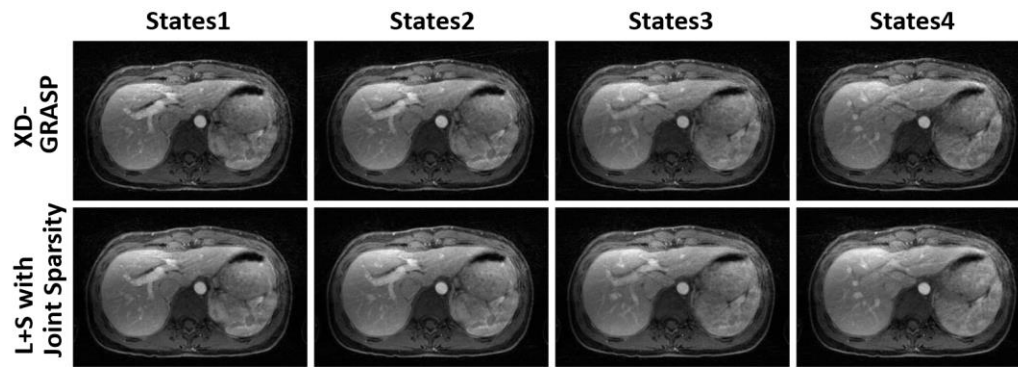


Figure 7-19: A comparison of XD-GRASP and L+S with soft weighting and joint sparsity for multiple motion states reconstruction in venous phase in liver DCE-MRI dataset with temporal resolution 100 spokes/frame. The structures in 4 motion states from inspiration to expiration in two reconstruction schemes were matched which certificated the fidelity of multiple motion states reconstruction through shifting weighting function. The better tissue details and improved image quality were achieved by our method.

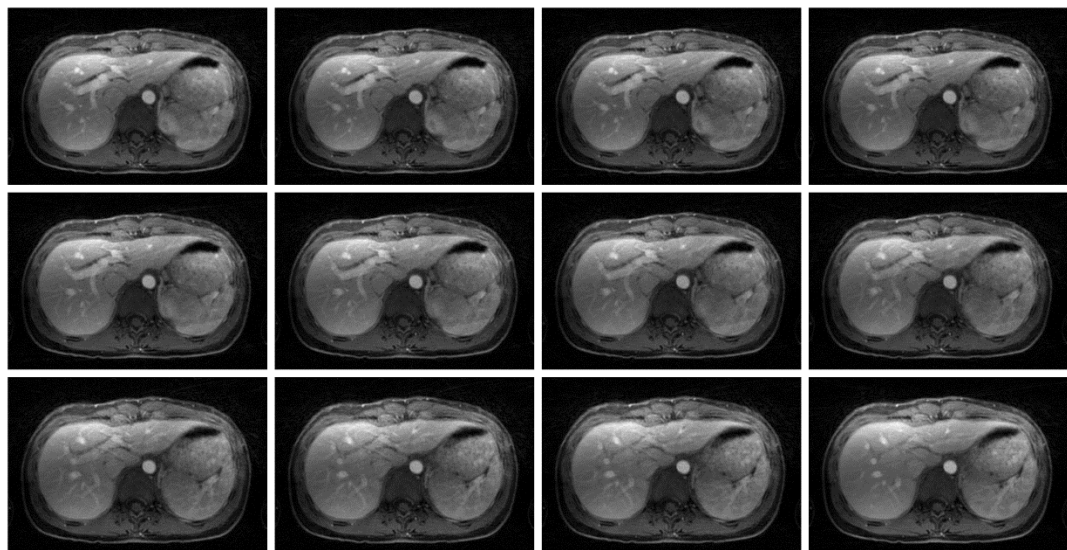


Figure 7-20: 12 motion states reconstructed by L+S with joint sparsity with shifted respiratory soft-weighting matrix in venous phase in liver image. Feasible motion states reconstruction was certificated. The image series with high motion state resolution explored the tissues variation caused by respiratory motion clearly.

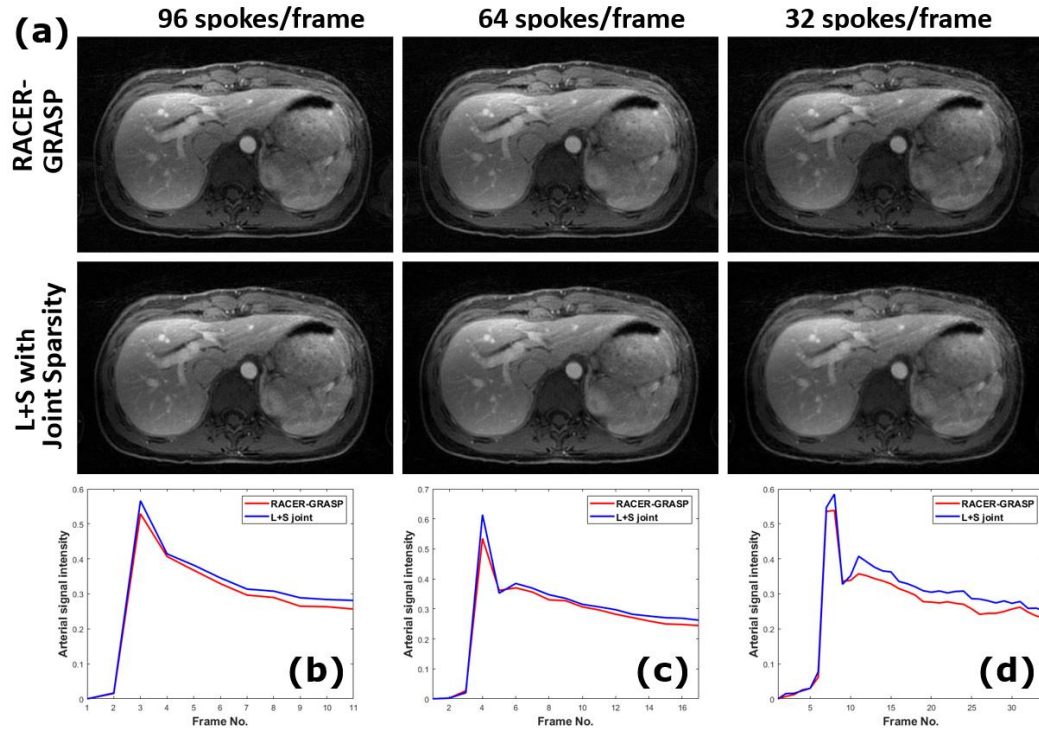


Figure 7-21: (a) A comparison of RACER-GRASP and L+S with soft weighting and joint sparsity at different temporal resolutions in the venous phase of liver images. The end-expiration phase was locked in two frameworks. Blurring artefacts and degradation of image quality were induced at higher AF in RACER-GRASP. Less blurring artefacts and degradation were obtained in the proposed method. The penalty factor for the two reconstruction schemes was set the same among all reconstructions. (b)~(d) Dynamic variation of the arterial signal intensity in the two reconstruction schemes at different temporal resolutions i.e. 96 spokes/frame (AF=6), 64 spokes/frame (AF=9) and 32 spokes/frame (AF=18).

## 7.9 Discussion

Radial sampling repeatedly acquires the k-space center while the imaging contrast of radial sampling is an averaging result among the data acquisition window (75,127). This averaging effect offers intrinsic immunity for the rigid motion. The motion artefact in radial sampling behaves as the motion blurring rather than ghost-

like artefacts in conventional Cartesian sampling (76). However, imaging the tissues with periodic motion like lung and liver is still a challenge in DCE-MRI. Motion blurring caused by respiratory motion or cardiac motion still degrades the image quality.

GRASP based techniques involved an additional motion subdivision besides the temporal subdivision, forming XD-GRASP and RACER-GRASP. XD-GRASP can lock multiple motion phases accurately and reconstruct them simultaneously, offering additional motion phase information for diagnosis. However, the AF of reconstructed images in XD-GRASP is directly proportional to the number of motion states. Excessive AF results in residual streaking artefacts and SNR degradation. The additional computation cost on motion dimension significantly decreases the reconstruction efficiency of XD-GRASP than that of standard GRASP, limiting its clinical applications further.

RACER-GRASP involves a weighted combination of motion states during iteration while only a certain motion phase was locked as the output. Hence, all of the acquired spokes within the frame were involved in the RACER-GRASP reconstruction with different weightings. The equivalent AF is not increased as much as that of XD-GRASP. The computation cost on motion dimension is relatively lower at the expense of losing the abundant motion phase information. The RACER-GRASP provides improved image quality compared with XD-GRASP. The implementation of GROG algorithm accelerates the reconstruction speed of RACER-GRASP further but unexpected convolutional artefacts were also introduced by GROG algorithm.

The proposed soft weighting matrix works as a sort of “soft bandpass” filter which controls the contribution of spokes acquired at the different motion phases. The modified sigmoid function achieves a smooth transition between “passband” in desired motion phase and “stopband” in other motion phases. The combination of L+S decomposition and soft weighting enables more accurate motion compression and higher reconstruction efficiency simultaneously.

To quantify the performance of different motion corrected frameworks, we have established a simulation framework which enables the quantification of motion correction and dynamic contrast simultaneously. Minimum motion errors were achieved by L+S with soft weighting in a simulated phantom dataset. One of the most significant merits of soft weighting is that it brings much less computation complexity than the motion subdivision during iterative reconstruction. Additional computation cost caused by soft weighting is negligible. L+S with soft weighting shows the same reconstruction efficiency as standard L+S decomposition. Without the need of GROG acceleration, two L+S based techniques still show higher reconstruction efficiency than GROG accelerated RACER-GRASP. Another merit of soft weighting is that it is able to provide abundant motion phase information like XD-GRASP. Feasible motion state resolution was achieved by shift weighting function among different respiratory phases. Exploring the variation of tissues within respiratory in detail may provide additional clinical information for diagnosis. One of most the significant drawbacks of motion correction methods (either motion subdivision or soft-weighting) in DCE-MRI reconstruction schemes is that the additional dynamic degradation. The peak dynamic signal in two motion corrected

GRASP techniques and L+S with soft weighting was decreased than the standard GRASP and L+S decomposition. In fact, the subdivision of motion states or soft weighting degrades the weight of data consistency components  $L_2$  norm while the weight of sparsity constraint  $L_1$  norm increases significantly in the optimization model. The equivalent value of penalty factor  $\lambda_T$  for temporal TV is amplified which is helpful to compress unstreaking artefacts at increased AF (caused by soft weighting or motion subdivision). However, temporal averaging effect is also improved and leads to a further degradation of dynamic contrast.

We introduced temporal FFT into L+S with soft weighting to recovery the dynamic contrast. The reconstruction results in the phantom dataset have certificated that additional temporal FFT successfully improved the dynamic contrast as expected for the L+S with soft weighting. The accuracy of motion compression was not degraded by the temporal FFT as well. The reconstruction results of clinic dataset have certificated that the proposed L+S with soft weighting and joint sparsity achieved high reconstruction efficiency, accurate motion compression and improved dynamic contrast simultaneously.

Besides the additional degradation of dynamic contrast, the temporal resolution is another challenge for motion corrected DCE-MRI reconstruction. Sufficient spokes are required to support additional motion subdivision in XD-GRASP and RACER-GRASP. The increase of spokes number within a time frame indicates the significant decrease of temporal resolution. The temporal resolution is decreased from 4 s/frame (28 spokes/frame) in chapter 6.6 to around 15 s/frame (100 spokes/frames) in XD-GRASP and RACER-GRASP which cannot satisfy the

clinical needs of diagnosis. It is unavailable to increase the temporal resolution by reducing the number of spokes within the frames for the XD-GRASP. The excessive AF directly results in failed reconstruction.

For the RACER-GRASP and the proposed L+S with soft weighting and joint sparsity, the number of spokes within the frames in these two schemes is not limited as strictly as it is in XD-GRASP. If the spokes are sufficient to cover a wide range of motion phases, it is still available to reconstruct image series at higher temporal resolution in RACER-GRASP and the proposed method at the cost of blurring.

Improved details of dynamic variation were obtained in both two methods from 96 spokes/frame to 32 spokes/frame in a clinical liver DCE-MRI dataset, showing the importance of high temporal resolution for clinical diagnosis in DCE-MRI. L+S decomposition based model enables better tissues detail and less blurring than RACER-GRASP among all the reconstructions at different AF. The superiority of dynamic contrast was maintained among all of temporal resolutions in the proposed method.

## **7.10 Conclusion**

L+S with joint sparsity and soft weighting demonstrates the use of combining L+S model with joint sparsity constraints for improved dynamic contrast, accurate motion compression, high temporal resolution and computationally efficient free-breathing DCE-MRI. The modified respiratory weighting function enables feasible motion states resolution in DCE-MRI which can provide additional diagnosis information and extends its clinical applications.

# Chapter 8 Conclusion and Future Development

This chapter presents a summary of research works and contributions made in this thesis. The limitations of the research and future plan are discussed.

## 8.1 Thesis Contributions

A 3D UTE imaging protocol is developed based on the stack-of-star central out golden angle sampling scheme with adaptive TE. With the design of the adaptive phase encoding, the minimum TE in the proposed UTE protocol is around 140  $\mu$ s which is similar to the conventional 3D central out radial UTE protocol. The combination of iterative DCF function and trajectory measurement enables a simple and robust calibration for the proposed UTE imaging protocol.

The proposed UTE imaging protocol enables a variety of applications including short  $T_2$  tissues imaging and metal implant imaging. The short  $T_2$  tissues like nose nerve and knee cartilage are clearly displayed in UTE images. The signal dephasing and geometry distortion caused by the metal implant are effectively reduced in UTE images. The data acquisition efficiency is increased by employing the continuous data acquisition model. Motion resolved UTE lung imaging has been achieved by the proposed method within 5 minutes, compressing the motion blurring effectively. Our method also enables functional lung imaging with the support of oxygen-enhanced MRI. For the oxygen-enhanced UTE MRI with motion subdivision, the interpolation errors and better PSE maps are obtained. A declining tendency of oxygen enhancement is observed from expiration phase to inspiration phase.

Besides the proposed 3D UTE imaging protocol, this thesis also presents an advanced free-breathing DCE-MRI reconstruction method called L+S with joint sparsity based on the stack-of-stars golden angle sampling scheme. A simulation framework has been established to evaluate the performance of the proposed method. Several simulated phantom datasets are created with fully sampled reference, enabling quantification of the dynamic contrast performance.

Temporal TV minimizes the variations on the temporal dimension which is helpful to reconstruct the highly undersampled time series. Unexpected temporal blurring is introduced by temporal TV which degrades the dynamic contrast in conventional reconstruction frameworks. The proposed method improves the dynamic contrast by implementing an additional sparsity constraint temporal FFT. The proposed reconstruction framework also maintains the reconstruction efficiency of L+S model which is much higher than GRASP based techniques. A robust motion correction approach is introduced into the proposed framework. The conventional GRASP based techniques employ motion subdivision to compress the motion blurring while the motion subdivision degrades the reconstruction efficiency and image quality. The soft weighting matrix in the proposed method compresses the motion blurring effectively without the expense of reconstruction efficiency. Both motion subdivision and soft weighting amplify the contribution of temporal TV constraint in reconstruction schemes, degrading the dynamic contrast further. By combining the soft weighting and joint sparsity, the proposed L+S with soft weighting and joint sparsity offers improved dynamic contrast, advanced motion compression and high reconstruction efficiency for DCE-MRI simultaneously.

## 8.2 Significant Innovations

In stack-of-stars central out golden angle UTE imaging, several innovations are contained in the proposed imaging protocol:

1. A simple and robust calibration method has been developed by the trajectory measurement and iterative DCF. The pre-scans measure the deviation of samples accurately. No delicate calibration of hardware system is required. The iterative DCF effectively removes the blurring caused by the gridding with deviated samples.
2. The continuous acquisition model is implemented into the UTE lung imaging to improve the data acquisition efficiency significantly. By utilizing the self-gating property of the stack-of-stars, the respiratory signal is estimated without the support of additional gating systems.
3. Motion resolved UTE lung imaging is achieved by the motion subdivision according to the estimated motion signal. Respiratory motion blurring is effectively reduced by motion subdivision. The variation of lung tissues caused by respiratory can be investigated by reconstructing multiple respiratory motion states.
4. Functional lung imaging is achieved by the proposed protocol with the support of oxygen-enhanced MRI. The interpolation errors in registrations in oxygen-enhanced UTE are also reduced by the prior motion subdivision.

In DCE-MRI, several innovations are contained in the proposed reconstruction frameworks:

1. Additional temporal FFT sparsity constraint is integrated into the standard L+S decomposition model to recover the dynamic contrast from temporal blurring.
2. FCSA algorithm is implemented to solve the L+S model with two sparsity constraints. The reconstruction efficiency of L+S model is maintained in the proposed L+S with joint sparsity. The computation complexity from the additional sparsity constraint is minimized by FCSA.
3. Soft weighting matrix is applied for motion compression in the proposed method. The soft weighting compresses the motion blurring effectively without the expense of computational complexity.
4. Joint sparsity and soft weighting are combined in the L+S model, forming L+S with soft weighting and joint sparsity. The proposed framework enables improved dynamic contrast, advanced motion compression and high reconstruction efficiency for DCE-MRI simultaneously.
5. Two simulation frameworks are established in this thesis. Several simulation phantom datasets are produced with additional fully sampled reference and ground truth to quantify the performance of the proposed method. The dynamic performance and motion correction of different reconstruction frameworks are quantified by a variety of parameters, including Euclidean distance and RMSE.

### **8.3 Limitations and Future Research Plan**

In the proposed UTE imaging protocol, sufficient spokes are required in stack-of-stars central out golden angle sampling scheme to satisfy the Nyquist standard. The number of spokes is extended further in motion resolved UTE to support the additional motion states subdivision. A total of 5~10 minutes scan duration is relatively long for patients and degrades the clinical experience. Due to the limitation of scan duration, the motion resolution is relatively low which is insufficient to catch the variation of lung tissues during respiratory.

The overall scan duration can be reduced effectively by employing the acceleration technique. We plan to design a compressed sensing based reconstruction framework which reconstructs the highly undersampled k-space by exploring the sparsity among the subdivided motion states. The blurring effect caused by sparsity constraint will be investigated.

Another windowing function is also considered to improve the motion resolution. By gradually replacing the acquired spokes among adjacent respiratory phases, the window function can effectively increase the number of motion states without the increase of AF. Utilizing the continuous acquisition model in golden angle sampling and windowing function can also be helpful to investigate the signal intensity variation of lung tissues during 5 minutes wash-in-time period in oxygen-enhanced UTE lung imaging.

The performance of DCE-MRI reconstruction frameworks highly relies on the parameter design of the penalty factor. Residual undersampling artefacts or excessive temporal averaging can be induced by the inappropriate design of the penalty factor. A more delicate design of the penalty factor is required by the proposed framework with joint sparsity. We plan to further investigate the combination of penalty factors for temporal FFT and temporal TV constraints and obtain an optimized and robust parameter design in L+S with joint sparsity.

The temporal resolution is a challenge for motion corrected DCE-MRI reconstruction. Sufficient spokes are required to support additional motion subdivision or soft weighting which degrades the temporal resolution of reconstructed image series. The current temporal resolution in motion corrected reconstruction frameworks cannot satisfy the clinical needs of diagnosis.

Based on the L+S reconstruction model and soft weighting, the AF can be further increased in the proposed L+S with soft weighting and joint sparsity framework. Further research is required to improve the temporal resolution without the expense of image quality, dynamic contrast and motion compression.

## Reference

1. Brown RW, Cheng Y-CN, Haacke EM, Thompson MR, Venkatesan R. Magnetic resonance imaging: physical principles and sequence design: John Wiley & Sons; 2014.
2. Purcell EM, Torrey HC, Pound RV. Resonance absorption by nuclear magnetic moments in a solid. *Physical review* 1946;69(1-2):37.
3. Lauterbur PC. Image formation by induced local interactions: examples employing nuclear magnetic resonance. *nature* 1973;242(5394):190-191.
4. Kumar A, Welti D, Ernst RR. NMR Fourier zeugmatography. *Journal of Magnetic Resonance (1969)* 1975;18(1):69-83.
5. Chernoff D, Stark P. Principles of magnetic resonance imaging. UpToDate Waltham MA: UpToDate Retrieved February 2010.
6. Holmes JE, Bydder GM. MR imaging with ultrashort TE (UTE) pulse sequences: Basic principles. *Radiography* 2005;11(3):163-174.
7. Tyler DJ, Robson MD, Henkelman RM, Young IR, Bydder GM. Magnetic resonance imaging with ultrashort TE (UTE) PULSE sequences: technical considerations. *Journal of Magnetic Resonance Imaging: An Official Journal of the International Society for Magnetic Resonance in Medicine* 2007;25(2):279-289.
8. Ma Y-J, Jang H, Chang EY, Hiniker A, Head BP, Lee RR, Corey-Bloom J, Bydder GM, Du J. Ultrashort echo time (UTE) magnetic resonance imaging of myelin: Technical developments and challenges. *Quantitative imaging in medicine and surgery* 2020;10(6):1186.
9. Chan CF, Keenan NG, Nielles-Vallespin S, Gatehouse P, Sheppard MN, Boyle JJ, Pennell DJ, Firmin DN. Ultra-short echo time cardiovascular magnetic resonance of atherosclerotic carotid plaque. *Journal of Cardiovascular Magnetic Resonance* 2010;12(1):1-8.
10. Tourais J, Krishnamoorthy G, Kouwenhoven M, Smink J, Breeuwer M. 3D Golden Angle Stack-of-Stars with Anisotropic Field-of-View. ISMRM 2018. Paris.

11. Roach DJ, Crémillieux Y, Fleck RJ, Brody AS, Serai SD, Szczesniak RD, Kerlakian S, Clancy JP, Woods JC. Ultrashort echo-time magnetic resonance imaging is a sensitive method for the evaluation of early cystic fibrosis lung disease. *Annals of the American Thoracic Society* 2016;13(11):1923-1931.
12. Cha MJ, Park HJ, Paek MY, Stemmer A, Lee ES, Park SB, Kim YS. Free-breathing ultrashort echo time lung magnetic resonance imaging using stack-of-spirals acquisition: a feasibility study in oncology patients. *Magnetic resonance imaging* 2018;51:137-143.
13. MacFall JR, Pelc NJ, Vavrek RM. Correction of spatially dependent phase shifts for partial Fourier imaging. *Magnetic resonance imaging* 1988;6(2):143-155.
14. Haacke EM, Mitchell J, Lee D. Improved contrast at 1.5 tesla using half-Fourier imaging: application to spin-echo and angiographic imaging. *Magnetic resonance imaging* 1990;8(1):79-90.
15. Runge VM, Wood ML. Half-Fourier MR imaging of CNS disease. *American journal of neuroradiology* 1990;11(1):77-82.
16. Sodickson DK, Manning WJ. Simultaneous acquisition of spatial harmonics (SMASH): fast imaging with radiofrequency coil arrays. *Magnetic resonance in medicine* 1997;38(4):591-603.
17. Pruessmann KP, Weiger M, Scheidegger MB, Boesiger P. SENSE: sensitivity encoding for fast MRI. *Magn Reson Med* 1999;42(5):952-962.
18. Griswold MA, Jakob PM, Heidemann RM, Nittka M, Jellus V, Wang J, Kiefer B, Haase A. Generalized autocalibrating partially parallel acquisitions (GRAPPA). *Magn Reson Med* 2002;47(6):1202-1210.
19. Sodickson DK, McKenzie CA. A generalized approach to parallel magnetic resonance imaging. *Medical physics* 2001;28(8):1629-1643.
20. Donoho DL. Compressed sensing. *IEEE Transactions on information theory* 2006;52(4):1289-1306.
21. Lustig M, Donoho D, Pauly JM. Sparse MRI: The application of compressed sensing for rapid MR imaging. *Magn Reson Med* 2007;58(6):1182-1195.

22. Lustig M, Donoho DL, Santos JM, Pauly JM. Compressed sensing MRI. *IEEE Signal Processing Magazine* 2008;25(2):72-82.
23. Chang CH, Ji J. Compressed sensing MRI with multichannel data using multicore processors. *Magnetic resonance in medicine* 2010;64(4):1135-1139.
24. Bilgin A, Trouard T, Gmitro A, Altbach M. Randomly perturbed radial trajectories for compressed sensing MRI. 2008. p 3152.
25. Jung H, Park J, Yoo J, Ye JC. Radial k-t FOCUSS for high-resolution cardiac cine MRI. *Magnetic Resonance in Medicine: An Official Journal of the International Society for Magnetic Resonance in Medicine* 2010;63(1):68-78.
26. Block KT, Chandarana H, Milla S, Bruno M, Mulholland T, Fatterpekar G, Hagiwara M, Grimm R, Geppert C, Kiefer B. Towards routine clinical use of radial stack-of-stars 3D gradient-echo sequences for reducing motion sensitivity. *Journal of the Korean Society of Magnetic Resonance in Medicine* 2014;18(2):87-106.
27. Block KT, Grimm R, Feng L, Otazo R, Chandarana H, Bruno M, Geppert C, Sodickson DK. Bringing compressed sensing to clinical reality: prototypic setup for evaluation in routine applications. 2013. Salt Lake City Utah, USA. p 3809.
28. Wech T, Pickl W, Tran-Gia J, Ritter C, Beer M, Hahn D, Köstler H. Whole-heart cine MRI in a single breath-hold—a compressed sensing accelerated 3D acquisition technique for assessment of cardiac function. 2014. © Georg Thieme Verlag KG. p 37-41.
29. Winkelmann S, Schaeffter T, Koehler T, Eggers H, Doessel O. An optimal radial profile order based on the Golden Ratio for time-resolved MRI. *IEEE transactions on medical imaging* 2006;26(1):68-76.
30. Bloch F. Nuclear induction. *Physical review* 1946;70(7-8):460.
31. Rooney W. MRI: from picture to proton. LWW; 2003.
32. Vaughan JT, Griffiths JR. RF coils for MRI: John Wiley & Sons; 2012.

33. Block KT. Advanced methods for radial data sampling in magnetic resonance imaging. SUB University of Goettingen 2008.
34. O'Sullivan JD. A fast sinc function gridding algorithm for Fourier inversion in computer tomography. *IEEE transactions on medical imaging* 1985;4(4):200-207.
35. Malik WQ, Khan HA, Edwards DJ, Stevens CJ. A gridding algorithm for efficient density compensation of arbitrarily sampled Fourier-domain data. 2005. *IEEE*. p 125-128.
36. Jackson JI, Meyer CH, Nishimura DG, Macovski A. Selection of a convolution function for Fourier inversion using gridding (computerised tomography application). *IEEE transactions on medical imaging* 1991;10(3):473-478.
37. Rasche V, Proksa R, Sinkus R, Bornert P, Eggers H. Resampling of data between arbitrary grids using convolution interpolation. *IEEE transactions on medical imaging* 1999;18(5):385-392.
38. Walsh DO, Gmitro AF, Marcellin MW. Adaptive reconstruction of phased array MR imagery. *Magn Reson Med* 2000;43(5):682-690.
39. Uecker M, Lai P, Murphy MJ, Virtue P, Elad M, Pauly JM, Vasanawala SS, Lustig M. ESPIRiT—an eigenvalue approach to autocalibrating parallel MRI: where SENSE meets GRAPPA. *Magnetic resonance in medicine* 2014;71(3):990-1001.
40. Ohliger MA, Grant AK, Sodickson DK. Ultimate intrinsic signal-to-noise ratio for parallel MRI: electromagnetic field considerations. *Magn Reson Med* 2003;50(5):1018-1030.
41. Candès EJ, Romberg J, Tao T. Robust uncertainty principles: Exact signal reconstruction from highly incomplete frequency information. *IEEE Transactions on information theory* 2006;52(2):489-509.
42. Dai Y-H, Yuan Y. *Nonlinear conjugate gradient methods*. Shanghai Science and Technology Publisher, Shanghai 2000.
43. Kowalski M. Thresholding rules and iterative shrinkage/thresholding algorithm: A convergence study. 2014. *IEEE*. p 4151-4155.

44. Beck A, Teboulle M. A fast iterative shrinkage-thresholding algorithm for linear inverse problems. *SIAM Journal on Imaging Sciences* 2009;2(1):183-202.
45. Liang D, Liu B, Wang J, Ying L. Accelerating SENSE using compressed sensing. *Magnetic Resonance in Medicine: An Official Journal of the International Society for Magnetic Resonance in Medicine* 2009;62(6):1574-1584.
46. Otazo R, Kim D, Axel L, Sodickson DK. Combination of compressed sensing and parallel imaging for highly accelerated first-pass cardiac perfusion MRI. *Magnetic resonance in medicine* 2010;64(3):767-776.
47. Huang J, Zhang S, Metaxas D. Efficient MR image reconstruction for compressed MR imaging. *Medical Image Analysis* 2011;15(5):670-679.
48. Robson MD, Gatehouse PD, Bydder M, Bydder GM. Magnetic resonance: an introduction to ultrashort TE (UTE) imaging. *Journal of computer assisted tomography* 2003;27(6):825-846.
49. Larson PE, Han M, Krug R, Jakary A, Nelson SJ, Vigneron DB, Henry RG, McKinnon G, Kelley DA. Ultrashort echo time and zero echo time MRI at 7T. *Magnetic Resonance Materials in Physics, Biology and Medicine* 2016;29(3):359-370.
50. Weiger M, Pruessmann K. MRI with zero echo time. *eMagRes* 2007.
51. Grodzki DM, Jakob PM, Heismann B. Ultrashort echo time imaging using pointwise encoding time reduction with radial acquisition (PETRA). *Magnetic resonance in medicine* 2012;67(2):510-518.
52. Sun Y, Ventura M, Oosterwijk E, Jansen JA, Walboomers XF, Heerschap A. Zero echo time magnetic resonance imaging of contrast-agent-enhanced calcium phosphate bone defect fillers. *Tissue Engineering Part C: Methods* 2013;19(4):281-287.
53. Du J, Bydder M, Takahashi AM, Carl M, Chung CB, Bydder GM. Short T2 contrast with three-dimensional ultrashort echo time imaging. *Magnetic resonance imaging* 2011;29(4):470-482.

54. Chen B, Zhao Y, Cheng X, Ma Y, Chang EY, Kavanaugh A, Liu S, Du J. Three-dimensional ultrashort echo time cones (3D UTE-Cones) magnetic resonance imaging of entheses and tendons. *Magnetic resonance imaging* 2018;49:4-9.
55. Dournes G, Yazbek J, Benhassen W, Benlala I, Blanchard E, Truchetet ME, Macey J, Berger P, Laurent F. 3D ultrashort echo time MRI of the lung using stack-of-spirals and spherical k-space coverages: Evaluation in healthy volunteers and parenchymal diseases. *Journal of Magnetic Resonance Imaging* 2018;48(6):1489-1497.
56. Qian Y, Boada FE. Acquisition-weighted stack of spirals for fast high-resolution three-dimensional ultra-short echo time MR imaging. *Magnetic Resonance in Medicine: An Official Journal of the International Society for Magnetic Resonance in Medicine* 2008;60(1):135-145.
57. McCallister A, Chung SH, Antonacci M, Z Powell M, Ceppe AS, Donaldson SH, Lee YZ, Branca RT, Goralski JL. Comparison of single breath hyperpolarized  $^{129}\text{Xe}$  MRI with dynamic  $^{19}\text{F}$  MRI in cystic fibrosis lung disease. *Magnetic Resonance in Medicine* 2021;85(2):1028-1038.
58. Hargreaves BA, Cunningham CH, Nishimura DG, Conolly SM. Variable-rate selective excitation for rapid MRI sequences. *Magnetic Resonance in Medicine: An Official Journal of the International Society for Magnetic Resonance in Medicine* 2004;52(3):590-597.
59. Pauly JM. Selective excitation for ultrashort echo time imaging. *eMagRes* 2007.
60. Brunner DO, Furrer L, Weiger M, Baumberger W, Schmid T, Reber J, Dietrich BE, Wilm BJ, Froidevaux R, Pruessmann KP. Symmetrically biased T/R switches for NMR and MRI with microsecond dead time. *Journal of Magnetic Resonance* 2016;263:147-155.
61. Salim M, Ozen AC, Bock M, Atalar E. Active decoupling of transmit and receive coils for full-duplex MRI. *arXiv preprint arXiv:181010973* 2018.

62. Block KT, Frahm J. Spiral imaging: a critical appraisal. *Journal of Magnetic Resonance Imaging: An Official Journal of the International Society for Magnetic Resonance in Medicine* 2005;21(6):657-668.
63. Ahn C, Cho Z. Analysis of the eddy-current induced artifacts and the temporal compensation in nuclear magnetic resonance imaging. *IEEE transactions on medical imaging* 1991;10(1):47-52.
64. Hughes D, Robertson S, Allen P. Intensity artifacts in MRI caused by gradient switching in an animal-size NMR magnet. *Magnetic resonance in medicine* 1992;25(1):167-179.
65. Mason GF, Harshbarger T, Hetherington HP, Zhang Y, Pohost GM, Twieg DB. A method to measure arbitrary k-space trajectories for rapid MR imaging. *Magnetic resonance in medicine* 1997;38(3):492-496.
66. Alley MT, Glover GH, Pelc NJ. Gradient characterization using a Fourier-transform technique. *Magnetic resonance in medicine* 1998;39(4):581-587.
67. Zhang Y, Hetherington HP, Stokely EM, Mason GF, Twieg DB. A novel k-space trajectory measurement technique. *Magnetic resonance in medicine* 1998;39(6):999-1004.
68. Beaumont M, Lamalle L, Segebarth C, Barbier EL. Improved k-space trajectory measurement with signal shifting. *Magnetic Resonance in Medicine: An Official Journal of the International Society for Magnetic Resonance in Medicine* 2007;58(1):200-205.
69. Pipe JG, Menon P. Sampling density compensation in MRI: rationale and an iterative numerical solution. *Magnetic Resonance in Medicine: An Official Journal of the International Society for Magnetic Resonance in Medicine* 1999;41(1):179-186.
70. Wiens CN, Artz NS, Jang H, McMillan AB, Koch KM, Reeder SB. Fully phase-encoded MRI near metallic implants using ultrashort echo times and broadband excitation. *Magnetic resonance in medicine* 2018;79(4):2156-2163.

71. Hargreaves B, Worters PW, Pauly KB, Pauly JM, Koch KM, Gold GE. Metal induced artifacts in MRI. *AJR American journal of roentgenology* 2011;197(3):547.
72. Carl M, Koch K, Du J. MR imaging near metal with undersampled 3D radial UTE-MAVRIC sequences. *Magnetic resonance in medicine* 2013;69(1):27-36.
73. Tibiletti M, Bianchi A, Kjørstad Å, Wundrak S, Stiller D, Rasche V. Respiratory self-gated 3 D UTE for lung imaging in small animal MRI. *Magnetic resonance in medicine* 2017;78(2):739-745.
74. Johnson KM, Fain SB, Schiebler ML, Nagle S. Optimized 3D ultrashort echo time pulmonary MRI. *Magnetic resonance in medicine* 2013;70(5):1241-1250.
75. Glover GH, Pauly JM. Projection reconstruction techniques for reduction of motion effects in MRI. *Magnetic resonance in medicine* 1992;28(2):275-289.
76. Tibiletti M, Kjørstad Å, Bianchi A, Schad LR, Stiller D, Rasche V. Multistage self-gated lung imaging in small rodents. *Magnetic resonance in medicine* 2016;75(6):2448-2454.
77. Zhang T, Cheng JY, Chen Y, Nishimura DG, Pauly JM, Vasanaawala SS. Robust self-navigated body MRI using dense coil arrays. *Magnetic resonance in medicine* 2016;76(1):197-205.
78. Pang J, Sharif B, Fan Z, Bi X, Arsanjani R, Berman DS, Li D. ECG and navigator-free four-dimensional whole-heart coronary MRA for simultaneous visualization of cardiac anatomy and function. *Magnetic resonance in medicine* 2014;72(5):1208-1217.
79. Kaushik SS, Cleveland ZI, Cofer GP, Metz G, Beaver D, Nouls J, Kraft M, Auffermann W, Wolber J, McAdams HP. Diffusion-weighted hyperpolarized <sup>129</sup>Xe MRI in healthy volunteers and subjects with chronic obstructive pulmonary disease. *Magnetic Resonance in Medicine* 2011;65(4):1154-1165.
80. Mugler III JP, Driehuys B, Brookeman JR, Cates GD, Berr SS, Bryant RG, Daniel TM, De Lange EE, Downs JH, Erickson CJ. MR imaging and

- spectroscopy using hyperpolarized  $^{129}\text{Xe}$  gas: preliminary human results. *Magnetic resonance in medicine* 1997;37(6):809-815.
81. Kauczor H-U, Surkau R, Roberts T. MRI using hyperpolarized noble gases. *European radiology* 1998;8(5):820-827.
  82. Chen XJ, Hedlund LW, Möller HE, Chawla MS, Maronpot RR, Johnson GA. Detection of emphysema in rat lungs by using magnetic resonance measurements of  $^3\text{He}$  diffusion. *Proceedings of the National Academy of Sciences* 2000;97(21):11478-11481.
  83. Ohno Y, Hatabu H. Basics concepts and clinical applications of oxygen-enhanced MR imaging. *European journal of radiology* 2007;64(3):320-328.
  84. Young I, Clarke G, Bailes D, Pennock J, Doyle F, Bydder G. Enhancement of relaxation rate with paramagnetic contrast agents in NMR imaging. *The Journal of computed tomography* 1981;5(6):543-547.
  85. Goodrich K, Hackmann A, Ganesan K, Ailion D, Cutillo A. Spin-lattice relaxation in excised rat lung. 1992. p 1307.
  86. Ohno Y, Hatabu H, Higashino T, Nogami M, Takenaka D, Watanabe H, Van Cauteren M, Yoshimura M, Satouchi M, Nishimura Y. Oxygen-enhanced MR imaging: correlation with postsurgical lung function in patients with lung cancer. *Radiology* 2005;236(2):704-711.
  87. Ohno Y, Hatabu H. Basics concepts and clinical applications of oxygen-enhanced MR imaging. *Eur J Radiol* 2007;64(3):320-328.
  88. Puderbach M, Ohno Y, Kawamitsu H, Koyama H, Takenaka D, Nogami M, Obara M, Van Cauteren M, Kauczor HU, Sugimura K. Influence of inversion pulse type in assessing lung-oxygen-enhancement by centrally-reordered non-slice-selective inversion-recovery half-Fourier single-shot turbo spin-echo (HASTE) sequence. *Journal of Magnetic Resonance Imaging: An Official Journal of the International Society for Magnetic Resonance in Medicine* 2007;26(4):1133-1138.
  89. Renne J, Lauermann P, Hinrichs J, Schönfeld C, Sorrentino S, Gutberlet M, Jakob P, Wacker F, Vogel-Claussen J. Clinical use of oxygen-enhanced T1 mapping MRI of the lung: Reproducibility and impact of closed versus loose

- fit oxygen delivery system. *Journal of Magnetic Resonance Imaging* 2015;41(1):60-66.
90. Mai VM, Liu B, Li W, Polzin J, Kurucay S, Chen Q, Edelman RR. Influence of oxygen flow rate on signal and T1 changes in oxygen-enhanced ventilation imaging. *Journal of Magnetic Resonance Imaging: An Official Journal of the International Society for Magnetic Resonance in Medicine* 2002;16(1):37-41.
91. Jakob PM, Wang T, Schultz G, Hebestreit H, Hebestreit A, Hahn D. Assessment of human pulmonary function using oxygen-enhanced T1 imaging in patients with cystic fibrosis. *Magnetic Resonance in Medicine: An Official Journal of the International Society for Magnetic Resonance in Medicine* 2004;51(5):1009-1016.
92. Kershaw LE, Naish JH, McGrath DM, Waterton JC, Parker GJ. Measurement of arterial plasma oxygenation in dynamic oxygen-enhanced MRI. *Magnetic resonance in medicine* 2010;64(6):1838-1842.
93. Zhang W-J, Niven RM, Young SS, Liu Y-Z, Parker GJ, Naish JH. Dynamic oxygen-enhanced magnetic resonance imaging of the lung in asthma—Initial experience. *European journal of radiology* 2015;84(2):318-326.
94. Triphan SM, Breuer FA, Gensler D, Kauczor HU, Jakob PM. Oxygen enhanced lung MRI by simultaneous measurement of T1 and T2\* during free breathing using ultrashort TE. *Journal of Magnetic Resonance Imaging* 2015;41(6):1708-1714.
95. Triphan SM, Jobst BJ, Breuer FA, Wielpütz MO, Kauczor HU, Biederer J, Jakob PM. Echo time dependence of observed T1 in the human lung. *Journal of Magnetic Resonance Imaging* 2015;42(3):610-616.
96. Kruger SJ, Fain SB, Johnson KM, Cadman RV, Nagle SK. Oxygen-enhanced 3D radial ultrashort echo time magnetic resonance imaging in the healthy human lung. *NMR in biomedicine* 2014;27(12):1535-1541.
97. Sasaki T, Takahashi K, Obara M. Viability of oxygen-enhanced ventilation imaging of the lungs using ultra-short echo time MRI. *Magnetic Resonance in Medical Sciences* 2017;16(3):259.

98. Naish JH, Parker GJ, Beatty PC, Jackson A, Young SS, Waterton JC, Taylor CJ. Improved quantitative dynamic regional oxygen-enhanced pulmonary imaging using image registration. *Magnetic Resonance in Medicine: An Official Journal of the International Society for Magnetic Resonance in Medicine* 2005;54(2):464-469.
99. Cootes TF, Taylor CJ, Cooper DH, Graham J. Active shape models-their training and application. *Computer vision and image understanding* 1995;61(1):38-59.
100. Usman M, Atkinson D, Odille F, Kolbitsch C, Vaillant G, Schaeffter T, Batchelor PG, Prieto C. Motion corrected compressed sensing for free-breathing dynamic cardiac MRI. *Magn Reson Med* 2013;70(2):504-516.
101. Padhani AR. Dynamic contrast-enhanced MRI in clinical oncology: current status and future directions. *J Magn Reson Imaging* 2002;16(4):407-422.
102. Sourbron SP, Buckley DL. Classic models for dynamic contrast-enhanced MRI. *NMR in Biomedicine* 2013;26(8):1004-1027.
103. Alonzi R, Padhani AR, Allen C. Dynamic contrast enhanced MRI in prostate cancer. *European Journal of Radiology* 2007;63(3):335-350.
104. Xu B, Spincemaille P, Chen G, Agrawal M, Nguyen TD, Prince MR, Wang Y. Fast 3D contrast enhanced MRI of the liver using temporal resolution acceleration with constrained evolution reconstruction. *Magn Reson Med* 2013;69(2):370-381.
105. Kim D, Dyvorne HA, Otazo R, Feng L, Sodickson DK, Lee VS. Accelerated phase-contrast cine MRI using k-t SPARSE-SENSE. *Magn Reson Med* 2012;67(4):1054-1064.
106. Feng L, Srichai MB, Lim RP, Harrison A, King W, Adluru G, Dibella EV, Sodickson DK, Otazo R, Kim D. Highly accelerated real-time cardiac cine MRI using k-t SPARSE-SENSE. *Magn Reson Med* 2013;70(1):64-74.
107. Block KT, Uecker M, Frahm J. Undersampled radial MRI with multiple coils. Iterative image reconstruction using a total variation constraint. *Magn Reson Med* 2007;57(6):1086-1098.

108. Feng L, Grimm R, Block KT, Chandarana H, Kim S, Xu J, Axel L, Sodickson DK, Otazo R. Golden-angle radial sparse parallel MRI: combination of compressed sensing, parallel imaging, and golden-angle radial sampling for fast and flexible dynamic volumetric MRI. *Magn Reson Med* 2014;72(3):707-717.
109. Rosenkrantz AB, Geppert C, Grimm R, Block TK, Glielmi C, Feng L, Otazo R, Ream JM, Romolo MM, Taneja SS. Dynamic contrast-enhanced MRI of the prostate with high spatiotemporal resolution using compressed sensing, parallel imaging, and continuous golden-angle radial sampling: preliminary experience. *J Magn Reson Imaging* 2015;41(5):1365-1373.
110. Chandarana H, Feng L, Block TK, Rosenkrantz AB, Lim RP, Babb JS, Sodickson DK, Otazo R. Free-breathing contrast-enhanced multiphase MRI of the liver using a combination of compressed sensing, parallel imaging, and golden-angle radial sampling. *Investigative Radiology* 2013;48(1).
111. Zhao B, Haldar JP, Brinegar C, Liang Z-P. Low rank matrix recovery for real-time cardiac MRI. 2010. 2010 IEEE International Symposium on Biomedical Imaging. p 996-999.
112. Lingala SG, Hu Y, DiBella E, Jacob M. Accelerated dynamic MRI exploiting sparsity and low-rank structure: kt SLR. *IEEE Transactions on Medical Imaging* 2011;30(5):1042-1054.
113. Otazo R, Candes E, Sodickson DK. Low-rank plus sparse matrix decomposition for accelerated dynamic MRI with separation of background and dynamic components. *Magn Reson Med* 2015;73(3):1125-1136.
114. Chandrasekaran V, Sanghavi S, Parrilo PA, Willsky AS. Rank-sparsity incoherence for matrix decomposition. *SIAM Journal on Optimization* 2011;21(2):572-596.
115. Candès EJ, Li X, Ma Y, Wright J. Robust principal component analysis? *Journal of the ACM (JACM)* 2011;58(3):1-37.
116. Helena B, Pardo R, Vega M, Barrado E, Fernandez JM, Fernandez L. Temporal evolution of groundwater composition in an alluvial aquifer

- (Pisuerga River, Spain) by principal component analysis. *Water research* 2000;34(3):807-816.
117. Weiss Y, Chang HS, Freeman WT. *Learning compressed sensing*. 2007. Citeseer.
  118. Chen L, Schabel MC, DiBella EV. Reconstruction of dynamic contrast enhanced magnetic resonance imaging of the breast with temporal constraints. *Magnetic Resonance Imaging* 2010;28(5):637-645.
  119. Huang J, Wang L, Zhu Y. Compressed sensing MRI reconstruction with multiple sparsity constraints on radial sampling. *Mathematical Problems in Engineering* 2019;2019.
  120. Huang J, Zhang S, Li H, Metaxas D. Composite splitting algorithms for convex optimization. *Computer Vision and Image Understanding* 2011;115(12):1610-1622.
  121. Feng L, Axel L, Chandarana H, Block KT, Sodickson DK, Otazo R. XD-GRASP: golden-angle radial MRI with reconstruction of extra motion-state dimensions using compressed sensing. *Magn Reson Med* 2016;75(2):775-788.
  122. Feng L, Huang C, Shanbhogue K, Sodickson DK, Chandarana H, Otazo R. RACER-GRASP: respiratory-weighted, aortic contrast enhancement-guided and coil-unstreaking golden-angle radial sparse MRI. *Magn Reson Med* 2018;80(1):77-89.
  123. Buehrer M, Pruessmann KP, Boesiger P, Kozerke S. Array compression for MRI with large coil arrays. *Magnetic Resonance in Medicine: An Official Journal of the International Society for Magnetic Resonance in Medicine* 2007;57(6):1131-1139.
  124. Chen L, Zeng X, Ji B, Liu D, Wang J, Zhang J, Feng L. Improving dynamic contrast-enhanced MRI of the lung using motion-weighted sparse reconstruction: Initial experiences in patients. *Magnetic resonance imaging* 2020;68:36-44.
  125. Seiberlich N, Breuer F, Blaimer M, Jakob P, Griswold M. Self-calibrating GRAPPA operator gridding for radial and spiral trajectories. *Magnetic*

Resonance in Medicine: An Official Journal of the International Society for Magnetic Resonance in Medicine 2008;59(4):930-935.

126. Benkert T, Tian Y, Huang C, DiBella EV, Chandarana H, Feng L. Optimization and validation of accelerated golden-angle radial sparse MRI reconstruction with self-calibrating GRAPPA operator gridding. *Magn Reson Med* 2018;80(1):286-293.
127. Feng L. *Rapid and continuous magnetic resonance imaging using compressed sensing*: New York University; 2015.